BIOTECHNOLOGY DEPARTMENT, UNIVERSITAT POLITÈCNICA DE VALÈNCIA

CANCER IMMUNOLOGY AND VIROLOGY DEPARTMENT,
DANA FARBER CANCER INSTITUTE

STUDY OF IMMUNE RESISTANT MECHANISMS IN MOUSE MODELS OF BREAST CANCER

PILAR BALDOMINOS FLORES

February 2024

DR. RAFAEL SIRERA PEREZ

DR. JUDITH AGUDO CANTERO

BIOTECHNOLOGY DEPARTMENT, UNIVERSITAT POLITÈCNICA DE VALÈNCIA

CANCER IMMUNOLOGY AND VIROLOGY DEPARTMENT, DANA FARBER CANCER INSTITUTE

Study of immune resistant mechanisms in mouse models of breast cancer

Pilar Baldominos Flores

February 2024

Dr. Rafael Sirera Perez

Dr. Judith Agudo Cantero

This PhD thesis has been elaborated under the supervision of Dr. Judith Agudo at the Cancer Immunology and Virology department of Dana Farber Cancer Institute and Dr. Rafael Sirera at the Biotechnology department of Universidad Politecnica de Valencia.

PILAR BALDOMINOS FLORES

JUDITH AGUDO CANTERO **RAFAEL SIRERA PEREZ**

“Dreams are extremely important.
You can’t do it unless you image it.”
George Lucas

Acknowledgements

I would like to take this opportunity to thank the people that have made this accomplishment possible because as they say in English “it takes a village” to do a PhD thesis.

Firstly, I would like to thank my directors Judith and Rafa. They supported me since the very beginning and embarked with me in this adventure. Thank you for believing in me and nurture my dreams and aspirations, it has been a pleasure to learn from you scientifically and personally. I can’t imagine having better mentors.

I would like to thank to all my lab mates, the current and the past ones, for generating an amazing atmosphere in the lab where we all truly celebrate each other accomplishments. But also, for being there in the days where nothing works, the days in which the path seems too hard, and we fantasize about becoming bakers and farmers. I would like to specially thank Lauren for the last months working together, for making collaborations easy and for being able to talk frankly about our needs and ways to approach the projects. I think we are an amazing team and can’t wait to keep working on this with you! I cannot write acknowledgements about my PhD journey without mentioning my students (JT, Guillem, Ia and Raphie). I am so proud of all of you; and I hope you learned as much from me as I learned from you.

Special thanks also to all the other scientist and personnel in the department and cores that make science easier and work-life a fun journey. Special thanks to Olga, for teaching me everything about photoconversion and making PADME-seq a reality but also for being an amazing role model showing that rigorous science is 100% compatible with being the soul of the party when needed! To Paula for directing the best microscopy core ever! I have learnt so much from you. We cannot thank you enough for being constantly working to make our research easier and more robust, but also for caring about us and our projects and be always willing to discuss and interconnect us so that we can grow as a team!

Thank you also to my fellowship program from La Caixa for their support during these years. Not only for funding my PhD but also to introduce me to the “comunidad de

becarios". I have met incredible people during these years that I am lucky enough to call them friends if not family. From flat mates to covid-buddies we have all seen each other grow in their fields and supported each other and attended thesis defenses even when we had no idea of what they were talking about. We generated a small family ready to try every (allergy friendly) restaurant in the city, go on improvised trips despite the weather, wedding dress shopping or organizing the perfect bachelor/ette gateaway! Thank you guys for being always there.

I would like to thank also to all my former mentors, lab mates, "mama pata y patitas" I worked with along the way. Each one of you have contributed to me being the scientist and the person I am today, thank you.

To all my friends in Spain that despite the distance we keep being present in our lives even if that implies hearing my podcasts and audiobooks in whatsapp. It is great to know nothing has changed and we are all there for each other just a phone call away.

Gracias a mi familia, en especial a mis padres por darme la educación que me dieron y apoyarme en todo momento. Por criarme sin limitaciones sobre "que quería ser"; porque gracias a ellos tengo el gran privilegio de trabajar en algo que me apasiona. Al resto de mi familia y en especial a mi tía Raquel por mover cielo y tierra cuando vamos para poder pasar tiempo juntos y hacernos más fácil vivir fuera. También agradecer a mi familia política por convertiros en familia real y apoyarme como lo harían mis padres; aunque eso implique que me haya llevado a vuestro hijo al otro lado del mundo. ¡No puedo estar más orgullosa de la familia que tengo!

Por último y más importante dar las gracias a mi compañero de aventuras, vida y mudanzas. Alex este sueño no habría sido posible sin tu apoyo. Gracias por dejarlo todo y creer en mí y en nuestro Proyecto de vida. Gracias por celebrar mis victorias y compartir las derrotas, por entenderme y ser mi lugar de calma cuando más falta me hace. Juntos hacemos el mejor equipo y estoy deseando de vivir mil aventuras más mientras sean a tu lado.

Abbreviations

4T07	Murine model of TNBC
APC	Antigen presenting cell.
B16F10	Murine model of melanoma
BM	Bone Marrow
BM-DC	Bone marrow derived dendritic cells.
CAFs	Cancer associated fibroblasts.
cDC	Conventional Dendritic cells
CODEX	Co-detection by indexing
CPM	Counts per million mapped reads.
D2A1	Murine model of TNBC
DAMPs	Damage associated molecular pattern.
ECM	Extracellular matrix
EdU	5-Ethynyl-2'-deoxyuridine
EGFP	Enhanced green fluorescent protein.
EMT6	Murine model of TNBC
FFPE	Formalin-Fixed Paraffin Embedded
GO	Gene ontology.
GSEA	Gene set enrichment analysis
GZM	Granzyme
HIF(1a)	Hypoxia inducible factor (1 alpha)
HIF1a STBL	Normoxia stable form of Hif1a
Hif1a-KO DC	Mice with Hif1a KO restricted to cDC.
ICB	Immune checkpoint blockade
IFNAR1	Interferon alpha receptor 1
IMDM	Iscove's Modified Dulbecco's Medium
INF(g)	Interferon (gamma)
IRES	Internal Ribosome Entry Site
Jedi	Just EGFP death inducer
KO	Knock Out
(t)(d)LN	(tumor)(draining) Lymph Node

LPS	Lipopolysaccharide
MDSCc	Myeloid derived suppressor cells
MHC	Major histocompatibility complex
MMP	Metalloproteases
MRD	Minimal Residual Disease
mregDCs	Antigen loaded dendritic cells.
mTNBC	metastatic Triple negative breast cancer
NK	Natural killer
ORR	Overall response rate
OVA	Ovalbumin
p27k	Truncated and inactive form of p27 protein
PADME	Photo-conversion of Areas to Dissect Micro-Environments
PAMPs	Pathogen associated molecular pattern.
pCR	Pathologic complete response
QCC	Quiescent cancer cell
ROIs	Regions of Interest
scRNAseq	single cell RNA sequencing
TAMs	Tumor associated macrophages.
TCR	T cell receptor
Teff	Effector T cells
Texh	Exhausted T cells
TILs	Tumor infiltrating lymphocytes.
Tint-exh	Intermediate exhausted T cells
TME	Tumor microenvironment
TNBC	Triple Negative Breast Cancer
TPM	Transcripts per million
Tprog-exh	Progenitor exhausted T cells
Tregs	Regulatory T cells
Tterm-exh	Terminally exhausted T cells
WT	Wild type

Table of contents

SUMMARY

Immunotherapy is a promising treatment for Triple-Negative Breast Cancer (TNBC), but many patients relapse or do not respond, highlighting the need to understand mechanisms of resistance. In this doctoral thesis we discovered that in primary breast cancer, tumor cells that resist T cell attack are quiescent. These Quiescent Cancer Cells (QCCs) form clusters with reduced immune infiltration. They also display superior tumorigenic capacity and higher expression of chemotherapy resistance and stemness genes. We adapted single-cell-RNA-sequencing with precise spatial resolution to profile infiltrating cells (stromal and immune cells) inside and outside the QCC niche. This transcriptomic analysis revealed hypoxia-induced programs and identified the presence of more abundant exhausted T-cells, tumor-protective fibroblasts, and dysfunctional dendritic cells inside clusters of QCCs. This uncovered differential phenotypes in infiltrating cells based on their intra-tumor location with respect to QCCs. We were also able to identify HIF1a expression in QCC as the driver of immune exclusion and dysfunction. Forced activation of a HIF1a program in cancer cells recapitulated the immune phenotype observed in the QCCs' niche. Thus, QCCs constitute immunotherapy-resistant reservoirs by orchestrating a local immune-suppressive milieu that blocks DC activation impairing T-cell function. Eliminating QCCs holds the promise to counteract immunotherapy resistance and prevent disease recurrence in TNBC.

RESUMEN

La inmunoterapia es un tratamiento prometedor para el cáncer de mama triple negativo (TNBC), pero los pacientes recaen, lo que destaca la necesidad de comprender los mecanismos de resistencia. En esta tesis doctoral hemos descubierto que, en el tumor primario de cáncer de mama, las células tumorales que resisten el ataque de los linfocitos T son quiescentes. Las células cancerosas quiescentes (QCC) forman nichos con baja infiltración inmune. Estas células QCC exhiben mayor capacidad de regenerar tumores

y tienen un perfil de expresión génica relacionado con resistencia a quimioterapia y pluripotencia. Adaptamos la secuenciación de ARN unicelular para obtener también una resolución espacial precisa que nos permitiese analizar los infiltrados dentro y fuera del nicho de QCC. Este análisis transcriptómico reveló la inducción de programas relacionados con la hipoxia e identificó células T más agotadas, fibroblastos supresores y células dendríticas disfuncionales dentro de las áreas de QCC. Esto pone de manifiesto los fenotipos diferenciales en las células infiltrantes según su ubicación intratumoral. Fuimos capaces además de identificar la activación HIF1a específicamente en las QCC como el responsable del fenotipo de exclusión y disfuncionalidad inmune. La activación forzada de HIF1a en células tumorales era suficiente para recapitular el fenotipo observado en las áreas con QCC. Por todo esto, hemos demostrado que las QCC constituyen reservorios resistentes a la inmunoterapia al orquestar un medio inmunosupresor hipóxico localizado que bloquea la función de las células dendríticas y por tanto de los linfocitos T. La eliminación de las QCC es la clave que promete contrarrestar la resistencia a la inmunoterapia y prevenir la recurrencia de la enfermedad en el TNBC.

RESUM

La immunoteràpia és un tractament prometedor per al càncer de mama triple negatiu (TNBC), però els pacients recauen, fent destacar la necessitat de comprendre els mecanismes de resistència. En aquesta tesi doctoral hem descobert que al tumor primari de càncer de mama, les cèl·lules tumorals que resisteixen l'atac dels limfòcits T són quiescents. Les cèl·lules canceroses quiescents (QCC) formen nínxols amb baixa infiltració immune. Aquestes cèl·lules QCC exhibeixen més capacitat de regenerar tumors i tenen un perfil d'expressió gènica relacionat amb resistència a quimioteràpia i pluripotència. Hem adaptat la seqüenciació d'ARN unicel·lular per obtenir també una resolució espacial precisa que ens permetés analitzar els infiltrats dins i fora del nínxol de QCC. Aquesta anàlisi transcriptòmica va revelar la inducció de programes relacionats

amb la hipòxia i va identificar cèl·lules T més esgotades, fibroblasts supressors i cèl·lules dendrítiques disfuncionals dins de les àrees de QCC. Això posa de manifest els fenotips diferencials a les cèl·lules infiltrants segons la seva ubicació intratumoral. Vam ser capaços a més d'identificar l'activació de HIF1a específicament a les QCC com a responsable del fenotip d'exclusió i disfuncionalitat immune. L'activació forçada de HIF1a en cèl·lules tumorals era suficient per recapitular el fenotip observat a les àrees amb QCC. Per tot això, hem demostrat que les QCC constitueixen reservoris resistents a la immunoteràpia en orquestrar un micro-ambient immunosupressor hipòxic localitzat que bloqueja la funció de les cèl·lules dendrítiques i per tant dels limfòcits T. L'eliminació de les QCC és la clau que promet contrarestar la resistència a la immunoteràpia i prevenir la recurrència de la malaltia al TNBC.

1. INTRODUCTION

1.1. Tumor immune micro-environment

1.1.1. Immune surveillance of tumors across history

P. Ehrlich in 1909 (1) predicted the idea of the immune system playing a role in containing potential carcinomas that would arise during our lifetime. However, the maturation of the idea had to await the development of the immunology field. In 1950 the work of Medawar shed light into the concept of allograph rejection helping in the understanding of cellular immunology (2). But the lack of availability of inbred animals together with level of knowledge of cellular immunology made it difficult for the field to prove that rejection was due to anti-tumor recognition and not through allograph rejection. It was not until the 1950s-60s that the tumor immunology field was revisited and gained support (3). They proved tumor antigen existence by immunization with tumor prior to syngeneic tumor transplantation.

All these experiments led to the formal **hypothesis of anti-tumor immune surveillance** proposed in 1957 by Burnet (4) and Thomas (5). This hypothesis stated: "*In large, long-lived animals, like most of the warm-blooded vertebrates, inheritable genetic changes must be common in somatic cells and a proportion of these changes will represent a step toward malignancy. It is an evolutionary necessity that there should be some mechanism for eliminating or inactivating such potentially dangerous mutant cells and it is postulated that this mechanism is of immunological character*".

During the next decades inconclusive experiments due to lack of understanding of the immunological players and their intricate development brought the field to an impasse. It was not until the 90s that the field was resurrected thanks to 2 main contributions: 1) the effect of interferon gamma (IFNg) in controlling tumors was proven (6) and 2) perforin (needed for cytotoxic immune activity) was shown to be necessary for tumor control (7).

The definitive proof the field was looking for came in the 1970s with the development of Rag2 KO animals (that lack mature lymphocytes) in which they could finally demonstrate that carcinogens developed tumors with higher efficiency than in immunocompetent animals.

In parallel, human studies showed indications of immunosurveillance, with higher incidence of neoplasia in immunocompromised patients by AIDS or organ transplantation (8) (9). It was also appreciated that tumor infiltrated lymphocytes (TILs) could be used as a prognosis factor for patient outcome, reinforcing the role of the immune system in cancer (10).

1.1.2. The immunoediting concept

As the immunology field progressed it was clear that the immune system had a secondary unintended role in sculpting tumor development. The elimination of immunogenic cancer cells was also generating that the resulting tumor was formed of cells that were able to escape this killing. Work done in Dr. Schreiber's group in 2001 proved that tumors generated in immunocompetent mice were able to grow in immunodeficient mice (11). However, if the tumors were generated in immunodeficient mice and injected into immunocompetent mice, half of the tumors were eliminated.

As it was clear that the pressure enforced by the immune system is involved in tumor progression and not only elimination; in 2002, Lloyd J Old and Robert D Schreiber proposed the term **immunoediting** (12). Immunoediting refers to the radical role of the immune system across the whole tumorigenic process. It is composed of three phases: elimination (or the previous immune surveillance), equilibrium and escape (Figure 1).

The elimination or immune surveillance step consists in the cooperation of the innate and adaptative immune systems to kill transformed cells. This process involves antigen uptake and presentation by dendritic cells to elicit a cytotoxic immune response.

The equilibrium phase is a Darwinian process in which the cells surviving the elimination phase are contained by the immune system, but their genomic instability generates a pool of heterogeneity that eventually can result in tumor escape. This process happens before clinical detection and is thought to be a slow process that can take up to several years (13).

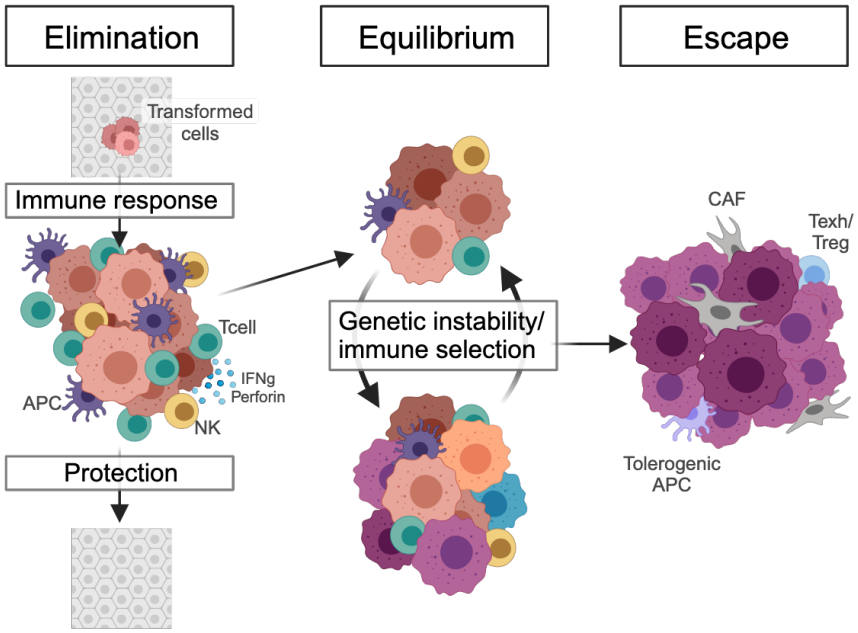

Figure 1. Schematic diagram of the cancer immunoediting hypothesis. The apparition of a malignant cell triggers the immunologic response and induces the elimination phase. If malignant cells resist this attack, they enter in an equilibrium phase where both tumor and immune system modulate each other. In this process the malignant cells able to escape the immune system will be selected and grow, producing the clinical tumors. Image modified from (12).

If the tumor gets to the escape phase it means the balance has tilted to the tumor side and there is a clinically detectable tumor. A lot of work has been done trying to identify the escape mechanisms from immune recognition. A recent review (14) categorizes tumor escape mechanisms as follows:

- **Resistance to cytotoxicity**: this includes direct mechanisms to survive CD8 and natural killer (NK) cells kiss of death by upregulation of BCL2 (antiapoptotic protein) or SerpinB9 (inhibits granzyme (GZM) mediated killing).
- **Limited recognition and inefficient antigen presentation**: this is probably the most obvious pathway when considering tumor-immune dynamics. Downregulation of genes in the major histocompatibility complex I (MHCI) and the

antigen presentation pathway in tumors or even in antigen presenting cells (APCs), is the straightest path to immune evasion. Downregulation of co-stimulatory molecules in APCs as well as upregulation of checkpoint blockade moleucles are also well-known mechanisms that could be included in this category.

- **Formation of an immunosuppressive microenvironment**: it is well documented that chronic inflammation leads to the accumulation of Tregs, myeloid-derived suppressive cells (MDSCs), suppressive macrophages and with them immunosuppressive molecules such as TGFb, Il10 or VEGFa. More recently, there has also been an increase in literature highlighting the importance of nutrients and their low availability in tumor microenvironment. Scarce resources and immunosuppressive signals limit an effective immune response.

The immunoediting concept and its implications highlight the sine qua non of understanding the tumor immune microenvironment (TME) if we want to put an end to the escape phase of tumor immunoediting.

1.1.3. T lymphocytes in tumors

T lymphocytes or T cells are the cellular mediators of immunity. They develop from a lymphoid progenitor in the bone marrow and suffer a maturation and selection process in the thymus, hence the T. Their importance in tumor control became clear with the validation of the immunosurveillance hypothesis. TILs in general and CD8+ specifically were very early on used as a prediction marker for patient outcome (10).

T lymphocytes present two major subsets: CD4+ or T helper cells that as their name states help to direct and mount a specific immune response; and CD8+ or cytotoxic T cells that have the capacity to directly eliminate the cells they recognize. This cytotoxic capacity is what makes CD8 T cells of special interest in the field of tumor immunology since they have the potential to recognize and eliminate tumor cells.

Naïve CD8+ T cells become activated by their interaction with APCs. APCs will give three ques to T cells that will determine the fate of the response (Figure 2) (15). The first signal is antigen itself, through the interaction of T cell receptor (TCR) with peptide-loaded MHCI. This interaction determines the specificity of the mounted immune response. The second signal is through secondary receptors that are co-stimulatory molecules, which reinvigorate and stabilize signal 1 interactions. Signal 3 is the cytokine milieu in which the response is happening and that will dictate the type and strength of the response.

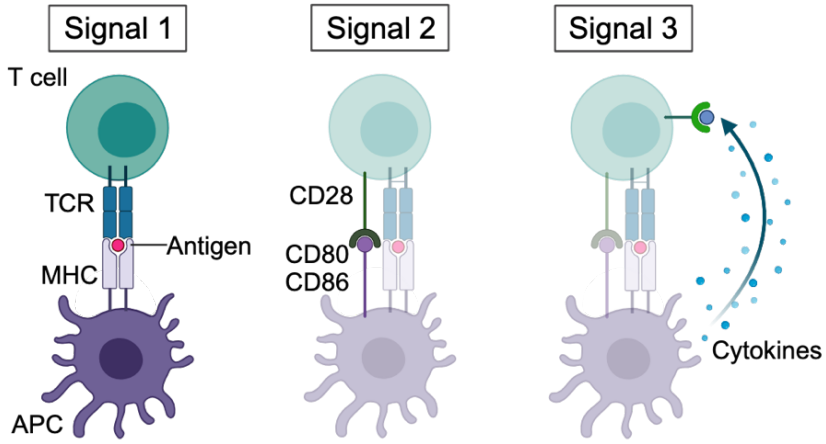

Figure 2. Schematic diagram of T cell activation. Activation of naïve T cells is a process that combines 3 signals: 1) interaction of TCR with antigen loaded-MHCI, 2) co-stimulatory molecule binding and 3) chemokine milieu. Image modified from https://www.jci.org/articles/view/31720/figure/1.

CD8+ T cell exhaustion and other functional states in tumors

In an optimal response naïve CD8 T cells will become active and change to the rapidly proliferative phenotype effector T cells (Teff). As the antigen is being cleared a non-proliferative population will emerge. These are the memory precursor cells that will become long lasting memory cells (16). Memory cells will be easily activated upon antigen exposure to rapidly respond to recurring threats.

However, in chronic antigen exposure such as in viral infections CD8+ T cells acquire an effector function that gets lost as the infection persists. The activated CD8 T cells start losing production of IL-2 as well as their cytotoxic capacity and proliferation capacity (17).

This phenotype is known as exhaustion (Texh). These features of exhaustion have also been observed in CD8+ T cells in the TME (Figure 3) (18).

Exhausted T cells are less proliferative and less cytotoxic than Teff, but they are still active (19). There are different degrees of exhaustion, and it is important to differentiate them and understand the molecular mechanisms driving these stages. There are already some well stablish markers as Tim3 that is known to be present in the most dysfunctional population of Texh (18) (20); or PD1 that is known as an early driver of tumor exhaustion (we will talk more about PD1 in section 1.5 of this introduction). The main stages of T cell exhaustion that have been identified in all studies are (Figure 3) (16) (18) (21):

- **Progenitor exhausted:** The most active population with capacity to be reinvigorated by PD1 blockade (a-PD1), proliferate, and show effector activity is progenitor exhausted (Tprog-exh). These cells are characterized by the expression of TCF1 and can produce cytolytic cytokines as IFNg, TNFa or GZMB.
- **Intermediate exhausted:** The next degree of exhaustion (Tint-exh, exhaustion intermediate) is harder to characterize because it has a heterogenic response with higher expression of TOX but showing also partial response to reinvigoration by a-PD1. Their response will most probably be determined by the environmental ques they receive in the moment of re-activation.
- **Terminally exhausted:** The worst degree of exhaustion, terminally exhausted (Tterm-exh), are cells with low proliferative capacity that are no longer able to be reactivated. They are characterized by $PD1^{High}$ Tim3+ markers, GZMA production which might indicate some cytotoxic activity and CCL3, CCL4 and CCL5 production which will lead to increase inflammation as well as tissue regeneration. They can also present CD39 marker which is linked to regulatory effects through the production of adenosine (22).

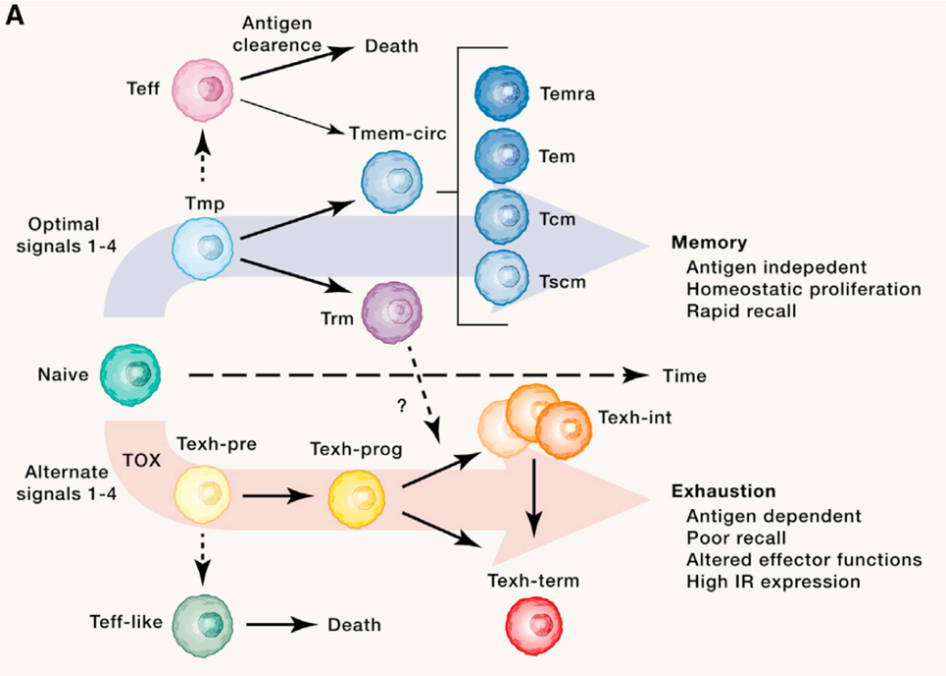

Figure 3. Schematic diagram of T cell activation states. Activation of naïve T cells generates different states according to the type of stimulus, the environmental conditions and antigen persistence. Acute and optimal signals lead to memory formation while chronic antigen exposure and tumor microenvironment lead to exhaustion. Source: (16)

There is also increasing literature linking all this processes with the presence of a 4th signal needed for correct CD8 activation and function, metabolism, and nutrient availability. We will discuss the implications of tumor metabolism in section 1.2.

Antigen specific CD8 T cells in tumor immunology

CD8+ T cells recognize peptides via interaction of their T cell receptor (TCR) to the antigen-loaded major histocompatibility complex I (MHCI). All nucleated cells possess some level of expression of MHCI molecules that are going to expose in their surface small peptides of endogenous produced proteins called antigens. This process was first studied and is easier understood in the context of a viral infection since the antigens are non-self and better stablished (23).

The lack of known antigens was a limitation in the tumor immunology field. Tumor antigens were not proven to exists until the 50s (3) (24) and it was not until the 80s that the field discovered the mechanism of antigen presentation by MHCI expression and TCR recognition. This allowed the confirmation and identification of tumor specific antigens (25) (26).

However, to study tumor-T cells interactions further there is a need to know the antigen but also possess a CD8+ T cell that unequivocally recognizes that antigen. This was solved by the appearance of model antigens such as ovalbumin (OVA) and transgenic mice with expression of specific TCR capable to recognize OVA peptide when loaded in MHCI (OT-I mice).

These studies facilitated and advanced hugely the field of tumor immunology leading to major discoveries on how antigen specific T cells work in a tumor context and how cancer cells protect themselves from this threat (27) (28). Although they present a major confounding factor. As we have seen tumor cells exhibit an important capacity of adaptation partially because of their big heterogeneity formed by genome instability. This means, that during the Darwinian process of tumor survival a clone with antigen loss will rapidly dominate tumor growth. The use of OVA does not allow for the discrimination of cells based on presence of absence of antigen. Therefore, after OT-I treatment it is impossible to differentiate if cells are truly escaping CD8 killing or if they lost the antigen.

In order to solve this problem Agudo *et al* developed a mouse model using the enhanced green fluorescent protein (EGFP) as a visible antigen (29). The mouse presents Just EGFP Death Inducer (Jedi) T cells capable to recognize the immunodominant epitope of GFP loaded in MHCI. The part of the GFP peptide that gets presented in the MHCI molecule of GFP-expressing cells is crucial for the fluorescence of the protein. This means, that as long as the cell is GFP+ the antigen is intact, and the cells can be recognized by the GFP-specific T cells (Figure 4). This allows for unequivocal identification of antigen carrying cancer cells as well as enables identification of small populations of cells thanks to its fluorescence properties. We will use this experimental setting in the results section to characterize resistant mechanisms to CD8+ T cell attack.

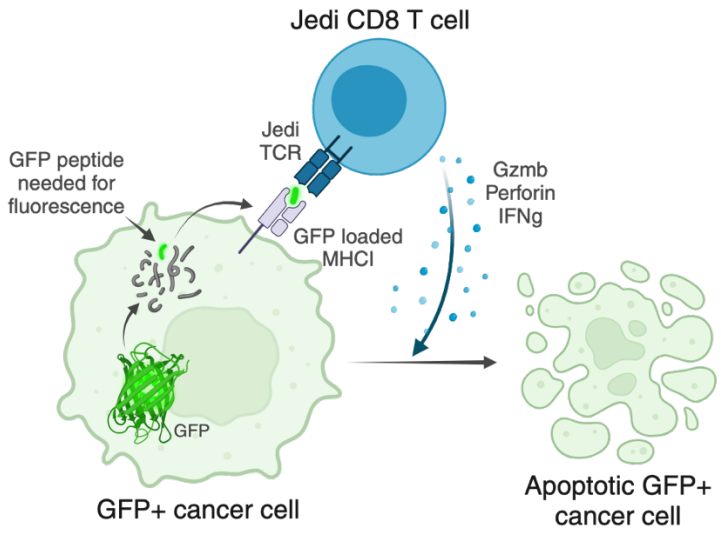

Figure 4. Schematic diagram of Jedi T cell model. EGFP protein when expressed in cells gets presented through MHCI. The immunodominant epitope that gets loaded is crucial for EGFP fluorescence, therefore fluorescent cells will be presenting the antigen. Jedi T cells possess a TCR that will recognize GFP-loaded-MHCI in GFP+ cells inducing Jedi cytotoxic function.

1.1.4. Fibroblasts: suppressive CAFs

Fibroblasts are described as non-immune, non-epithelial cells of mesenchymal origin with a structural function producing and remodeling extracellular matrix (ECM). During wound healing, toxic or metabolic stress, fibroblasts get activated and acquire higher contractability and higher deposition of ECM (30). Activated fibroblasts can be identified by aSma, Pdgfra or Ddr2 markers. This activation process happens also in tumors leading to cancer associated fibroblasts (CAFs).

During wound healing fibroblasts are involved in ECM remodeling to avoid scaring, producing metalloproteases (MMPs) that will help with ECM degradation (30). Chronic activation of the wound healing pathway will alter this process and generate an excessive ECM that leads to fibrosis. Cancer could be considered to this purpose a non-healing wound and therefore will share many characteristics with the fibrosis process. In fact, CAFs signatures correlated to lack of immune infiltration in advanced tumors and include some of these MMPs which indicate ECM remodeling and fibrosis (31) (32).

Fibroblasts are a very plastic population and therefore it is hard to classify them based on states. scRNAseq has allowed the identification of specific markers for pro-tumorigenic fibroblasts. Recently it has been shown that highly activated tumor infiltrating fibroblasts are marked by Lrrc15 expression (32). This population of fibroblasts is not present in healthy tissues and arise in response to continued exposure to TGFb. The identification of Lrrc15 has opened new possibilities to target and modulate CAFs specifically avoiding damage of other healthy tissue architectures. Several groups have also linked this population with T cell exclusion and failure of immune therapies in patients (33) (34).

1.1.5. Dendritic cells in the TME

Conventional dendritic cells (cDCs) were discovered in 1973 by Steinman and Cohn (35) and are known to be the bridge between innate and adaptive immune responses. They are the sentinels that take up, process and present antigens from tissues. They have the capacity to integrate the environmental signals associated with the specific antigen to mount an immune response or maintain immunological tolerance in the body. That is why they are considered “the best support actors of antitumor immunity” (36). In fact, cDC signatures in the TME correlate with better prognosis and response to therapy, even more than the presence of antigens themselves or the so called mutational burden (37) (38).

cDC arise in response to Flt3l from bone marrow (BM) progenitors producing pre-DCs that will leave the BM to reach lymphoid organs (resident cDCs) or tissues. Migration of DCs to tissues happens in homeostasis and intensifies during disease. In the tissues cDCs will uptake and integrate antigen leading to upregulation of migratory program that will bring them to the draining lymph node (dLN) in the search of their matching T cell (Figure 5).

Antigen uptake happens through scavenger receptors as CD205, CD209 or Clec9a. cDCs also possess “Damage and Pathogen Associated Molecular Pattern” (PAMPs and DAMPs) receptors that will help to integrate the environmental ques in order to activate the proper immune response. Their activation leads to enhanced antigen presentation,

increase in the co-stimulatory molecules (CD80, CD86, CD40) and induction of migratory program (CCR7 and Fascin1) (Figure 5).

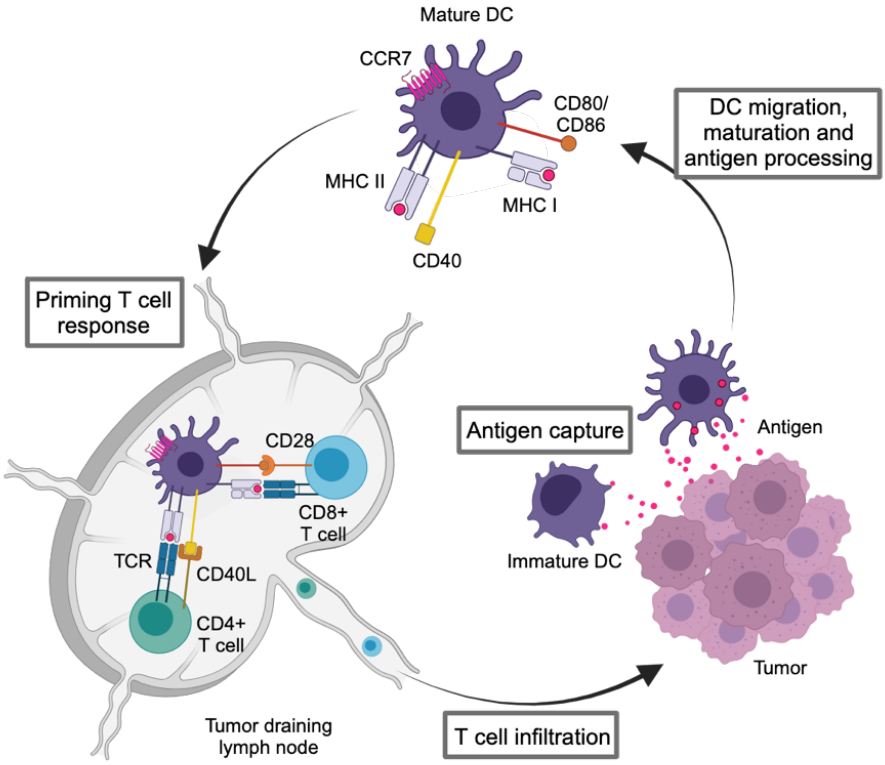

Figure 5. Schematic diagram of DC maturation and T cell priming. Immature cDC arrive to tissues where they get exposed to antigen and environmental ques of inflammation. In response to antigen uptake they upregulate co-stimulatory molecules, antigen presentation machinery and start expression CCR7 that will allow them to migrate to dLN. In the dLN cDC will activate CD8 or CD4 T cells. Imaged modified from Xiao Z et al, (39)

Once in the dLN they wait for a T cell whose cognate TCR binds to their antigen:MHC complex with sufficient avidity. CD80 and CD86 co-stimulatory receptors will help stabilize this synapsis to allow for cytokine exchange. DCs will produce IL12 that is necessary for T cell maturation and T cells will produce IFNg that will re-stimulate cDC.

It has been shown that DCs play a key role in anti-tumor immunity as they are the only cells that carry intact tumor antigens to the dLN (40). Therefore, cDC are also responsible for the vast majority of T cell activation, amplifying further this response by transferring

antigen to LN resident APCs (Figure 6) (41). Just increasing cDC differentiation and activation with Flt3 and the TLR agonist PolyI:C injections, can boost anti-tumor responses in an *a priori* poorly immunogenic tumor setting (40).

However, inside the tumor microenvironment there are many players that can inhibit an immune response by impairing cDC function. Regulatory T cells (Tregs) can directly affect their function by competitively binding CTLA-4 to the DC CD80 or CD86 co-stimulatory receptor since it has a higher avidity than the effector T cell CD28. CTLA4 binding will downregulate CD80, CD86 and will induce also secretion of IDO that will inhibit effector T cell functions (42) (43) (44).

In the TME there are other cells that are well known producers of IL10 and TGFb such as myeloid derived suppressor cells (MDSCs), tumor associated macrophages (TAMs) and Tregs. These suppressive cytokines make cDCs less active and more tolerogenic, but they also activate CAFs that have been reported to directly impair cDC function (45).

Dendritic cell classification and cDC1 importance in TME

cDCs can be further classified as cDC1 and cDC2. While cDC2 are thought to mainly present to CD4 T cells though MHCII; cDC1 present to CD8 T cells through MHCI in a process called cross-presentation. After antigen uptake, CLEC9a activates SYK that helps the rupture of the phagosome releasing antigen into the cytoplasm. This allows for MHCI cross-presentation (46).

cDC1 programs are better understood than cDC2 and it is now clear that they are crucial for proper CD8 anti-tumor response. *Batf3* and *Irf8* are crucial transcription factors for cDC1 development. Animals that lack either of these genes are deficient in cDC1 and are not able to mount a proper immune response or control tumor growth (47) (48). This phenotype cannot be rescued even after adoptive transfer of activated T cells; exposing the importance of cDC1 in anti-tumor T cell immunity.

cDC1 are not only necessary in the dLN but also inside the TME itself to correctly recruit and reinvigorate T cells (Figure 6). Inside tumors they are recruited by NK cells that

produce Xcl1 and Flt3l (49). There they sustain and amplify anti-tumor response by interacting with cytotoxic T cells and producing CXCL9 in response to IFNg stimulation; which helps in the recruitment of additional T cells. Tumor cell killing by cytotoxic T cells releases more antigen and allows cDC1 to go back to the dLN and sustain the immune cycle in the TME. This cDC1-CXCL9-T cell axis is crucial for the response to the immune therapies (50).

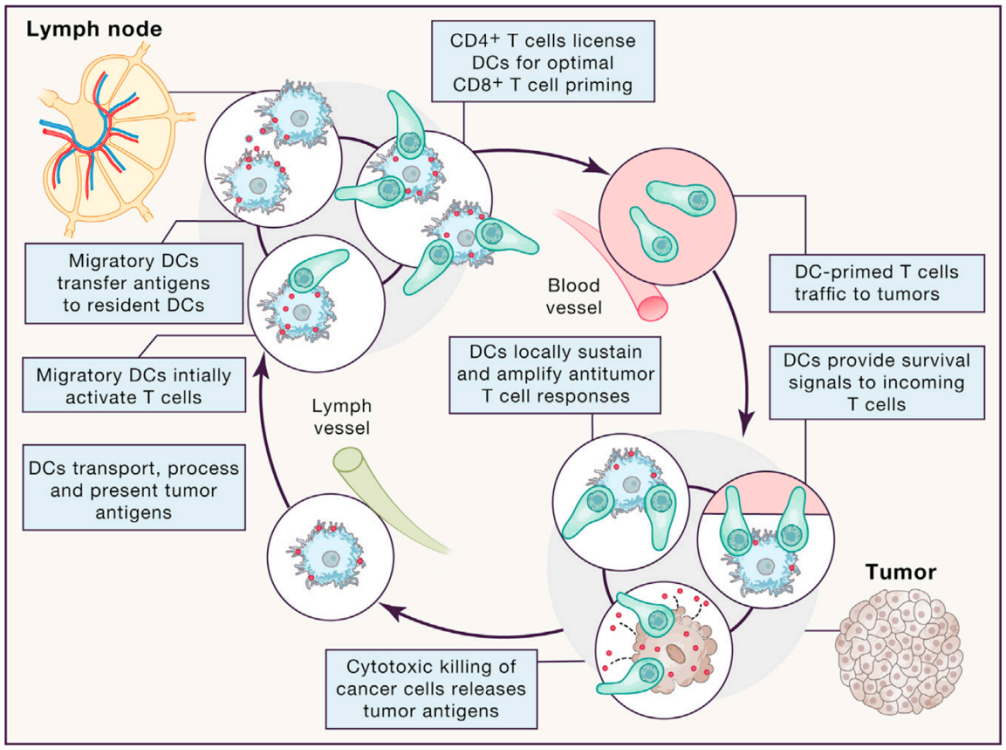

Figure 6. Schematic diagram of cDC roles and implications in anti-tumor immunity. Source: (39)

Antigen-loaded DCs and their role in anti-tumor immunity

Although upon antigen uptake and activation DCs upregulate migration programs not all of the DCs go back to the dLN. Some of them stay in the perivascular space to recruit and reinvigorate lymphocytes entering the TME (Figure 6). This cell state has been independently found and described as DC3, CCR7+ DC, Lamp3+ DCs or mregDCs (51) (52) (53) (54). After DC1 and DC2 activation their transcriptomic profile changes and they lose expression of key markers such as CLEC9A or XCR1. In exchange they upregulate

antigen presentation and migration programs as well as immunomodulatory molecules. In this thesis we will refer to antigen-loaded dendritic cells as mregDCs.

cDCs have been shown to upregulate *Cxcl16* to retain and attract T cells, increase IL12 production to stimulate NK and T cell responses, and produce IL15 to increase T cell survival (55) (54) (56). They are therefore key players in the TME that help in licensing T cells. Their presence is essential for immune therapies to work; hence they have been correlated with a better outcome and response in patients.

1.2. Tumor metabolism

Tumor metabolism plays a critical role in shaping the TME. Oncogenic transformation is known to rewire the metabolism of cancer cells. This phenotypic change, together with the limited and sometimes deficient vascularization, introduces three main challenges for the TME: low oxygen availability or hypoxia, nutrient starvation, and accumulation of waste products. Immune cells have to compete for nutrients with the rapidly proliferating cancer cells as well as adapt their metabolism to survive in that environment.

1.2.1. Abnormal vascularization and hypoxia

Hypoxia, or low oxygen levels, is a characteristic feature of the TME. It was initially thought that the main contributor to hypoxia in the TME was the rapid proliferation of cancer cells that outpaced the development of vasculature. Stabilization of the hypoxia inducible factor 1 (HIF1a) was detected in foci that were more prevalent near necrotic areas (57). While initial activation of HIF1a is probably due to lack of oxygen, this induces angiogenesis that in this specific context further aggravates the problem.

HIF1a induces expression of VEGFa among other angiogenic factors that induce vascularization. However, in the TME the high and chronic expression of VEGFa leads to aberrant and leaky vessels. The formation of poorly functional vessels increases the lack of oxygen and nutrients as well as favors the spread of tumors to circulation. This was

found when drugs blocking VEGFa, that were initially thought to block tumor growth by nutrient starvation, actually helped restored a better vascularization of the tumor. VEGFa blockers are therefore great options to implement in combination therapy to increase drug delivery and facilitate immune cells arrival to tumor.

Induction of HIF1a in the TME has also been associated with expression of immunosuppressive molecules such as TGFb. HIF1a additionally promotes metabolic remodeling since it regulates almost every enzyme in the glycolysis pathway (57). It also manages glucose abundance by controlling glycogen synthesis and breakdown. The activation of glycolysis and blockage of the Krebs cycle (because of the need of oxygen) leads to the accumulation of lactate. HIF1a therefore also induces lactate transporters (58) in order to eliminate this waste product and maintain stable cytosolic pH levels. However, this will generate the acidification of the interstitial fluid of tumors.

Hif1a and oxygen deprivation in immune function

Oxygen availability in the TME is scarce as tumor progresses, so hypoxia is one of the main metabolic components of the TME. Hypoxic responses are regulated by Hypoxia inducible factors (HIFs). An in-depth discussion of the HIF activation mechanism and its effect in tumor cells can be found in section 1.4.2.2. of this introduction. In this section we will focus on the effect of hypoxia and HIF activation in tumor infiltrates.

There is an increasing body of literature correlating HIF activation and immune suppression (59). CAFs with HIF1a activation have been shown to upregulate an immune suppressive signature with expression of TGFb, several MMP proteins and the immunomodulatory molecule PD-L1 (60). PD-L1 (which dampens the immune response by blocking signal 2 in T cells) can be directly upregulated by HIF1a in both tumor and immune cells (61).

Paradoxically, HIF1a induction in T cells seems to augment their cytotoxic activity against tumors, increasing their proliferation and IFNg production (62) (63). Even if hypoxia does not affect cytotoxic T cell function, T cells inside the hypoxic TME are observed as

dysfunctional. Hypoxic signatures are also correlated with worse prognosis (64) and immune therapy failure (65). This could suggest a role for hypoxia in the upstream regulators of the immune response, the dendritic cells.

The effect of hypoxia and HIF induction in DCs has not been as well studied as in other cell types. However, most studies point to a beneficial role of HIF1a induction in DC activation. After DC activation HIF1a levels are increased more than the stabilization seen in hypoxic conditions (66). It has also been reported that some crucial molecules upregulated after antigen uptake such as IL-12 and IL-22 are dependent of HIF1a stabilization (67). A more recent study highlighted the importance of HIF1a in DC migration to the dLN by boosting the glycolysis pathway (68). Perhaps the contradictory roles of HIF1a and hypoxia in immune function and its effect in the TME is explained by the nutrient deprivation observed in this environment.

1.2.2. Glycolysis and nutrient deprivation

Nutrient consumption is dictated by the necessities of the cell state. For activation, immune cells require an extra boost of energy, that makes them turn from oxidative phosphorylation (OXPHOS) to aerobic glycolysis (16) (69). In cDCs sustained levels of glycolysis are needed both for maturation and function (70). Enhanced glycolytic activity has been observed to appear after antigen uptake, to increase during late activation by HIF1a upregulation of Glut1, and to be needed during DC-T cell interactions.

T cell activation requires an exponential increase of their biomass through proliferation. This process requires a metabolic switch from the mitochondrial respiration of naïve T cells to an enhanced glycolysis. Teff metabolic demands are in contradiction to the nutrient landscape found in the TME. In healthy tissues there are cooperative and complementary metabolic relationships but in tumors nutrient competition is fierce (16). The scarce nutrient availability forces TILs to adapt (Figure 7). Texh metabolism is altered with reduced mitochondrial mass and function, low oxygen consumption and increased ROS generation (71). Texh start the metabolic changes after PD1 signaling inducing them

to rely on lipid metabolism which makes them increase in catabolism, autophagy and lipid import (72). These metabolic changes are enhanced as they get to a more Tterm-exh state.

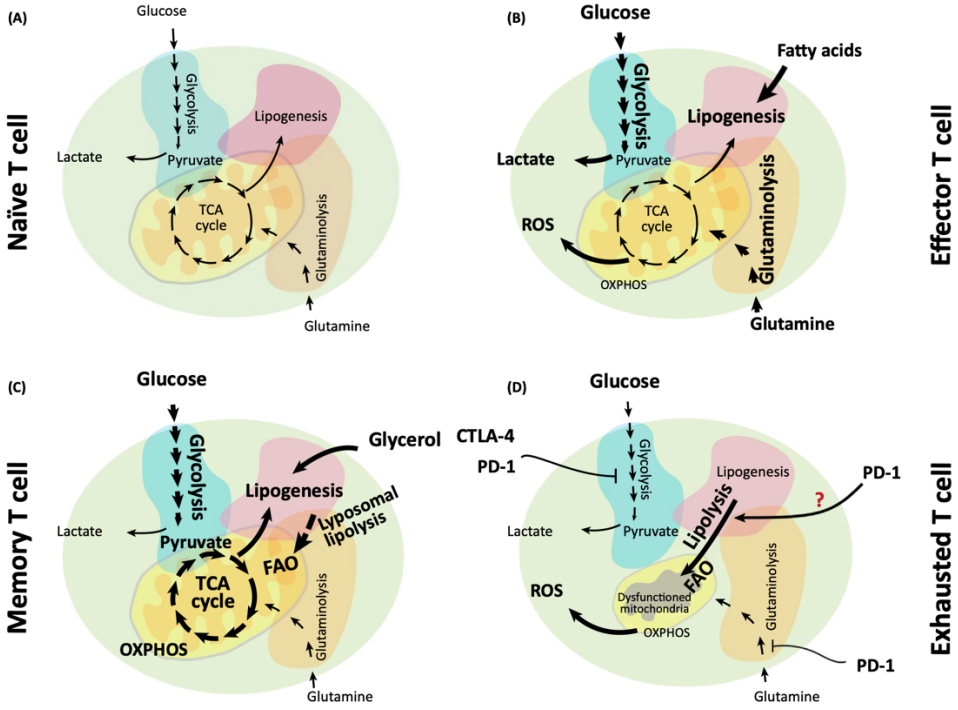

Figure 7. Schematic diagram of metabolism at different T cell states. Source: (73)

1.2.3 Waste products: lactate accumulation

The high glycolytic activity in the TME leads to elevated lactate and lactic acid accumulation. Lactate has been seen as a waste or bystander product but there is an increasing body of literature highlighting its complex and important role in immune regulation (69). Lactate is a known inhibitory molecule for T cells. It has been shown that in tumors with reduced lactate concentration due to low levels of LDHA (the enzyme that catalyzes the reaction from pyruvate to lactate) there is better T cell infiltration and tumor control (74).

Lactate can also influence cDC function. A recent study shows that lactate stabilizes HIF1a in cDC which helps reduced autoimmunity in the central nervous system. In the

TME lactate accumulation has been correlated to impaired cDC differentiation and maturation by decreasing MHCII and co-stimulatory molecules, as well as reduced migration (75).

However, the molecular mechanisms of lactate mediated immune regulation are still unclear. There are well known lactate transporters inside the solute carriers family (SLC) that are also present on immune cells. *Mct1* or *Slc16a1*, *Mct2* or *Scl16a7,* and *Mct4* or *Scl16a3* are the main lactate transporters genes (69). Lactate transport works in both directions emphasizing the need of cells to sense lactate concentration in the environment and the potential role of lactate as an immune regulator. While MCT1 and MCT2 primarily work on lactate import, MCT4 is predominantly involved in lactate secretion (76). Alterations of these lactate transporters can impact cDC function and boost the immune response in the TME, highlighting the role of lactate as an immune regulator (77).

1.3. Spatial analysis of the TME

Single-cell techniques have revolutionized biology by allowing the discovery of rare cell populations and phenotypes, as well as the characterization of highly heterogenous populations of cells. However, both the localization of each specific cell type inside a tissue and the identification of cell-cell interactions requires spatial information that is lost during the sample processing.

Obtaining a map with both spatial resolution and transcriptional state is crucial to understand the complex reality of tumor microenvironment. Imagine this intricated scene painted by the Spanish artist “El Bosco” (Figure 8a) as an analogy of the real situation in the tissue: if we were to study it with high throughput microscopy, we would get a big picture idea of the general things happening (Figure 8b). But we will fail to resolve all the relationships and details of the different individuals involved. However, with current scRNAseq techniques we can obtain a very detailed idea of the specific state of each character (Figure 8c), but we fail to resolve the big picture if we miss the spatial information that is crucial to set things in a context.

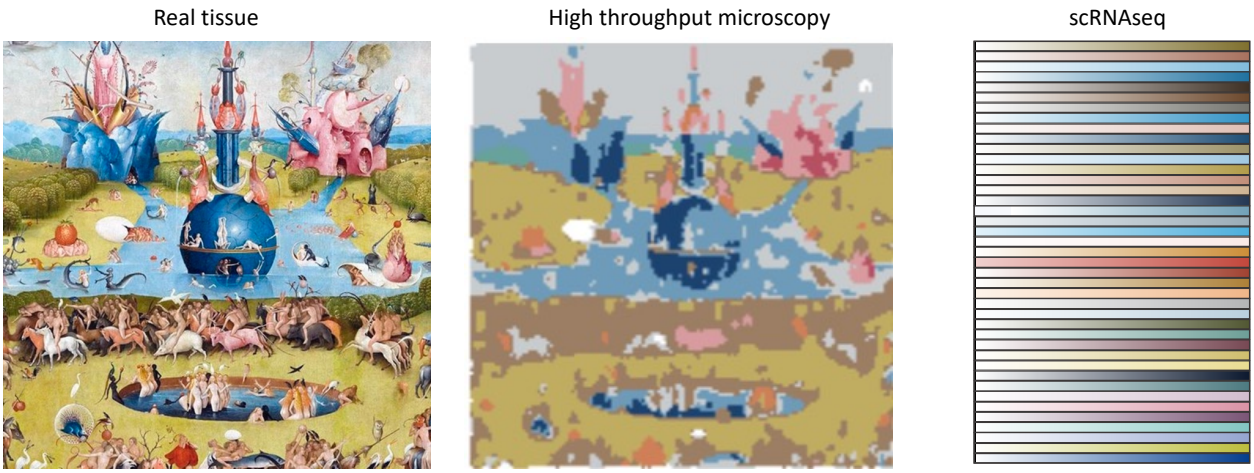

Figure 8. Limitations of current techniques in their approximation of reality. Real tissue or TME is a very complex ecosystem that is represented here in the first panel by an inset of "El Jardin de las Delicias" painting from "El Bosco". The second panel is a representation of how we would visualize such a complex environment if we were to visualize it utilizing solely a limited number of colors. The third panel exemplifies the visualization obtained by current scRNAseq analysis where we would appreciate every single pigment and composition, but ignoring completely the spatial distribution.

In the recent years many different approaches are being developed in order to solve this problem from multiplexed immunofluorescence to the spatial transcriptomics field.

1.3.1. Multiplexed immunofluorescence

Multiplexed immunofluorescence tries to approach the problem by increasing the number of markers to analyze in a single image. They have the advantage of measuring protein, so their readouts are at the latest state of molecular regulation. On the contrary they have a limitation in the number of possible measurements and are considered a targeted technique since the parameters to measure are pre-stablished (antibodies and markers are decided in advance).

Some of the most common multiplexed immunofluorescence techniques:

- **CODEX:** the name comes from co-detection by indexing, and it is based in DNA oligo conjugated antibodies (78). In this method samples are stained with up to 60

conjugated antibodies. Then the sample is revealed by rounds of hybridization of 3 complementary fluorescently labeled oligonucleotides. After every round the previous oligonucleotides are washed, and the developing process is repeated (Figure 9). We will show some quantification of specific immune subsets in distinct regions of the tumor using this method in the Result section.

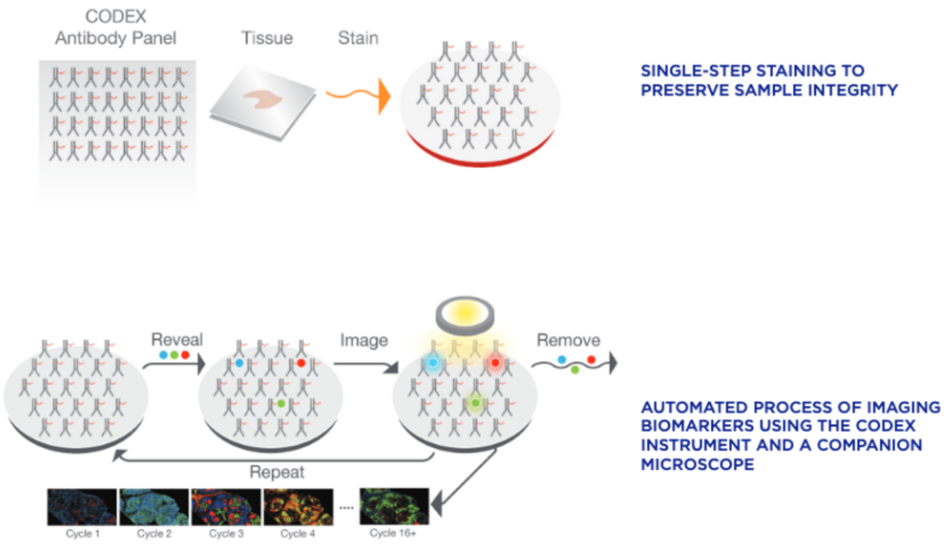

Figure 9. Schematic diagram of CODEX workflow. CODEX tissue preparation starts with a single staining step using all the antibodies. After the staining the developing process occurs in an automated manner, revealing rounds of 3 antibodies at a time by hybridization with fluorescent probes and image acquisition. Source: https://www.scilifelab.se/units/co-detection-by-indexing-codex/

- **CyCIF:** It is a public domain method for cyclic immunofluorescence of up to 30 markers. In this method sample is sequentially stained with groups from 3-6 fluorescently conjugated antibodies. Already attached antibodies are gently inactivated between rounds in order to preserve tissue integrity (79).

- **MIBI:** Multiplexed Ion Beam Imaging conjugates antibodies with heavy metals to fuse imaging with mass spectrometry (80). This technique allows for 30+ antibody single staining and then images are revealed with a TOF mass spectrometer.

1.3.2. Spatial transcriptomics

The field of spatial transcriptomics started a huge expansion in 2016 after the work of Stahl PL *et al* (81) in which they developed for the first time an untargeted method to obtain spatial information of transcripts from a tissue section. Since then, a lot of effort has been made to face the three main challenges: spatial resolution, number of gene transcripts and cost/availability.

- **Microdissection technologies:** This approach requires the use of a laser capture microdissection microscope. Fresh frozen or FFPE slides are micro dissected under the microscope and then sent for RNAseq. TOMO-seq examines the RNA content through tissue sections and allows to examine a specific position across a whole specimen (82). It is easy to implement but lacks single cell resolution.

- **In situ hybridization-based techniques:** These techniques evolved from methods to detect single RNA molecules inside cells such as FISH or RNAscope. They developed different strategies to bypass their main limitation that is given by the number of fluorophores the microscope can detect. These methods possess single cell resolution, but the use of probes makes them a targeted method. The main technique in this category, MERFISH (83), has been shown to recognize 10K genes with 80% efficiency (84). MERFISH's disadvantage lies in the cost, which escalates with the number of probes to be used. It also requires the use of specialized equipment. Since it is a microscopy-based method as the number of probes increases so does the background, reducing the signal to noise ratio.

- **Spatial capturing technologies:** These technologies capture RNA content from tissue and add a barcode based on the spatial location. After the RNA is sequenced, every transcript can be traced to the original location in the tissue using the spatial barcodes (81). Most widely used commercial methods are based on this approach. They allow for whole transcript sequencing, but lack single cell

spatial resolution due to the size of each spatial barcode spot that fits 10-50 cells. 10x Visium is currently the leader in the market and is working to reduce the barcode sites to achieve single cell resolution.

- **Photolabeling based techniques:** The discovery of photoactivable and photoconvertible proteins as PA-GFP and Kaede respectively, allowed for the labeling of specific populations of cells originally intended to track them and study cell migration with live imaging (85). More recently Medaglia C *et al* proposed Niche-seq: a strategy that uses PA-GFP and two photon microscopy to label specific niches of cells which could then be FACS sorted and submitted for scRNAseq (86). This technique allows for true single cell resolution in sequencing but needs a well-defined area to be studied. The use of multiphoton microscopy increases the difficulty and the experimental time.

The different approaches with their respective advantages and limitations allow to the user to pick based on their needs. Out work required true single cell resolution and had a very specific question focusing on well-defined areas of the tumor microenvironment. We developed our own method based on photolabeling based techniques with considerable variations to ease the process and maximize photolabeling.

1.4. Triple Negative Breast Cancer

Breast cancer is the most common form of cancer in women accounting for 30% of patients. Its incidence has been steadily increasing over the past years and is expected to continue in this trend (87). Breast cancers can be further stratified into subtypes according mainly to 3 markers. Triple Negative Breast Cancer (TNBC) is characterized by the lack of all three of them: hormone receptors both progesterone and estrogen as well as HER2 receptor.

TNBC accounts for 15% of total breast cancer cases and it is the most common subtype in women under 40 years old (88). It is the most aggressive, invasive, and proliferative form of breast cancer leading to a bigger portion of breast cancer related deaths than other more abundant subtypes.

1.4.1. Current treatments

The lack of the three principal markers discards the use of targeted therapies such as hormonal therapy and targeted HER2 therapy. As a systemic treatment chemotherapy has been the standard of care before and after surgery. This involves anthracyclines, taxanes, or platinum-based drugs. The main treatment however is surgical resection that could involve partial or total mastectomy. After surgery radiotherapy is also used to eliminate any potential tumor residue. More recently immunotherapy has been approved by the FDA as standard of care in metastatic TNBC and is being evaluated for non-metastatic patients, which will be addressed in depth in the next section.

1.4.2. Recurrence and resistance

Despite all efforts 10% of patients relapse after a successful elimination of the primary tumor. This is a constant observed phenomena throughout history. In 1934 Rupert Willis already proposed the idea of tumor dormancy, referring to undetectable disease persistence. In 1954, Hadfield reviewed this concept and observed that among BC patients, recurrence after 5 years was less common. To this day the 5 years threshold is still used to differentiate early and late recurrence (89). TNBC patients have shorter recurrence time than other BC subtypes, being the fastest and most prevalent one at the local site.

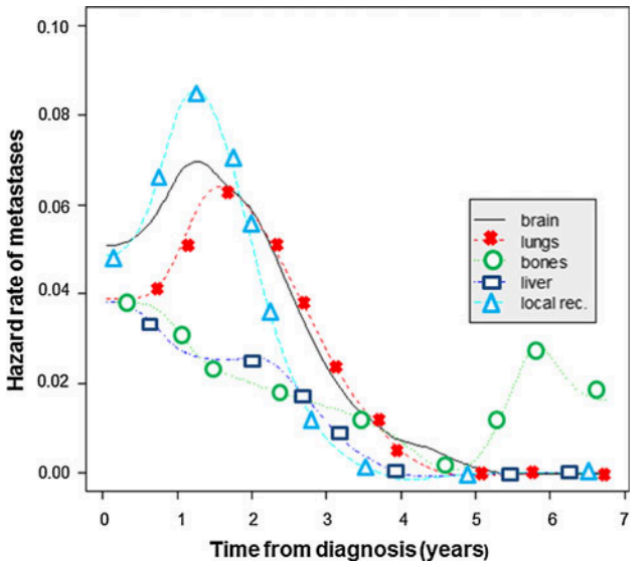

Figure 10. Relapse and metastasis risk in TNBC patients. Graph depicts the hazard rate of recurrence and metastasis in patients with TNBC as a function of time after diagnosis. Source: (90)

This scenario remarks the existence of a microscopic, clinically undetectable tumor that is the source of recurrent events. This is called minimal residual disease (MRD). By its own definition it is almost impossible to study in patients since it would require exhaustive screenings of biopsies. However, there is good evidence of this phenomenon in organ transplants where *a priori* healthy donor organs develop cancerous lesions after the immunosuppression of the organ recipient (9). Another source of evidence is the presence of disseminated tumor cells in bone marrow of breast cancer patients (91). Furthermore, the presence of DTCs has been correlated with shorter recurrence times. The evidence of MRD together with the time it takes for patients to relapse reinforces the proposal of a latent disease or dormancy.

1.4.2.1. Dormancy and stemness

Cancer cellular dormancy was proposed by Aguirre-Ghiso in 2007 as a cellular state to explain disease latency or disease dormancy (92). As explained above dormancy was proposed as a clinical term in which the disease was present but undetectable. However,

this could be explained by different scenarios: 1) the small mass was in an equilibrium state of proliferation and death by lack of vascularization or by the effect of the immune system. 2) Cellular dormancy in which there is either a growth arrest in G0/G1 like state or the cells show an extremely low proliferation rate. Dormant cells can be found in both the primary tumor site and the metastatic site explaining why recurrence can appear as both primary and metastatic independently.

There is growing evidence of slow cycling cells present in the tumor mass as the source of relapse in different cancers (93) (94). It has been well reported that in response to some targeted therapies and chemotherapy there are some persister cells that exhibit dormancy characteristics (95). Study of quiescent cells in the tumor mass by dyes diluted with proliferation has also allowed the identification of cells prone to metastasize (94). These dormant cells are not a clonal selection but rather an epigenetic and metabolic adaptation driven by the damage and the environmental cues. Analysis of patient samples also showed the presence of a dormancy gene signature with differences in enrichment varying from 2% to 30% among patients.

Recently it has also been appreciated the role of the immune system in the induction and maintenance of cellular dormancy. Several studies have pointed to the role of different types of interferon in this process. It has been shown that T cells are necessary for chemotherapy induced dormancy in murine 4T1 orthotopic models of TNBC (96). Similarly, CD8 T cells from murine 4T07 TNBC orthotopic model also induce dormancy in the distant sites (97). Moreover, NK cells induce cellular dormancy in breast cancer through IFNg production (98). In patient clinical samples, IFNb is associated with longer metastasis free survival suggesting cells are kept in a dormant state for longer time (96).

1.4.2.2. HIF1a and persistence

Hypoxia has been associated with cancer aggressiveness, progression, and metastasis (99). Since the discovery of the molecular mechanism governing hypoxia, HIF1a has

been postulated as a signature of persistence (100), marking cells capable to survive treatment and predicting relapse and poor response in patients (64).

In TNBC HIF1a signature is present in all stages even in initial lesions (101) and it is known to rewire metabolism which cancer cells harness to their full advantage as previously described. Some of the molecular markers for breast cancer stem cells as *Ca9* (102) or *Aldh* (103) are induced by HIF and play a role in the generation of the suppressive microenvironment in tumors. This highlights the role of HIF as a master regulator of cells capable of recurrence (so-called “cancer stem cells” by some) (100).

Some of the common mutations of TNBC can induce HIF1a in an oxygen independent manner (104) (105). This explains why HIF1a is particularly high in TNBC patients (106) and why TNBC cancer cells retain hypoxic signatures even in normoxia cultured conditions (107). However, mRNA expression is not altered so the accumulation must be related to the post-translational regulation of HIF1a protein.

Active HIF complex is formed by the union of HIF1b that is constitutively expressed and HIF1a or HIF2a. The HIFa subunits are constitutively expressed but regulated at the protein level by oxygen conditions. PHD proteins hydroxylate two proline and one asparagine residues in HIF1a in the presence of oxygen (P402/P557/N813). The VHL protein will then recognize hydroxylated HIF and ubiquitinate it so that it is degraded by the proteosome. It is therefore possible to stabilize HIF1a in normoxic conditions using a mutated version of the HIF1a protein that cannot be hydroxylated (108). We will refer to this form as HIF1a^{STBL} in the Result section of this thesis.

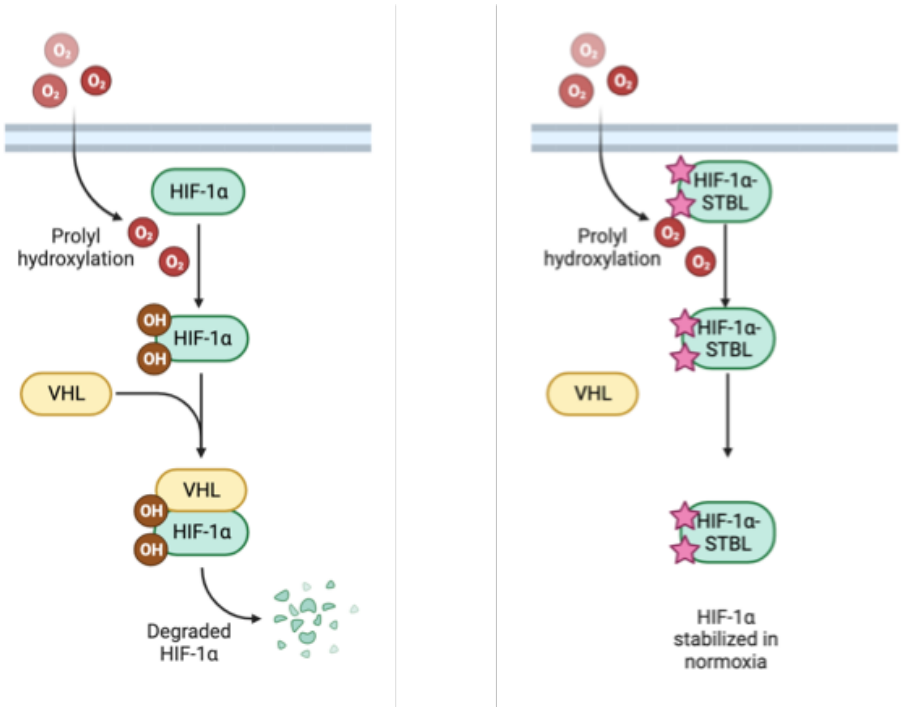

Figure 11. Schematic diagram of HIF1a activation and normoxic stabilization of HIF1a STBL. During normoxic condition in the presence of oxygen (O_2) HIF1a gets hydroxylated. This hydroxylation makes possible the binding of VHL that will mediate HIF1a degradation. HIF1a STBL has point mutations in the hydroxylated residues that avoid such modification. In the absence of hydroxylation the protein can not bind to VHL and is accumulated, even in the presence of O_2.

1.5. Immunotherapy for TNBC

1.5.1. Immune checkpoint blockade

Immunotherapy was named by Science as the breakthrough of the year in 2013. Immune checkpoint blockade (ICB) therapy revolutionized the treatment of uncurable cancers like melanoma (109), opening a new field full of possibilities. Its impact in the advance of cancer treatment was reassured in 2018 when it was awarded the Nobel Prize in physiology and medicine.

Immune checkpoint mechanisms were evolutionary developed as a way to maintain self-tolerance and put breaks to the immune response. They consist of receptor – ligand interactions that dampen the immune response. ICB therapy consists in the use of

monoclonal antibodies that compete for either the receptor or the ligand blocking their union, hence maintaining the immune activation.

The first ICB therapy tested in a phase III study was aCTLA4 (Ipilimumab) in melanoma patients that significantly increased the overall survival (110). During T cell activation in the immunological synapse, APCs present antigen through MHC as signal 1. Then B7 family of proteins in APCs bind to the co-stimulatory molecule CD28 in T cells to activate them (signal 2). CTLA4 is expressed in T cells and competes with CD28 for binding to B7. Blocking CTLA4 will ensure the binding of CD28 to B7 to obtain a successful T cell activation. This interaction is thought to be more relevant at the dLN where the T cell response is being mounted. Blocking this mechanism can lead to loss of self-tolerance and present higher immune related adverse events than other immune therapies.

PD1 is a family member of the CD28 family and acts as a co-inhibitory molecule when binding to PDL1 or PDL2 (members of the B7 family) expressed in APCs. However, non-immune cells and cancer cells can also express it and hijack this mechanism to defend themselves against direct T cell engagement (111). In this case its effect is not on the T cell activation but rather in the effector phase. It has been shown that PD1 signaling is involved in T cell exhaustion and that its blockade can at least partially restore the exhausted phenotype (109). PD1/PDL1 monoclonal antibodies have shown an impressive response in several types of tumors and present less immune related adverse events than CTLA4 blockade (112).

1.5.2. Current status and approval

TNBC presents a great opportunity for ICB since it presents high level of immune infiltration, high mutational burden, and expression of PDL1. Among TNBC patients it was first evaluated as a monotherapy in metastatic patients (mTNBC). mTNBC has very limited treatment options and shows a poor prognosis, and therefore there is a critical need to evaluate potential treatments options.

The first study to evaluate the use of anti-PD1/PDL1 axis was Keynote012. In this study pembrolizumab showed 18.5% overall response rate (ORR) in mTNBC patients. After this Keynote086 (113) (114)(pembrolizumab) and JAVELIN (115)(atezolizumab) showed an ORR of 21.4 and 22% respectively in PDL1+ patients. Another study showed combination of aPD1 with aCTLA4 had a 17% ORR that increased to 43% when analyzing previously treated patients (116). These encouraging results lead to the Keynote355 study for chemotherapy in combination with pembrolizumab. After Keynote355 clinical trial the FDA approved this combination in mTNBC and recurrent unresectable primary TNBC with PDL1 expression (117).

After ICB success in the late stages of the disease it was evaluated in earlies stages. In these studies, the measurement used is pCR that is defined as non-invasive cancer lesion in breast or lymph node tissue. Several studies evaluated a-PD1 in combination with chemotherapy (I-SP42 (118), Keynote173 (119) or IMpassion031 (120)) and they all showed a pCR of 60% in the combo treatment. After the results of Keynote522 (121) the FDA approved the use of pembrolizumab with chemotherapy in high risk TNBC regardless of PDL1 status.

The field is now looking for other combinations that can further boost the results obtained with ICB treatment. One of the most prominent ones is the combination with PARP inhibitors (122). PARP inhibitors have been reported to lead to accumulation of DNA fragments through induction of DNA damage. These are well established DAMPs that will boost the innate immune system to produce type I IFN and activate an immune response. It has been shown that they increase antigen presentation of DCs in the TME. Combination of PARP inhibitor and aPD1 therapy has shown a 47%ORR in mTNBC with BRCA1/2 mutations and a pCR of 47% in early stage TNBC in several studies (123) (124) (125). These results are being further evaluated and highlight the potential of combinatorial ICB treatment to treat TNBC.

1.5.3. Unmet needs

ICB treatment has considerably improved the treatment of TNBC patients. It has given successful and durable therapeutic options to previously unresponsive patients. However, response rates are 20% in metastatic disease and 60% in early stages. There is a lot of room for improvement. It is crucial to understand why therapy fails in order to design new therapeutic strategies. The field is currently evaluating the potential to use irradiation to induce inflammation prior to ICB or vaccines that are capable to generate and sustain an immune response so that ICB can increase its effectiveness (126).

Aside from the margin of improvement there is also a need to obtain better predictive markers for responsive patients. This will help to direct patients to the most suitable therapy and do not lose time with therapies that are destined to fail in their specific case. As of now, the best markers are the presence of PDL1 together with the presence of TILs. However, it is not well understood what drives the presence of absence of TILs and the PDL1 marker is not always a good predictor marker for response. There are in fact some studies in which they found a similar response rat between PDL1 positive and negative patients making it not necessary for evaluation in the treatment of primary tumors according to the FDA.

All this together remarks the need to further understand the interplay between immune cells and cancer cells in the tumor microenvironment as well as their immune evasive mechanisms in order to elucidate therapy resistance. These studies will be crucial for driving new combinatorial therapies that can harness the full potential of immune therapy.

2. HYPOTHESIS AND OBJECTIVES

Immunotherapy is a promising treatment for Triple-Negative Breast Cancer (TNBC). However only a fraction of patients respond, arising the need to understand resistance. Little is known about the ability of the immune system to clear the heterogeneous populations that coexist in a tumor. We hypothesize that inside tumors there might be a resistant population orchestrating a dysfunctional TME that avoids T cell function.

- *Visualization and characterization of immuno-therapy resistant cancer cells in primary TNBC.* Is the immune system able to eliminate the different populations and states of cancer cells in a tumor setting? We will assess the ability of the immune system to clear the heterogenic populations of a tumor using the proposed technology of GFP and Jedi T cells. We will also characterize the surviving populations.
- *Identification of the stroma/immune components within the niche containing immunotherapy resistant cancer cells.* What are the defining features of the stroma and immune populations surrounding immunotherapy resistant cells? We will develop a new scRNA-seq with spatial resolution to characterize the niche surrounding resistant tumor cells.
- *Which are the underlying mechanisms used by resistant cancer cells* to survive immunotherapy. How are tumor cells escaping direct T cell killing? T cell infiltration in tumors is heterogenic tumors but the drivers of this uneven infiltration are poorly understood. We will study the resistant mechanisms used by cancer cells against T cell immunity.

3. RESULTS

Quiescent cancer cells resist T cell attack by forming an immunosuppressive niche.

Baldominos P, Barbera-Mourelle A, Barreiro O, Huang Y, Wight A, Cho JW, Zhao X, Estivill G, Adam I, Sanchez X, McCarthy S, Schaller J, Khan Z, Ruzo A, Pastorello R, Richardson ET, Dillon D, Montero-Llopis P, Barroso-Sousa R, Forman J, Shukla SA, Tolaney SM, Mittendorf EA, von Andrian UH, Wucherpfennig KW, Hemberg M, Agudo J.

Cell. 2022 May 12;185(10):1694-1708.e19. doi: 10.1016/j.cell.2022.03.033. Epub 2022 Apr 20. PMID: 35447074.

My contribution was essential for the publication of this work. I designed all the experimental settings under the guidance of my thesis directors. I performed all the experiments except for those involving clinical data and participated in all the analysis present in this work. I also contributed to a major part of the manuscript writing. The result section of this paper is presented with some extended figures and clarifications.

3.1. GFP as a visual antigen allows to unequivocally detect resistant cells.

To investigate how tumor cells that retain expression of targeted antigen(s) can escape T cell killing, we used anti-GFP specific Jedi T cells (29) in combination with GFP expressing TNBC 4T07 cells (Figure 12). GFP as a visible tumor antigen allows one to distinguish cells that survive T-cell attack and retain antigen expression. This is necessary to differentiate tumor cells that truly developed T cell resistant mechanisms from cells that escaped by antigen loss (GFP-). During tumor implantation and development GFP^- cells acquired an evolutionary advantage and become the predominant clone of the resulting tumor. The immunoediting process will favor antigen loss and as a result bulk analysis of the whole tumor population will mask the underlying mechanisms of antigen carrying tumor cells.

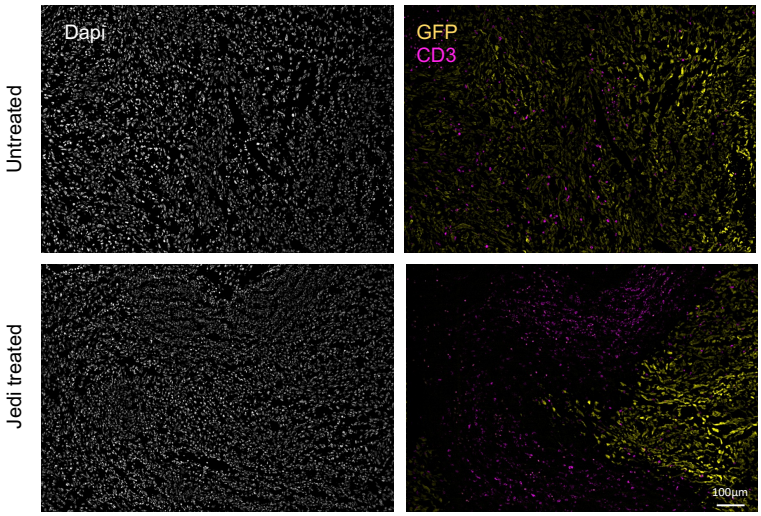

Figure 12. GFP+ cells are a small fraction of tumor cells after Jedi treatment. Representative images of 4T07 GFP+ tumors (n=3 animals per group) for untreated and Jedi adoptive transfer. Immunofluorescence analysis shows Dapi (grey), GFP (yellow) and CD3 (magenta).

3.2. Cancer cells that survive upon adoptive T cell therapy do not proliferate.

In order to study how GFP+ cells escape Jedi T cell killing, we orthotopically injected a mix of GFP+ and mCherry+ cells in mice. Since Jedi T cells do not recognize mCherry, mCherry+ cells constituted labelled controls that were embedded within the same milieu (Figure 13A). We generated PD1-deficient Jedi T cells (PD1-/- Jedi) by crossing with PD1-/- mice (127), so PD1 inactivation was directed only against GFP+ cells. PD1-/- Jedi T cells were transferred at either day 7 or day 15, to capture different stages of tumor growth (Figure 13B). Jedi T cells were traced by CD45.1 staining, expansion was restricted to tumor draining lymph node (tdLN) (Figure 13C).

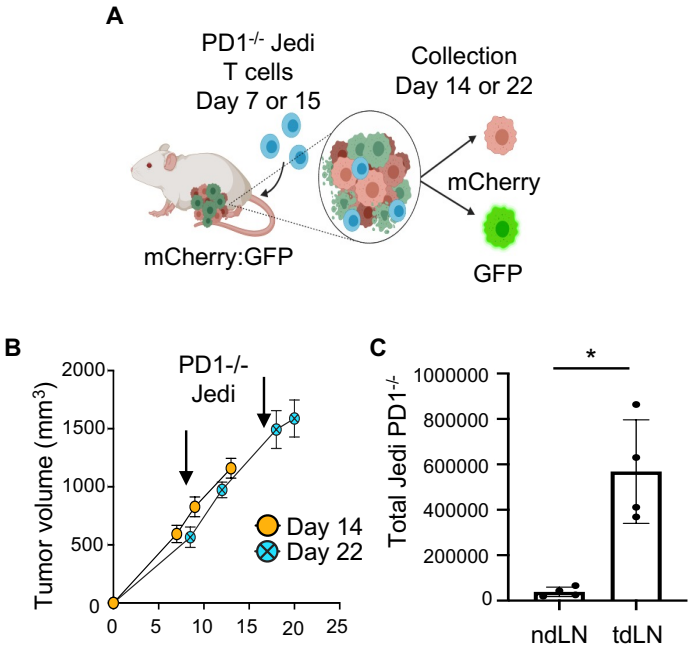

Figure 13. Experimental design to isolate T cell resistant cancer cells. A) Schematic of the experiment: mammary carcinoma was grown with mixed GFP+ and mCherry+ 4T07 cells (1:1). Mice were treated with 7M PD1-/- Jedi T cells at either day 7 or day 15 after tumor inoculation. All mice were analyzed 7 days post-T cell injection B) Tumor growth curves of 2 independent experiment following schematics of A. The mean±sem of the volume is shown. Arrow marks time of T cell injection. C) Jedi PD1-/- quantification (mean±sem) in tumor draining lymph node (tdLN) and distant lymph node

(ndLN) by flow cytometry based on CD45.1 expression that was restricted to Jedi T cells. (n=4 mice). *P<0.05.

PD1-/- Jedi T cells effectively killed most but not all GFP+ cancer cells (Figure 14A, B). To ensure differences in GFP:mCherry ratio were due to Jedi killing we grew same mixture of cells in immunodeficient NSG mice. The GFP:mCherry ratio in NSG mice was close to 1 ensuring there was no growth advantage and the difference was the result of immune pressure (Figure 14C). We also confirmed the GFP:mCherry ratio at day 7 before Jedi treatment when the adaptive immune response is minimal (Figure 14C).

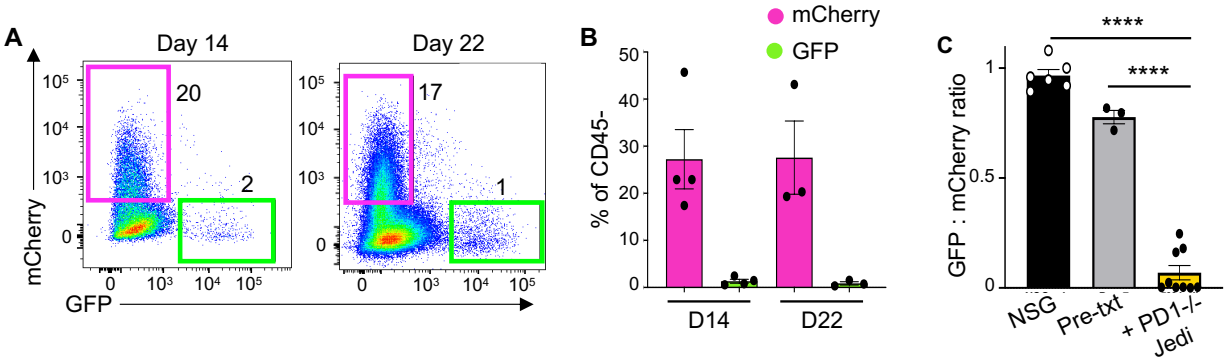

Figure 14. T cell resistant GFP+ cells represent a small fraction that can be identify by flow cytometry. A) Representative flow cytometry plots from tumors in 2A, gated on DAPI- CD45-. (C) Mean±sem of data in A. (n=4). ****P<0.0001.

Surviving GFP+ cancer cells were not scattered in the tumor mass but rather in organized clusters (Figure 15A, B). Immunofluorescence with CD3 and CD45.1 showed that majority of T cells inside the tumors were CD45.1+ Jedi T cells (Figure 15A, B). Images also showed reduced T cell infiltration in GFP+ areas compared to mCherry+ regions, indicating partial T cell exclusion. Quantification of CD3+ infiltrates showed a two-fold reduction in GFP+ regions (Figure 15C). This result demonstrates that mammary carcinomas contain regions with restricted T cell infiltration likely contributing to their resistance to immunotherapy.

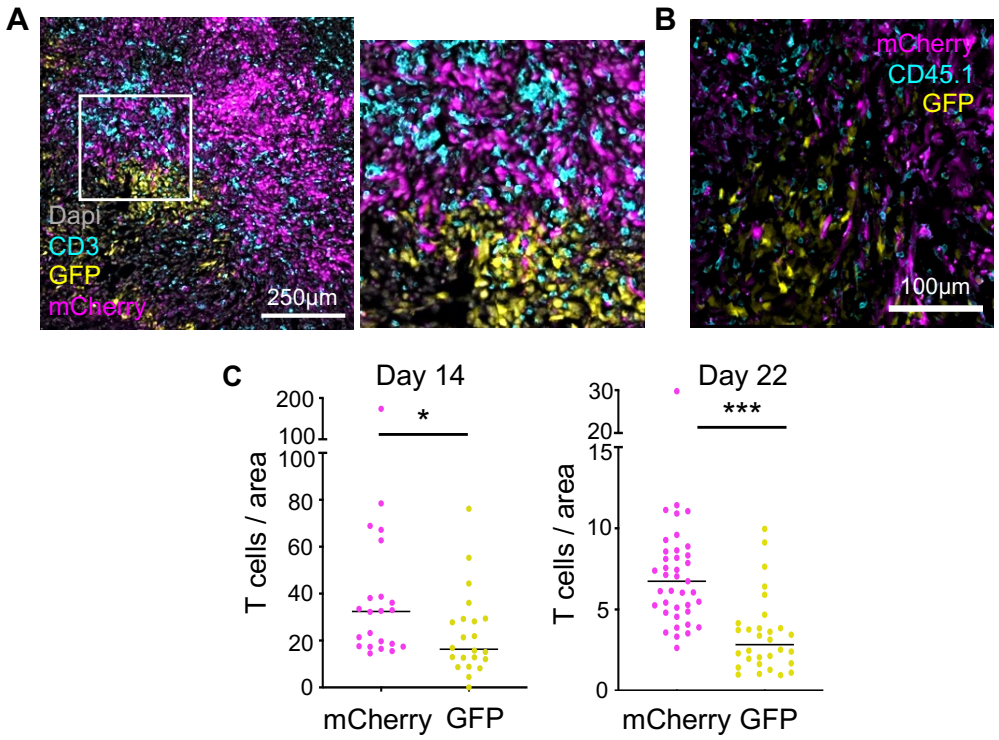

Figure 15. GFP+ resistant cells form clusters that present T cell exclusion. A, B) Representative tumor images from 2A at day 14. A) CD3 immunofluorescence B) CD45.1 immunofluorescence (C) Number of T cells per tumor area from mice in 2A. Bar marks the median (n=3 tumors). *P<0.05, ***P<0.001.

We FACS-sorted GFP+ surviving antigen-expressing cancer cells along with control mCherry+ cells to perform RNA-sequencing (Figure 16A). Principal Component Analysis (PCA) revealed that GFP+ and mCherry+ cells from the same tumors did not cluster together. Instead GFP+ samples from the various tumors were closer to each other than to mCherry+ cells from the corresponding tumor (Figure 16B, C). This provided a good framework to search for differentially expressed genes between GFP+ and mCherry+ cells to uncover mechanisms of resistance to T cell killing.

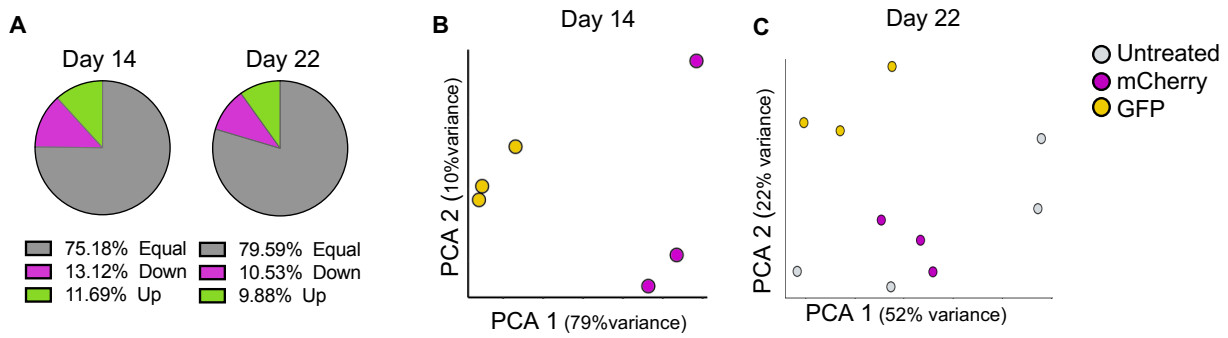

Figure 16. General overview of bulk RNA sequencing from GFP+ resistant cells. A) RNA-sequencing was performed in mCherry+ versus GFP+ cancer cells from tumors in Figure 2A. Pie charts show the percentage of statistically differentially expressed genes. B, C) Principal Component Analysis (PCA) from RNA-seq data from mCherry+ and GFP+ tumor cells from 2A at day 14 (B) and day 22 (C). (n=3-4 mice)

First, we focused on antigen presentation, and found that expression of essential genes in the pathway was not reduced (Figure 17A). Because MHCI was reported to decrease at the protein level in T cell-resistant pancreatic tumor cells (128), we also quantified surface levels of MHCI protein in surviving GFP+ cells (Figure 17B, C). GFP-expressing cells were MHCI positive and had comparable levels albeit a bit higher than their non-targeted mCherry+ counterparts.

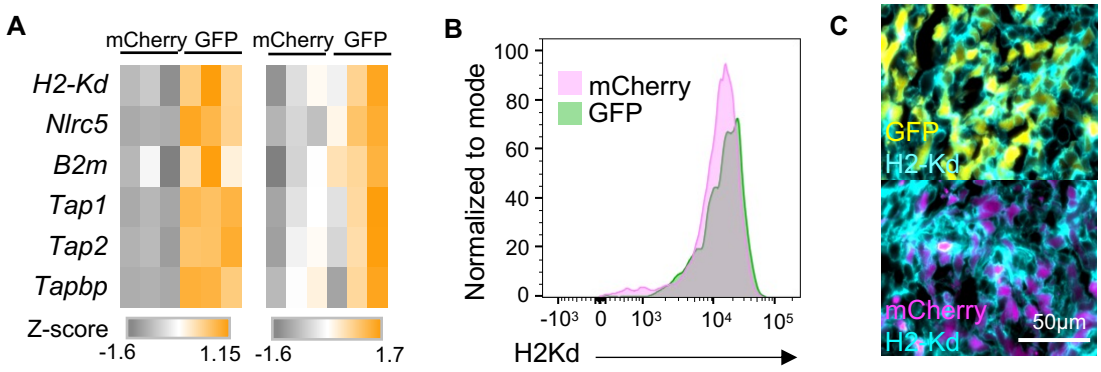

Figure 17. GFP+ resistant cells have intact antigen presentation. A) Heatmap shows key genes in the antigen presentation machinery from mice in Figure 1A. Data is color coded to reflect gene expression Z-scores. B, C) Protein levels of H2-Kd (MHCI) in cancer cells from mice in 2A (n=4 mice).

Measured by flow cytometry (B) or immunofluorescence (C). Representative plot and images are shown (n=3 mice).

We then searched for the highest upregulated genes in GFP+ resistant cells in both datasets of independent experiments. This analysis revealed that the top 10 upregulated genes in the GFP+ population included Ngfr and Aldh1a1 (Figure 18A). These genes have been described as markers that identify a subset of breast cancer cells with enhanced resistance to chemotherapy and stronger tumor initiating capacity, referred to as breast cancer stem cells (129) (130). Car9, another breast cancer stem cell marker (100), was also increased in GFP+ cells (Figure 18A, B).

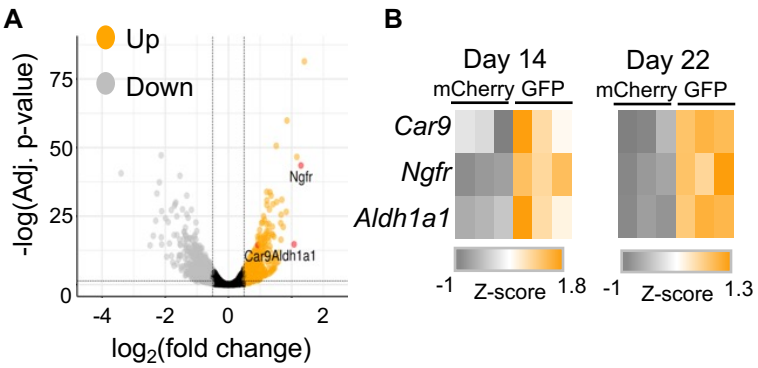

Figure 18. GFP+ resistant cells show upregulation of genes related to chemotherapy resistance and hypoxia. A) Volcano plot showing log2 fold-change differences versus –log (adjusted p-value) of GFP+ vs mCherry+ cells from Figure 13. B) Heatmap shows differentially expressed genes related to resistance to therapy, tumor initiation and hypoxia from samples in Figure 1A. Data are color coded to show gene expression Z-scores.

We next performed an unbiased pathway enrichment analysis of the transcriptome of GFP+ versus mCherry+ cells. The most significant gene ontology pathways that differed between GFP+ and mCherry+ cells were all related to cell cycle (Figure 19A, B). Key genes involved in proliferation and DNA replication, such as *Mki67* and *Pcna*, were all downregulated (Figure 19C, D).

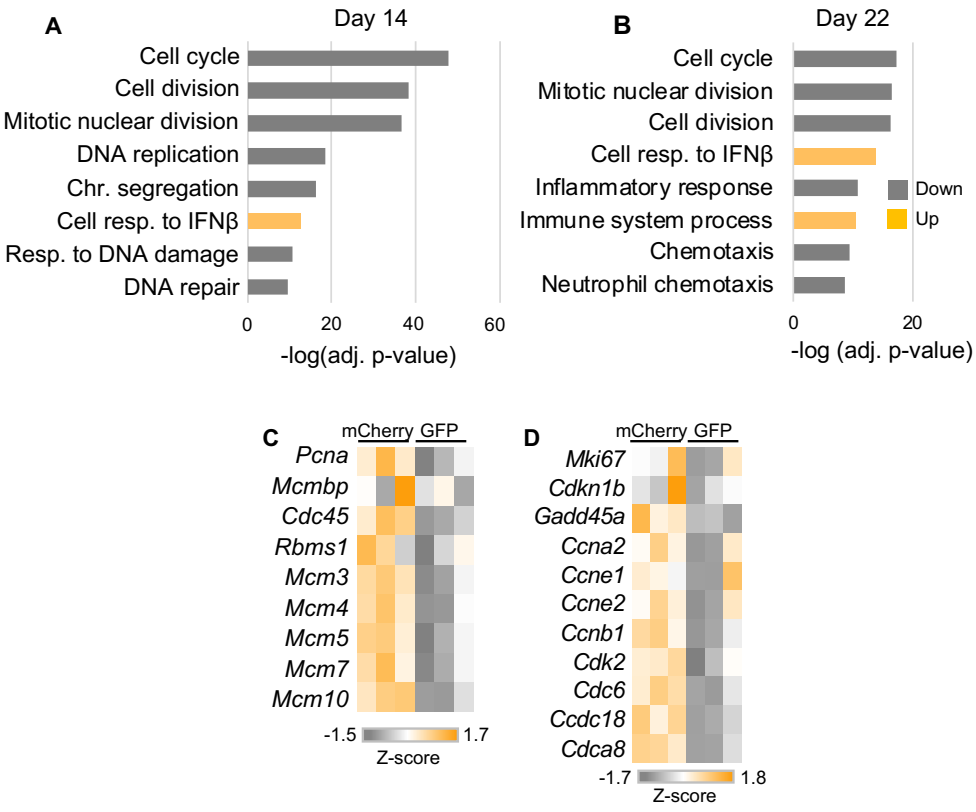

Figure 19. GFP+ resistant cells present cell cycle downregulation. Pathway enrichment analysis from differentially expressed genes in GFP+ versus mCherry+ cancer cells from RNA-seq from Figure 13 at day14(A) and 22 (B) (n=3-4 mice). Graph shows pathways ranked by lowest adjusted p-value. (C, D) Heatmaps show key differentially expressed genes in GFP+ vs mCherry+ cells involved in regulation of DNA replication (C) and cell cycle (D). Data are color coded to show gene expression Z-scores.

To confirm whether these resistant cells were in cell cycle arrest, we treated tumor-bearing mice with the thymidine analog 5-Ethynyl-2'-deoxyuridine (EdU) daily, starting before adoptive transfer of PD1-/- Jedi T cells. Six days post-Jedi treatment, most mCherry+ cancer cells were positive for EdU. Conversely, EdU signal was low in T cell-resistant GFP+ tumor cells. This demonstrated that most T cell resistant GFP+ cancer cells were not cycling prior to adoptive T cell transfer and did not cycle during T cell killing (Figure 20A, B). Therefore, cancer cells that escaped attack by CD8+ T cells formed distinct clusters of QCCs.

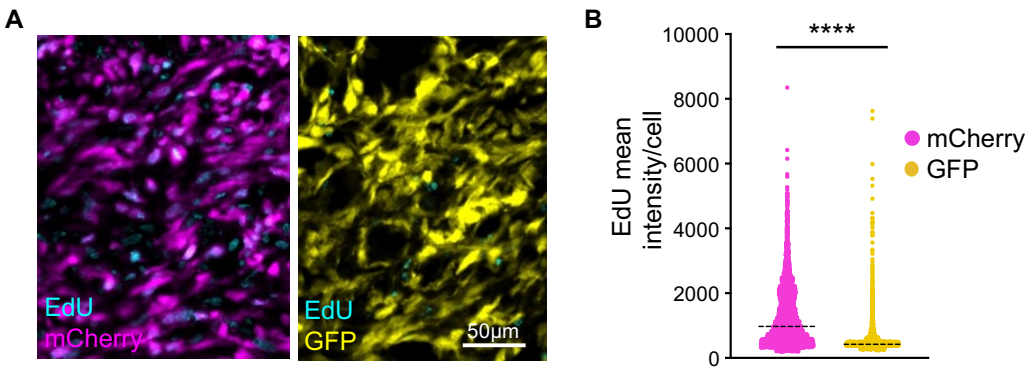

Figure 20. GFP+ resistant cells were quiescent before Jedi PD1-/- T cell adoptive transfer. J) EdU labelling in tumors from 2A. EdU was injected 30h before adoptive transfer of Jedi PD1-/- T cells and continued daily (n=5 mice). (K) EdU intensity for every cell from pictures in J. Line marks the median (n=15 images from 5 tumors). ****P<0.0001.

3.3. QCCs are more resistant to direct attack from cytotoxic T cells.

To understand QCC resistance to T cell killing, we set up an approach to isolate and profile live non-cycling cancer cells. We used a published quiescence reporter (131), consisting of mVenus fused to an inactive p27-CDK binding domain (mVenus-p27K). We validated this mVenus-p27K reporter in 4T07 tumors and observed that all mVenus-p27K^{High} cells were negative for Ki67 (Figure 21A, B). mVenus-p27K^{High} cells also remained EdU-negative after 5 days of EdU treatment (Figure 21C, D). These findings are consistent with previous studies reporting the existence of p27+ quiescent tumor cells in primary breast cancer (93). mVenus-p27K^{High} cells were also observed in 4T07 tumors in immune-deficient NSG mice (Figure 22), demonstrating that these QCCs arise independently of T cells.

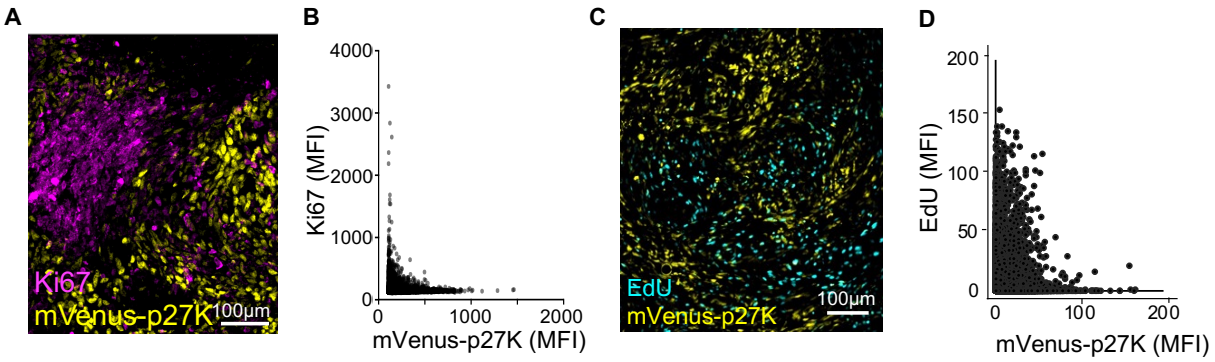

Figure 21. Validation of mVenus-p27K reporter in 4T07 naïve tumors. A, B) Analysis of Ki67 and mVenus-p27K reporter expression. A) Representative picture B) Graph depicts the intensity of the fluorescence signal for each marker in each cell from A. C, D) EdU was injected daily from day 10 to day 15 when tumors were harvested. Analysis of EdU and mVenus-p27K reporter expression was performed by immunofluorescence. C) Representative picture D) Graph depicts the intensity of the fluorescence signal for each marker in each cell from C.

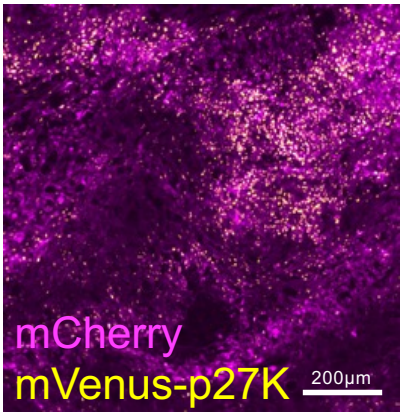

Figure 22. Quiescent mVenus-p27K tumor cells are formed in immunodeficient mice. Double transduced mCherry and mVenus-p27K-expressing 4T07 cells were injected in the mammary fat pad of NSG mice. Image shows a representative area of tumors at day 10 (n=3 mice).

Next, we replaced mVenus with the red protein tdTomato to prevent spectral overlap with GFP, and then engineered 4T07 cells to express either GFP as antigen or miRFP670 (far red) as a non-immunogenic control label. Mice with tumors that were mix of GFP:miRFP670 cells and carrying the tdTomato-p27K reporter received adoptive transfer

of PD1-/- Jedi T cells. Surviving GFP+ cells had a 2-fold increase in tdTomato^{High} cells compared to miRFP670+ cells (Figure 23A, B, C). We repeated this experiment using a higher number of PD1-/- Jedi T cells to enable more stringent killing (Figure 23A). In this setting, the few resistant GFP+ cells were almost all quiescent (Figure 23B, C). Taken together, this suggests that intra-tumor QCCs are more resistant to T cell killing than actively cycling cancer cells.

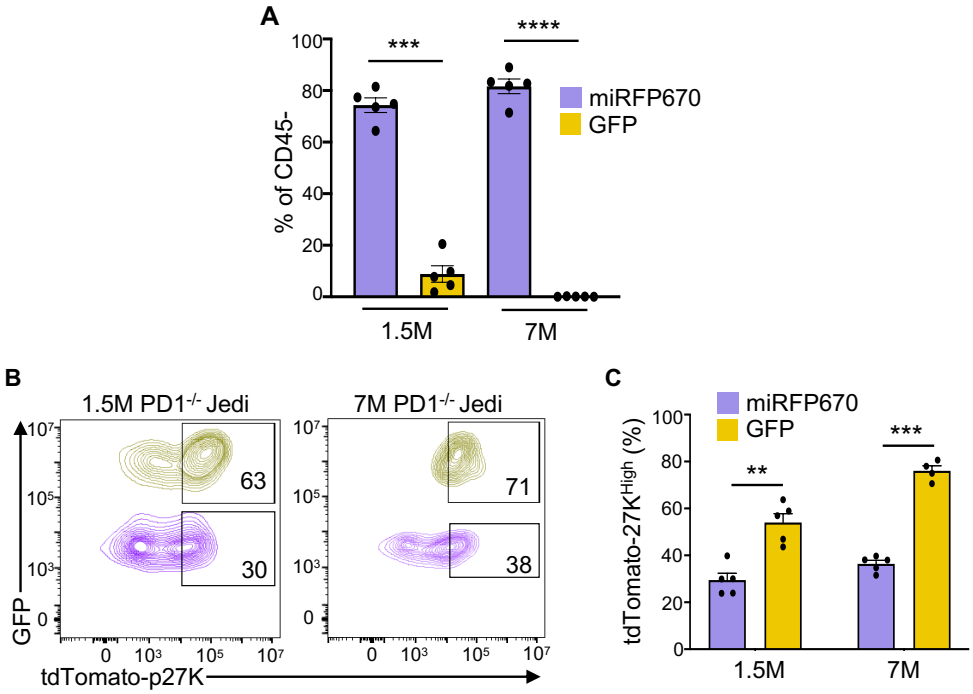

Figure 23. GFP+ resistant cells are marked by the tdTomato-p27K+ reporter. GFP and tdTomato-p27K 4T07 cells mixed with H2B-miRFP670 and tdTomato-p27k 4T07 and injected into animals. Tumor-bearing mice were treated with the specified number of PD1-/- Jedi T cells (n=5 mice). A) Flow cytometry analysis of GFP+ and H2B-miRFP670+ live tumor cells. Graph shows mean±sem of the percentage of total live per color amongst DAPI- CD45-. (B) Representative flow cytometry plots gating on GFP+ and miRFP670+ tumor cells from Dapi- CD45- gate. Percentages calculated over color coded populations. (C) Mean±sem of percentage of tdTomato^{High} cells from B. **P<0.01, ***P<0.001, ****P<0.0001.

Next, we assessed whether p27K^{High} cells were enriched upon T cell killing or, conversely, surviving GFP+ cells became quiescent during T cell attack. We built a genetic circuit

where Doxycycline induces H2B-tdTomato only in p27K+ cells (Figure 24A). p27K+ tumor cells were labeled by one Doxycycline injection. The next day, after drug clearance, Jedi T cells were adoptively transferred. Around 65% of the surviving GFP+ cells were tdTomato+ while only ~20% of the cells were tdTomato+ in tumors from NSG mice (with no T cell pressure) (Figure 24B). This indicates that many surviving GFP+ tumor cells after Jedi treatment were already p27K^{High} prior to adoptive transfer of Jedi cells.

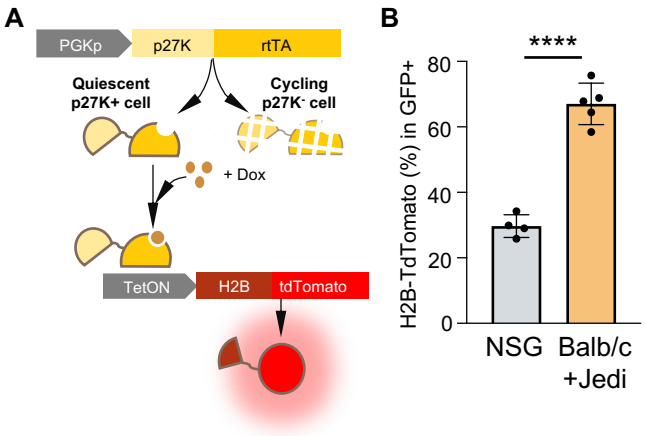

Figure 24. GFP+ resistant cells were p27K reporter+ before Jedi treatment. A, B) Genetic circuit to assess quiescence in cancer cells prior to injection of Jedi T cells. GFP+ 4T07 cells with the circuit were injected in BALB/c or NSG mice. All mice received doxycycline on day 6 post-tumor inoculation. 30h later, 5M Jedi T cells were injected into the BALB/c group. (A) Schematic. (B) Mean±sem of the percentage of H2B-tdTomato+ cells (n=4-5 mice). ****P<0.0001.

Since interferons can induce quiescence in disseminated tumor cells (98), and the top upregulated pathway in surviving GFP+ cells after T cell attack was “IFN-beta signaling” (Figure 19), we generated knockout cells for the IFNB receptor *Ifnar1* (Figure 25A). GFP+ Ifnar1-/- cancer cells were killed by Jedi T cells in a similar rate to their WT counterparts (Figure 25B). Among the surviving cells, there was also a similar ratio of p27K^{High} cells compared to WT GFP+ cells (Figure 25C), suggesting that IFNB was not critical for the quiescent phenotype observed in surviving cells.

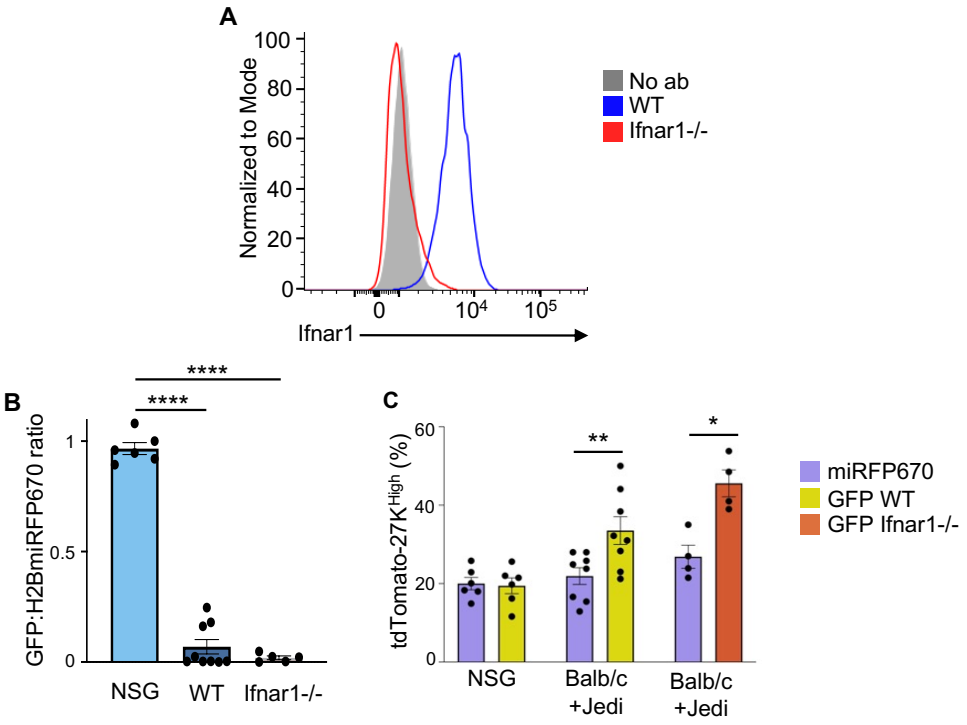

Figure 25. GFP+ resistant cells were tdTomato-p27K High in the absence of Ifnar1. A) Confirmation of loss of IFNAR1 protein in Ifnar1-/- cells B, C) Quantification of p27K^{High} cells in Jedi T cell-resistant cancer cells upon loss of IFNAR1 signaling. Either *Ifnar1-/-* or WT GFP 4T07 cells were mixed with WT H2B-miRFP670 4T07 cells (1:1) and were injected into BALB/c mice. WT GFP+ and H2B-miRFP670+ 4T07 cells were injected into NSG mice as no T cell controls. All cancer cells carried tdTomato-p27K reporter. 5M Jedi T cells were injected into all BALB/c mice. A) Graph shows quantification (mean±sem) of the GFP/H2B-miRFP670 ratio in the tumors. B) Mean±sem of percentage of tdTomato^{High} cells in each group is shown. *P<0.05, **P<0.01, ***P<0.001, ****P<0.0001.

3.4. QCCs possess greater cancer initiation potential.

Since QCCs did not proliferate for multiple days, we questioned whether these resistant cells could re-start a growth program after T cell therapy. We first tested the ability of surviving GFP+ cells to re-grow tumors compared to bulk GFP cells. Jedi T cell resistant GFP+ cells were able to re-grow tumors more efficiently than non-selected GFP+ tumor cells (Figure 26).

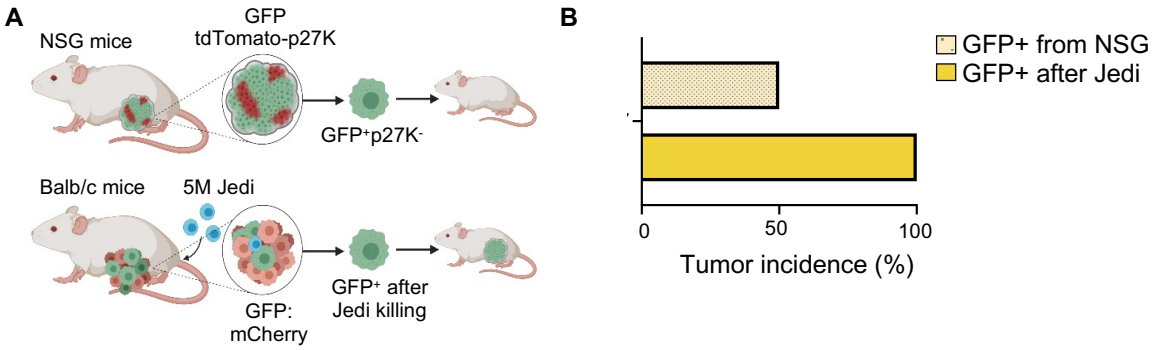

Figure 26. Assessment of tumor initiation potential in GFP+ cancer cells that survive T cell attack. GFP+ cells were isolated from 4T07 mammary carcinoma of either untreated NSG mice or from Jedi-treated BALB/c mice. 500 live sorted cells were injected in new mice. (A) Schematic of experiment. (B) Percentage of tumor growth (n=4).

We already observed the presence of p27K^{High} cells in naïve treated 4T07 tumors (Figure 21). We wanted to investigate if they would also have enhanced tumorigenic potential prior to therapy. First, in order to see if this was not cell line dependent, we investigated the existence of p27K^{High} QCCs in other models of TNBC: EMT6 and D2A1. We used the same experimental setting and treated tumors with EdU for the last 5 days, time in which tumors double in size (Figure 27A). In these models, mVenus-p27K^{High} cells also formed clusters and did not proliferate for several days (Figure 27B, C).

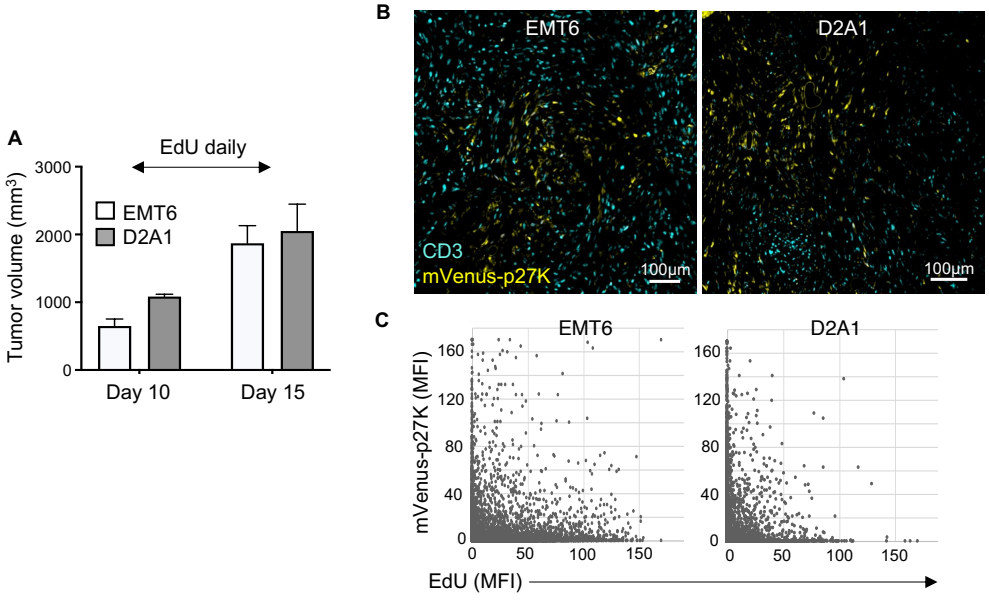

Figure 27. QCCs formation in other TNBC orthotopic models. A) Mice with mVenus-p27K- expressing EMT6 or D2A1 carcinoma were treated with EdU for the last 5 days prior harvesting tumors. Graph depict tumor volume at time of treatment initiation and harvest. B) Representative picture of immunofluorescence analysis after EdU staining. C) Graph depicts the intensity of the fluorescence signal for each marker in (B) in each cell.

Once the presence of QCCs in multiple TNBC models was confirmed, we addressed whether their quiescent state was terminal or if they were able to regrow tumor as p27K^{High} cells were able to do after Jedi treatment. We FACS-sorted live mCherry+ mVenus-p27K^{High} (QCCs) and mCherry+ mVenus-p27K^{Neg} proliferative counterparts from these models and injected them in new mice (Figure 28A). In all cases, mVenus-p27K^{High} cells re-grew tumors, proving they were not in a terminal state of quiescence. Remarkably, QCCs displayed a higher tumor initiation potential when injected at limiting numbers than mVenus-p27K^{Neg} cells (Figure 28B, C). Thus, QCCs were not only able to re-enter cell cycle and initiate tumor growth but did so more effectively than their proliferating counterparts.

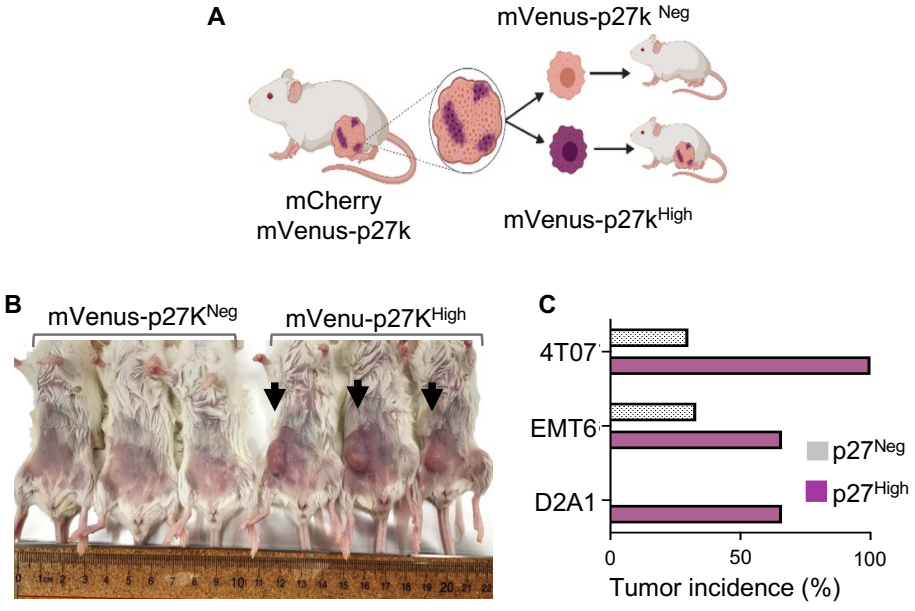

Figure 28. QCCs show higher tumorigenic potential than proliferative counterparts. A-C) Assessment of tumor initiation potential in QCCs. mCherry+ mVenus-p27K^{High} and mCherry+ mVenus-p27K^{Neg} cancer cells were isolated from 4T07, EMT6 and D2A1 tumors. Live sorted cells (500 for

EMT6 and 1000 for 4T07 and D2A1) were injected in new mice. (A) Schematic. (B) Representative picture. (C) Percentage of tumor growth (4T07 n=6; EMT6 n=3; D2A1 n=3).

3.5. Clusters of QCCs form a niche with limited immune infiltration.

We performed immuno-staining of CD3 in untreated mVenus-p27K-expressing 4T07, EMT6 and D2A1 tumors (Figure 29A). Although T cells were found inside clusters of QCCs, their numbers were always lower in these regions (Figure 29B).

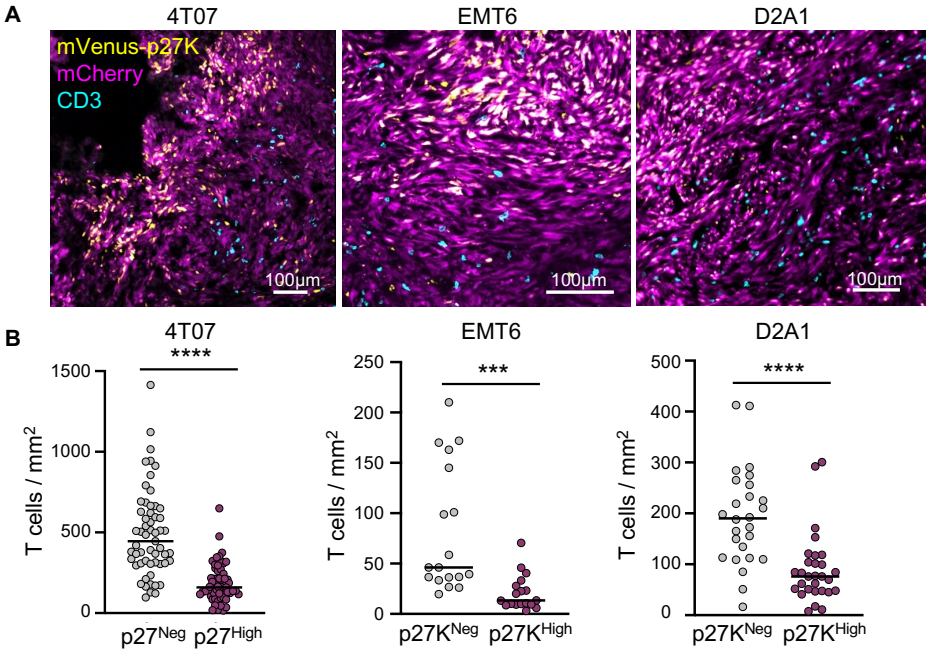

Figure 29. CD3+ cells are excluded from QCC areas. Immunofluorescence analysis of CD3+ cells in mCherry and mVenus-p27K-expressing 4T07, EMT6 and D2A1 mammary carcinomas (n=4 mice). (E) Quantification of T cell density in mVenus-p27K^{High} versus mVenus-p27K^{Neg} areas in 4T07 tumors (n=28 images from 3 mice. ***P<0.001, ****P<0.0001.

T cell exclusion in naïve treated tumors was a crucial finding that could help explain why GFP+ surviving cells originated from QCCs. Therefore, we wanted to further quantify the relationship between QCCs and T cells. To do so we generated tumors with H2B-mCherry

and mVenus-p27K reporter. The nuclear markers helped us with cell segmentation and allowed us to quantify the distance from every cancer cell to the closest T cell (Figure 30A). We then randomized QCC positions among H2B-mCherry+ cells and recalculate distance from QCC to the T cells. The real distance between mVenus-p27K^{High} and CD3+ cells was always larger than that obtained in the randomization, indicating that T cells were on average further from QCCs than from the rest of cancer cells (Figure 30B).

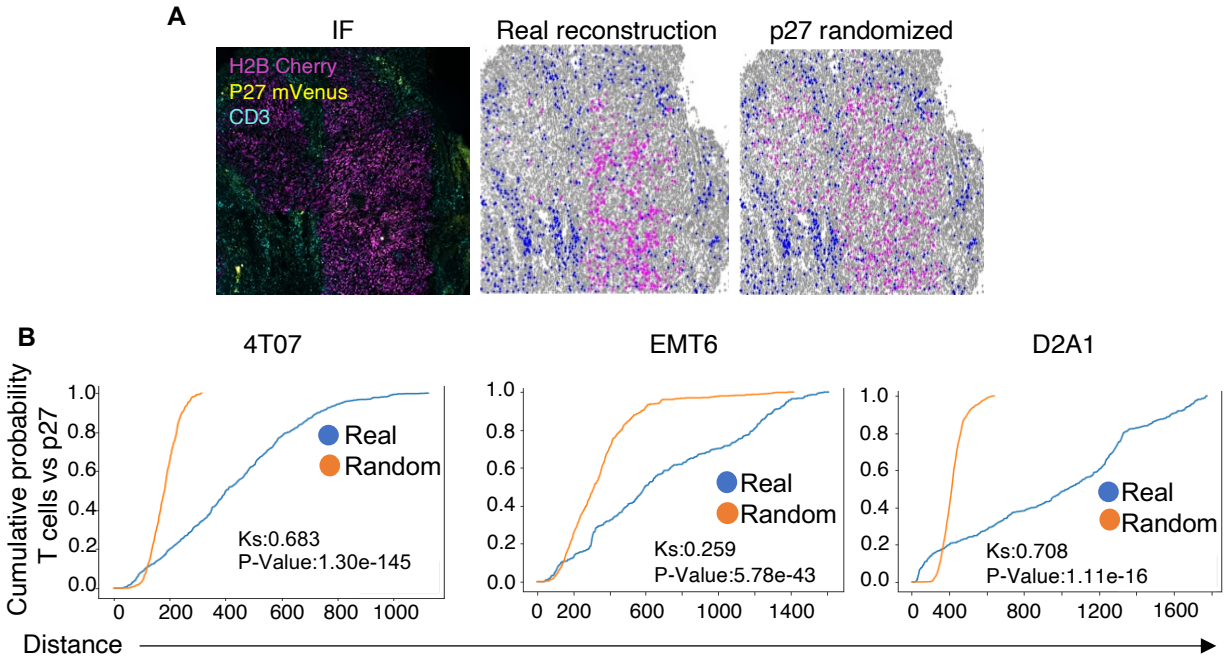

Figure 30. Computational analysis of T cell exclusion in QCC areas. A) H2B-mCherry tumors with mVenus-p27K reporter were grown into Balb/c mice. Panel show a representation of the computational analysis performed. For every tumor images were taken. Every picture was then segmented with Dapi, and cells were assigned to QCC, or T cell based on the intensity values for every channel. Then p27K^{High} cells were randomized among H2B-mCherry+ cells. B) Representative graph obtained with 1 tiled image for the evaluation of T cell exclusion with Kolmogorov-Smirnoff statistic using the real QCC population or a randomized QCC distribution among cancer cells (n=3 tumors with 3 sections analyzed per tumor).

Staining for CD4 and CD8 confirmed that both types of T cells were reduced inside the clusters of QCCs (Figure 31A, B). Further analysis with anti-CD45 staining revealed that

regions with QCCs had poor immune infiltration compared to cycling areas (Figure 31C). These results demonstrated that QCCs reside in a niche with reduced numbers of infiltrating immune cells.

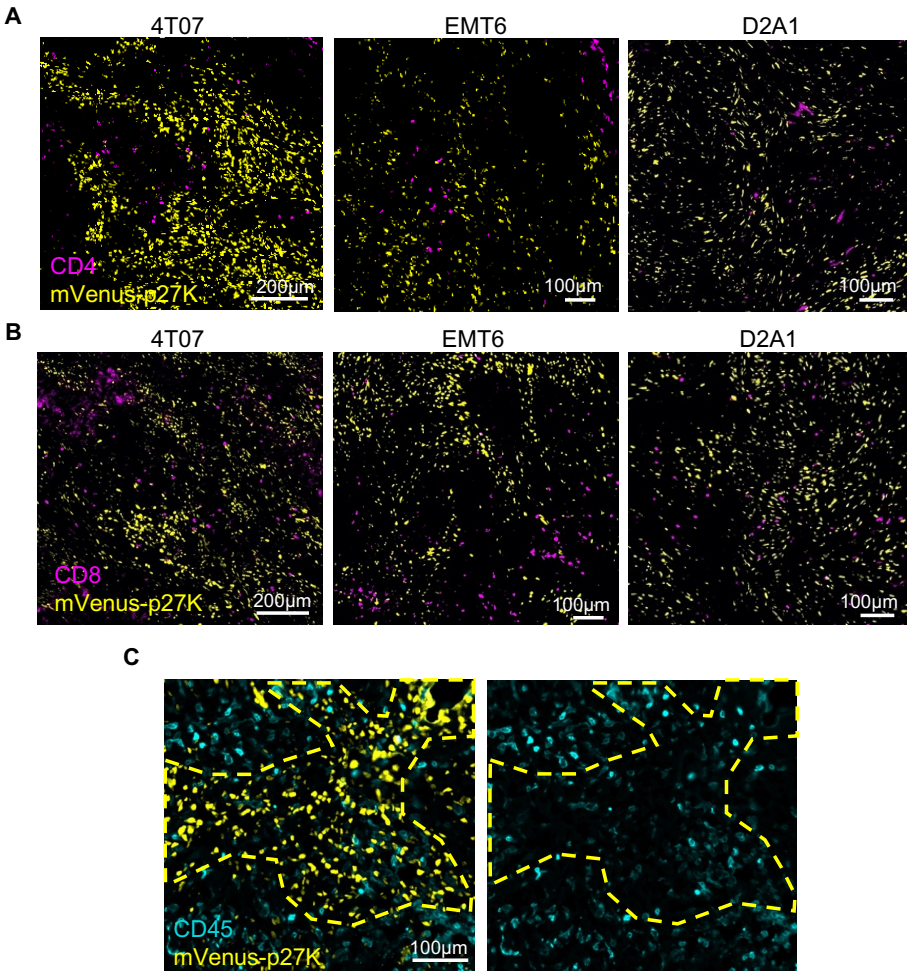

Figure 31. Immune exclusion on QCC areas. A, B) CD4 (A) and CD8 (B) representative immunofluorescence in mVenus-p27K-expressing 4T07 tumors (n=3 mice). (G) CD45 representative immunofluorescence in mVenus-p27K-expressing 4T07 tumors (n=5 mice).

3.6. Proliferation correlates with T cell infiltration in patients.

To dissect the relationship between QCCs and T cells in patients, we analyzed p27, Ki67, CD3 and E-cadherin on tumor tissue (Figure 32A). We measured the number of Ki67+

(proliferative) or p27+ (quiescent) tumor cells in contact with T cells in cancer biopsies from 10 de-identified treatment naive patients. This uncovered that Ki67+ cells were more frequently found in the vicinity of T cells than p27+ cancer cells (Figure 32B).

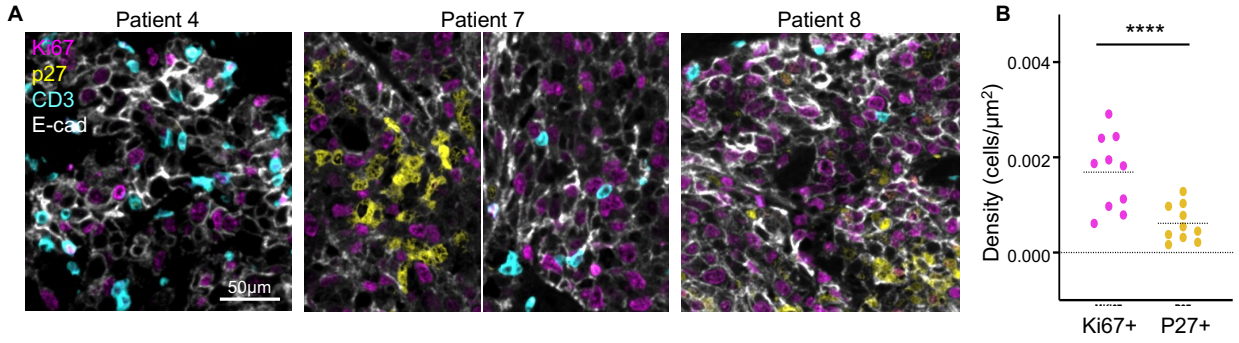

Figure 32. T cell infiltration in patients correlates with Ki67+ cancer cells. A) Immunofluorescence analysis of CD3, p27, Ki67 and E-cadherin (E-cad) in tissue sections from TNBC de-identified patients (n=10 patients). (I) Density of p27+ and Ki67+ tumor cells surrounding T cells. Each dot represents the averaged density of the corresponding marker (p27 or Ki67) in all analyzed areas from each patient in A.

Next, we investigated whether abundance of quiescent versus proliferative cells in human TNBC could influence the response to ICB. We utilized bulk RNA-seq datasets from pre-treatment biopsies in a cohort of 29 patients with metastatic TNBC that were treated with PD-1/PD-L1 inhibitors (Barroso-Sousa R, Forman J, Collie K, et al under revision). In this cohort, 5 patients presented with primary resistance to ICB; we defined them as non-responders. Among the 24 patients with benefit, 5 patients experienced a durable response (durable responders; progression-free survival ranging from 26-60 months) (Figure 33A). Gene set enrichment analysis (GSEA) of these data comparing durable responders and non-responders showed “Reactome E2F regulation of DNA replication” as the number one most enriched pathway (Figure 33B), suggesting that tumor proliferation may correlate with response to ICB. This result agreed with recent reports comparing chemotherapy+ICB to chemotherapy alone. RNA-seq analysis of >800 patients in a multi-center clinical trial revealed “Cell proliferation” as a top pathway enriched in responders in the ICB arm (65). Although it is only an association, these data

suggest that TNBC with abundant proliferative tumor cells could have a better response to ICB, while QCCs could lead to resistance.

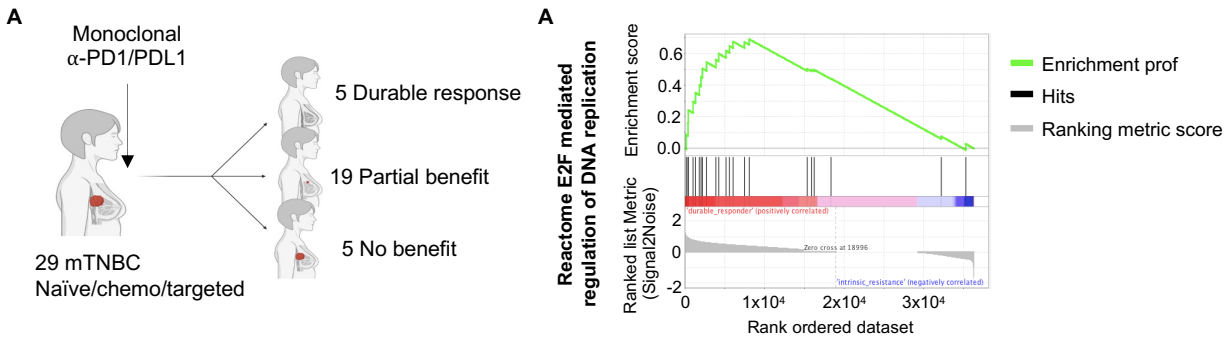

Figure 33. Durable response of immunotherapy in patients is correlated with cell proliferation by bulk RNAseq. A) Patient cohort treated with ICB at DFCI (n=29 patients). B) Most significantly upregulated transcriptional program in durable responders compared to non-responders in A by bulk RNAseq from tumor pre-treatment biopsies.

3.7. QCCs express genes related to chemoresistance, hypoxia, and glycolysis.

To investigate mechanisms of resistance in QCCs, we FACS-sorted live QCCs (mVenus-p27K^{High}) and non-quiescent (mVenus-p27K^{Neg}) tumor cells from 4T07, EMT6 and D2A1 tumors for RNA-seq. Unbiased Gene Ontology (GO) analysis from differentially expressed genes (Figure 34,) showed that the most downregulated genes in QCCs were involved in cell cycle, confirming their quiescent nature (Figure 35).

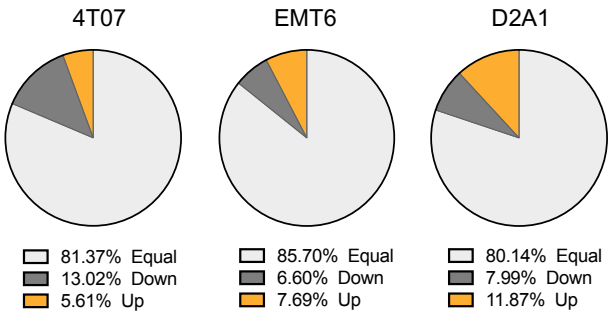

Figure 34. Overview of differentially expressed genes in three orthotopic mouse models between QCC and proliferative cancer cells. RNAseq analysis of mCherry+ mVenus-p27K^{High} and mCherry+ mVenus-p27K^{Neg} cells from 4T07, EMT6 and D2A1 tumors. Pie charts show the percentage of differentially expressed genes by bulk RNAseq in cells from Figure 29 (4T07 n=4; EMT6 and D2A1 n=3, respectively).

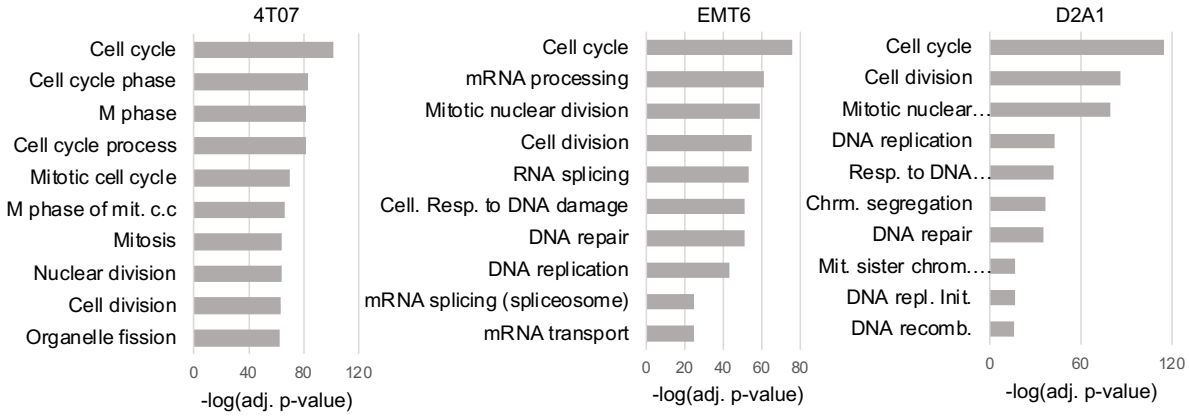

Figure 35. Gene Ontology analysis from downregulated genes in QCC ranked by significance. Pathway enrichment analysis of RNA-seq from Figure 34 showing top downregulated pathways ranked by adjusted p-value.

Amongst the most upregulated genes in QCCs, we identified genes linked to chemo-resistance: *Car9* (132), *Kdm5a*, *Kdm5b* (133); and related to stemness: *Runx1*, *Klf4*, *Sox4*, *Sox9* (134) (135) (Figure 36).

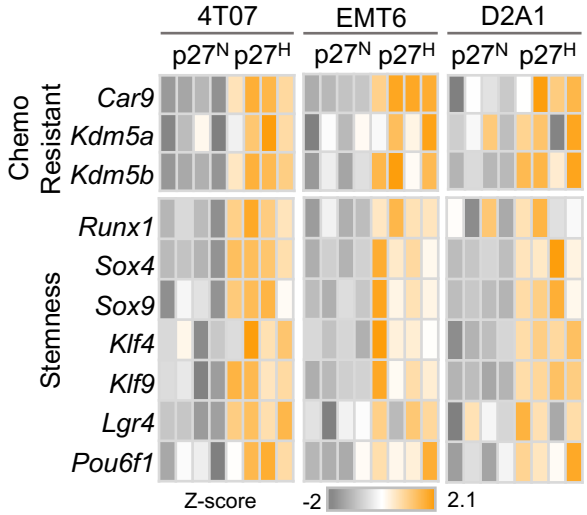

Figure 36. QCC upregulate genes related with stemness and chemoresistance. RNAseq analysis of mCherry+ mVenus-p27K^{High} and mCherry+ mVenus-p27K^{Neg} cells from 4T07, EMT6 and D2A1 tumors. Heatmaps show differentially expressed genes involved in stemness and chemotherapy-resistance.

Unbiased GO term analysis of upregulated genes showed that the top upregulated pathways in QCCs across the 3 models were hypoxia and hypoxia-related (eg. angiogenesis) and glycolysis and glucose metabolism-related (Figure 37).

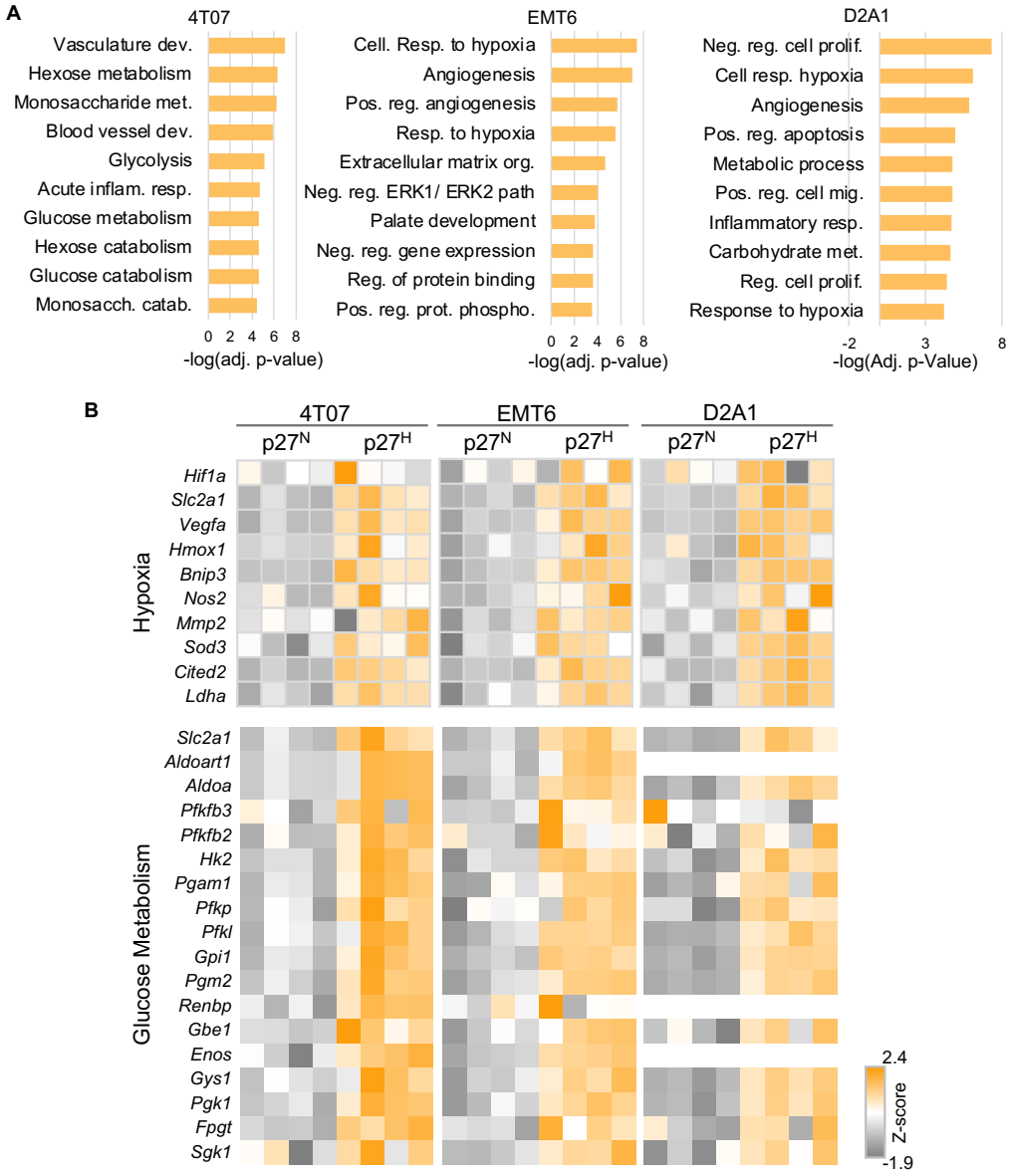

Figure 37. Gene ontology analysis of upregulated genes in QCC. RNAseq analysis of mCherry+ mVenus-p27K^{High} and mCherry+ mVenus-p27K^{Neg} cells from 4T07, EMT6 and D2A1 tumors. (n=4). A) Pathway enrichment analysis showing top upregulated pathways by adjusted p-value. (B) Heatmap shows hypoxia-induced and glucose metabolism differentially expressed genes in A. Data is color coded to reflect gene expression Z-scores.

To test whether these QCCs were indeed in a hypoxic niche, we visualized pimonidazole (Hypoxyprobe®) along with CD3 in mVenus-p27K-expressing tumors. Pimonidazole+ regions partially co-localized with clusters of QCCs and inversely correlated with T-cell rich regions (Figure 38).

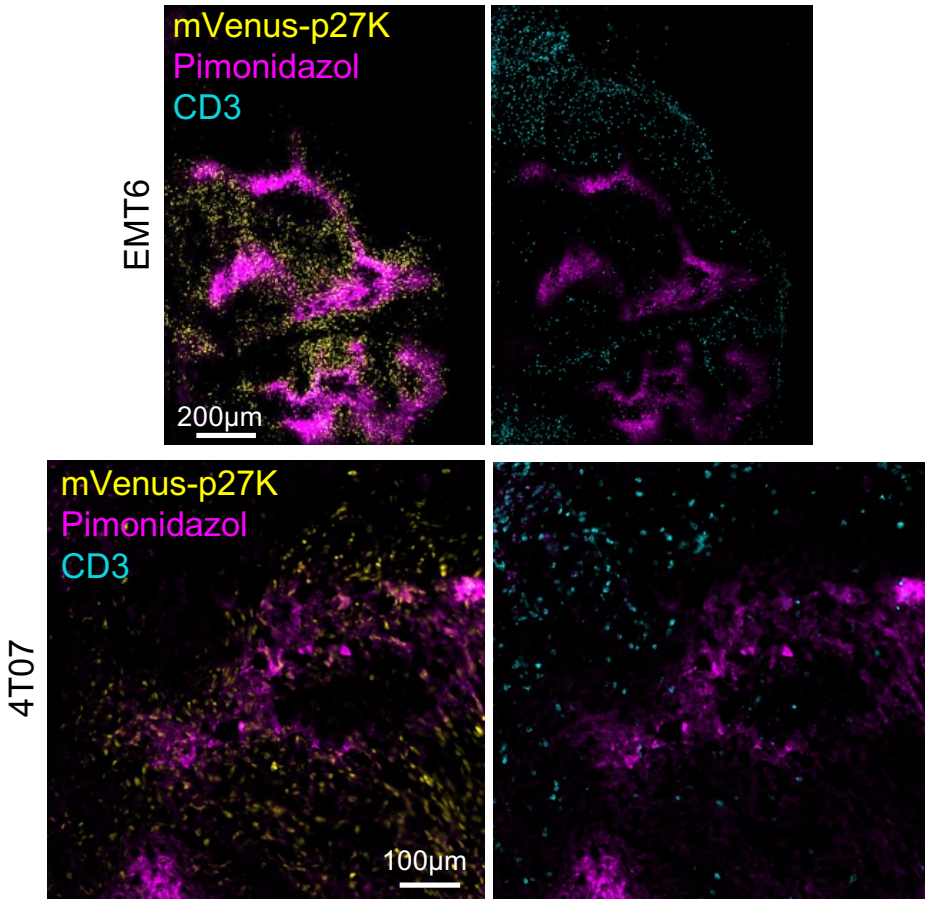

Figure 38. Immunofluorescence evaluation of hypoxic areas with Pimonidazol staining shows correlation with QCC and anticorrelation with T cells. Pimonidazole was injected to EMT6 and 4T07 tumor bearing animals 30min prior euthanasia. Representative immunofluorescence shown for Pimonidazol (magenta) and CD3 (cyan). (n=3 mice/model).

Accordingly, areas of surviving GFP+ cancer cells after Jedi T cell attack also showed augmented pimonidazole signal (Figure 39). This suggested that the HIF1Aα signature observed in the RNA-seq data was the result of local hypoxia.

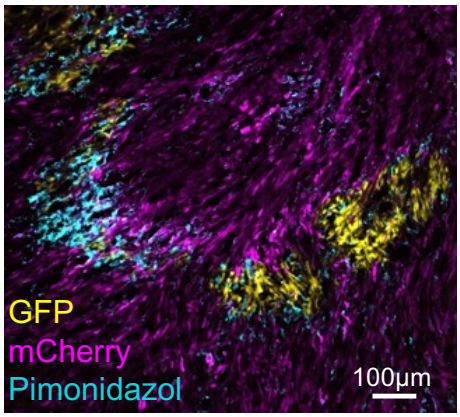

Figure 39. Immunofluorescence evaluation of hypoxic areas in GFP:mCherry mixed tumors treated with Jedi T cells. Pimonidazole in GFP:mCherry 4T07 tumors 7 days after treatment with 5M Jedi T cells (n=5 mice).

HIF1A activation leads to expression of glycolytic genes such as the glucose transporter *Slc2a1* or *Glut1*. QCCs showed a >2-fold increase in uptake of 2-NBDG, demonstrating that these cells were more glycolytic than their proliferative counterparts, a feature that had been described in tumor initiating cells (135) (136) (100) (Figure 40). Hence, QCCs in breast cancer reside in hypoxic micro-niches and display an enhanced glycolytic phenotype as reported by others (93) (137).

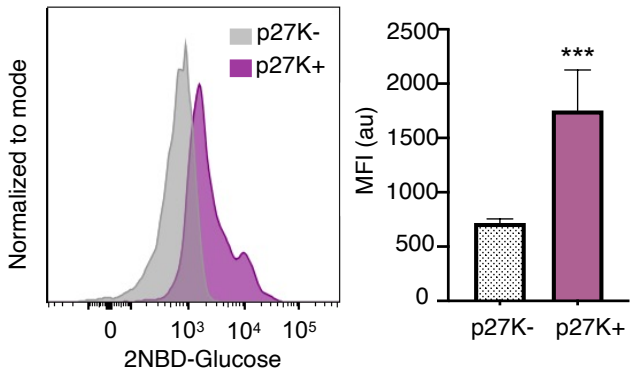

Figure 40. Glucose uptake evaluation in QCC vs proliferative cells from 4T07 tumors. Tumors were processed to obtain single cell suspension and exposed to 2-NBDG-glucose. Glucose uptake was evaluated by flow cytometry in tdTomato-p27K High cells vs tdTomato-p27K Negative cells. Mean±sem of Mean Fluorescent Intensity (MFI) of 2-NBD-Glucose (n=3 mice). ***P<0.001.

3.8. The QCC niche displays suppressive fibroblasts and more exhausted T cells.

To uncover how QCCs limited T cell function at single-cell resolution, we adapted a protocol for isolation of cells from specific tissue areas for scRNA-seq (86) to our tumor setting. We used transgenic mice expressing the photo-convertible protein Kaede to grow tdTomato-p27K-expressing tumors and generated consecutive slices of live tumor (Figure 41). This approach, which we named Photo-conversion of Areas to Dissect Micro-Environments (PADME-seq), allowed us to profile infiltrating cells from distinct sub-regions within the same tumor mass (inside and outside clusters of QCCs).

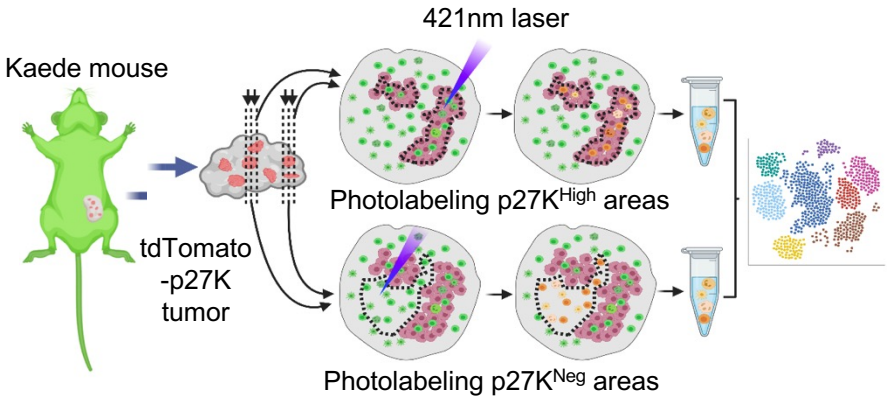

Figure 41. PADME-seq schematic. Tumors transduced with tdTomato-p27K reporter were injected into Kaede mice. Live consecutive sections were used to photoconvert infiltrated from p27K High areas or p27K negative areas. Photoconverted cells were flow sorted and submitted for 10X scRNAseq.

In every tumor slice QCC or non-QCC locations were defined based on tdTomato-p27K expression (Figure 42A). QCC areas were assigned in one slice and non-QCC in the adjacent slice. Photoconversion allowed for distinction of the marked areas both in the microscope (Figure 42 B, C) and by flow cytometry (Figure 43).

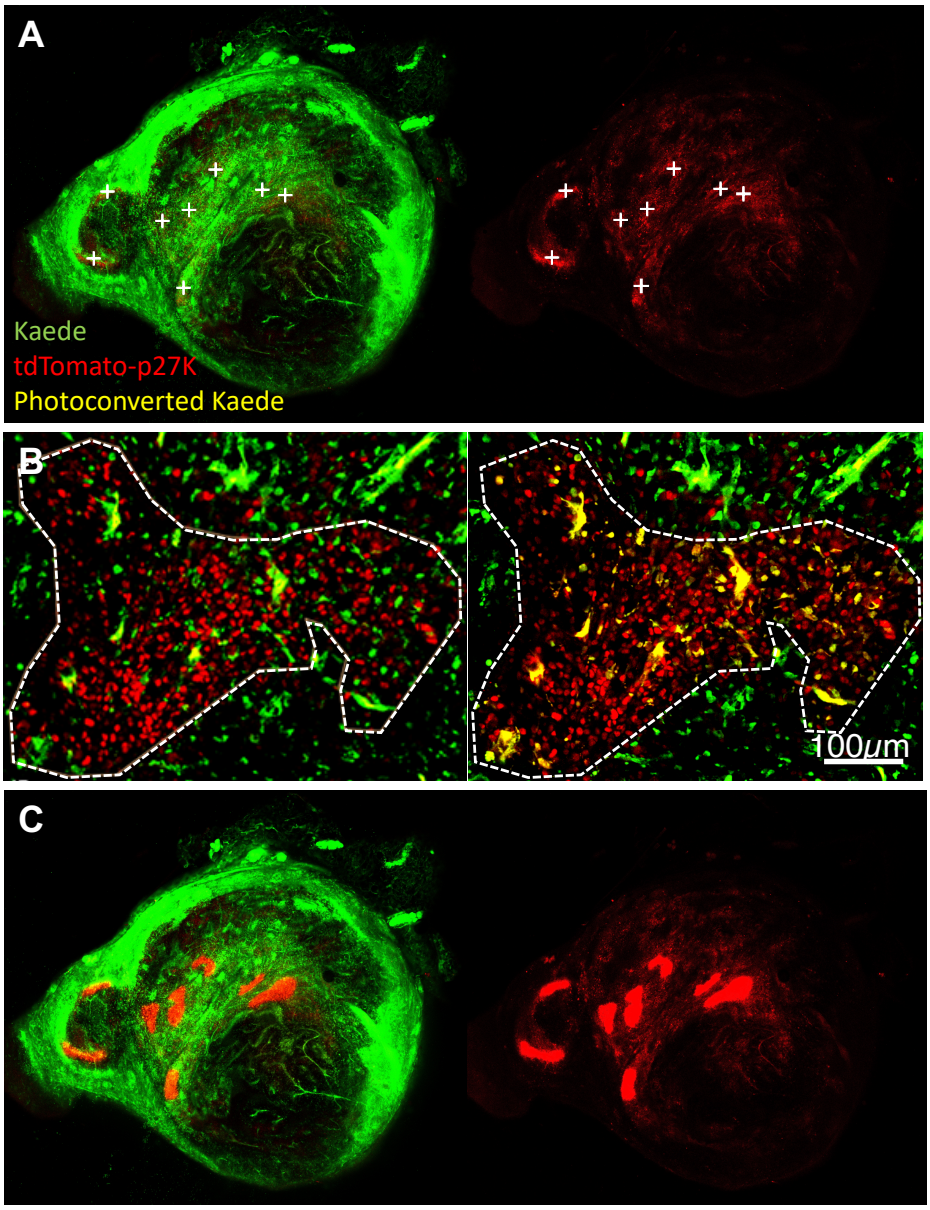

Figure 42. Photoconversion of Kaede protein in tumor slices. A) Full-size image of the tumor slice showing the distribution of the expression of the non-photoconverted Kaede protein in host cells (green channel) and the expression of the quiescence reporter in specific tumor cells (red channel). The data from the red channel was used to select positions of interest (white crosses) based on the tdTomato-p27k reporter (red). B) Region of interest drawn based on tdTomato-p27k reporter expression (white dash-dotted line) before and after photoconversion (left and right, respectively). Overlay of green and red channels is shown. C) Full-size image of the tumor slice acquired after photoconversion to corroborate successful photoconversion in all selected positions.

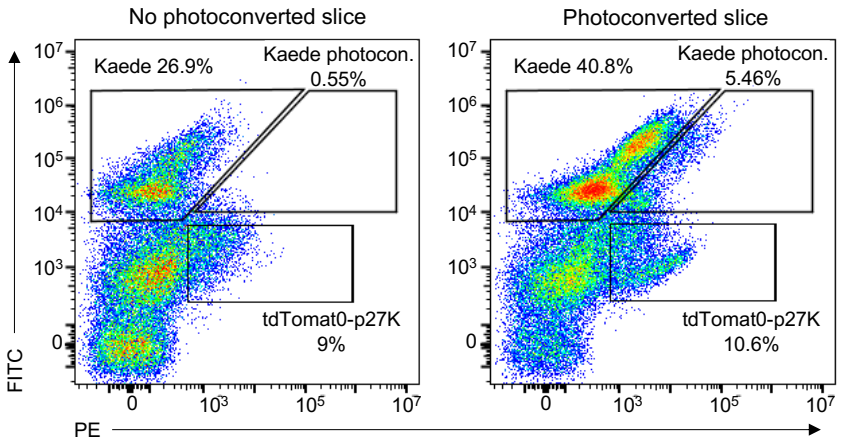

Figure 43. Flow cytometry visualization of Kaede photoconversion in tumor slice. Representative flow cytometry of digested tumor slice gated in Dapi- with and without photoconversion.

We performed two separate experiments in which we FACS-sorted equivalent numbers of live photo-converted cells from each region. After discarding doublets and cells with low mRNA quality, we had 1,743 and 975 cells from inside the areas of QCCs for each experiment respectively, and 1,968 and 2,259 in non-QCC regions. All major tumor infiltrating cell types (macrophages, fibroblasts, T cells, dendritic cells, NK cells, and neutrophils) were present both inside and outside regions of QCCs (Figure 44, 45, 46).

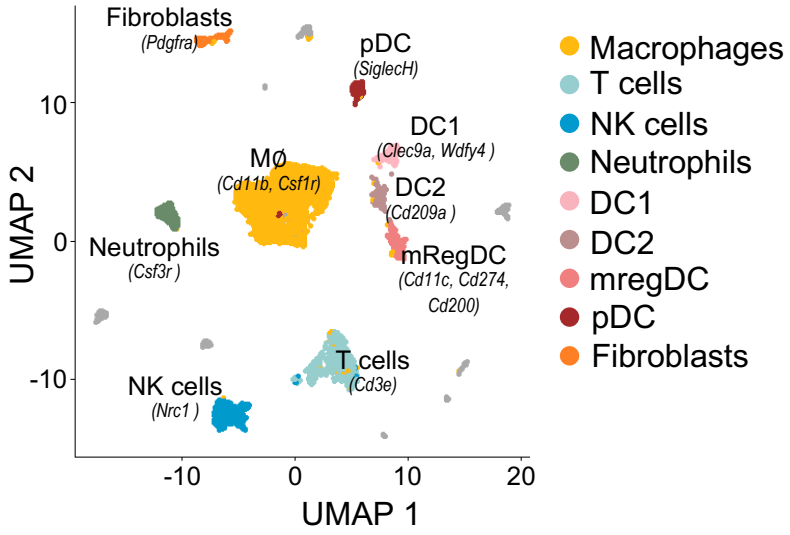

Figure 44. UMAP representation of populations from PADME-seq. We performed PADME-seq

from 2 independent tumors and for each tumor we pooled 2 slices from each tumor p27KHigh and p27K negative areas. Populations were called based on specific markers for each population.

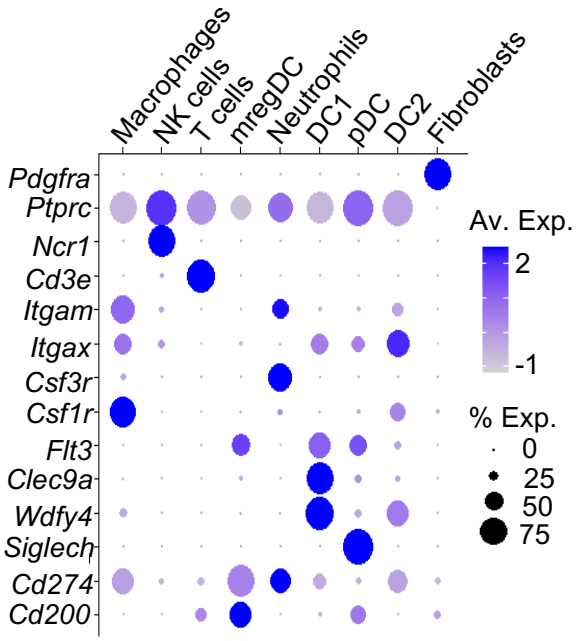

Figure 45. Expression of markers used to call populations from PADME-seq. Plot shows expression levels and percentage of cells expressing each marker for the genes used to call populations in UMAP from figure 44.

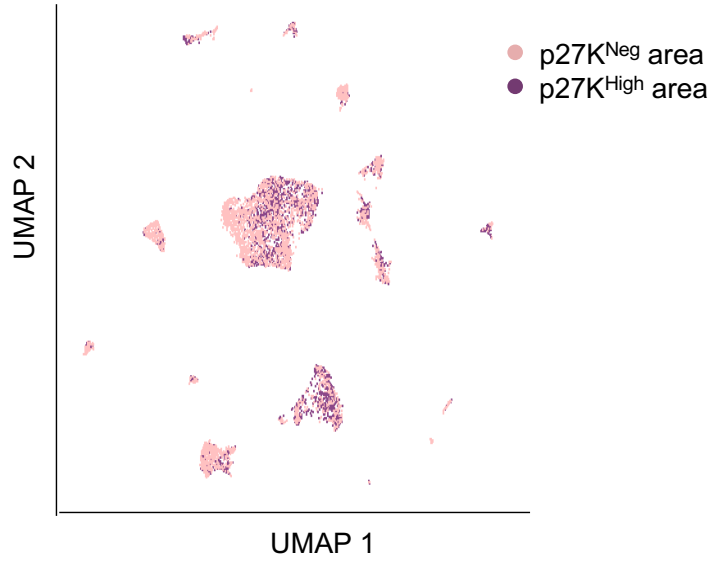

Figure 46. Distribution of cells from each area across the different populations. UMAP visualization from figure 44 highlighting cells based on the area of origin.

Since immunofluorescence analysis had shown that immune infiltrates (Figure 31C) were reduced in QCC regions, we first investigated whether fibroblasts were phenotypically different. Unsupervised GSEA comparing fibroblasts from p27K^{High} versus p27K^{Neg} areas revealed that immune-related defense pathways were downregulated in the QCC niche (Figure 47A). Conversely, collagen-deposition pathways were upregulated (Figure 47A, B). Notably, we compared our data with a previously published fibroblast signature identified in ICB-resistant patients (32) and confirmed a suppressive fibroblast phenotype inside the QCC niche (Figure 47C).

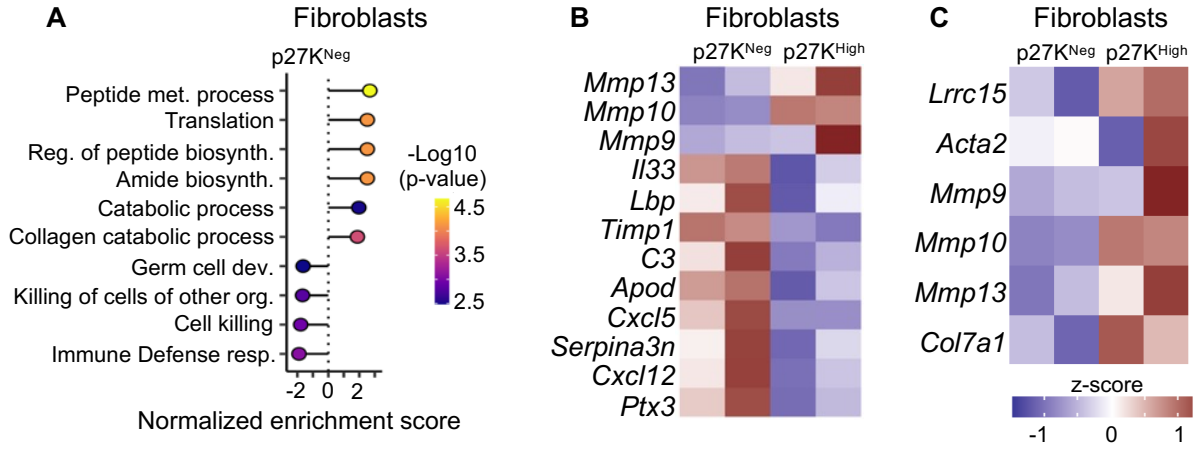

Figure 47. Collagen deposition and immunosuppressive fibroblast signature. A) Unsupervised gene-set enrichment analysis performed in the fibroblast population comparing cells from p27K^{High} vs p27K^{Neg} areas. B) Heatmap with the average expression across populations in set signature genes from A. C) Heatmap shows key differentially expressed genes depicted from Dominguez, et al. 2020 (32) as an immunosuppressive signature. Z-score normalized data are shown.

Although immune infiltration was lower in areas of QCCs, some T cells were able to enter. To understand why these T cells could not kill QCCs, we analyzed gene expression profiles of T cells inside and outside QCC areas. First, to elucidate the heterogeneity in T cell subsets, we reclustered the *Cd3+* T cell cluster (Figure 48, 49). This revealed one subset of γδT cells, one of CD4+ T cells and five of CD8+ T cells. One CD8+ T cell subset

displayed high expression of myeloid-specific genes such as Lyz2 and was not included in further analysis (Figure 49).

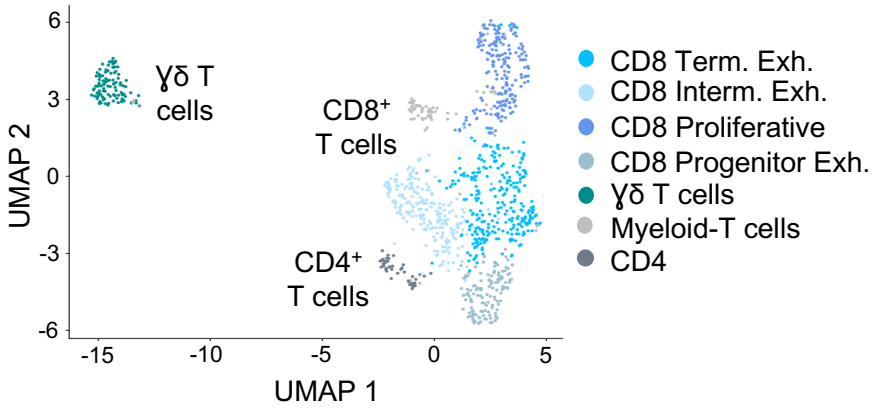

Figure 48. UMAP visualization of T cell reclustering. CD3+ cells from Figure 44 were reclustered. Populations were called based on top differentially expressed genes shown in figure 39.

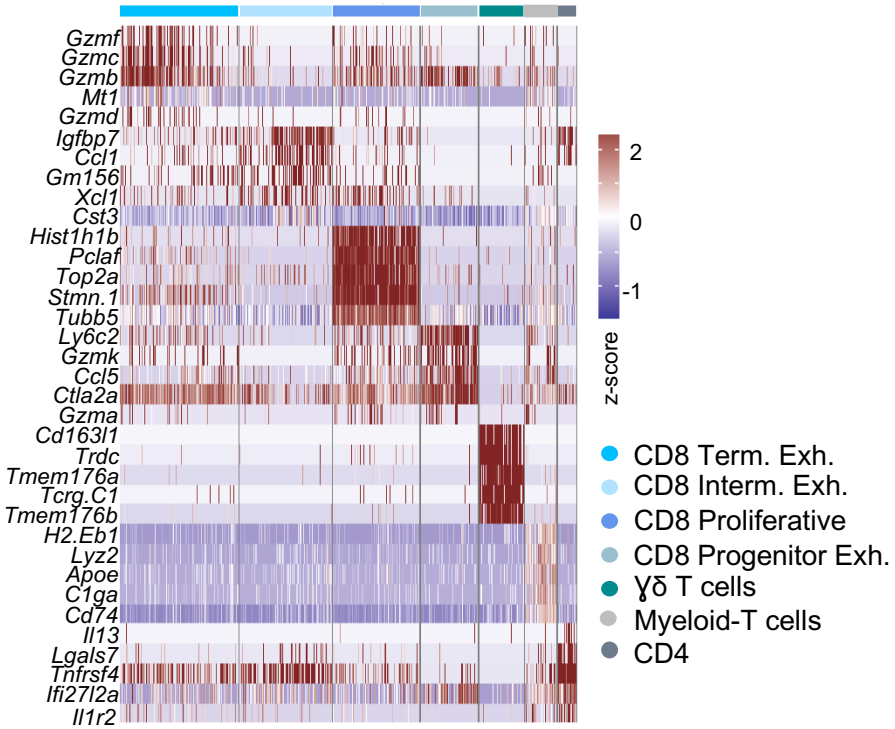

Figure 49. Top differentially expressed genes in T cell reclusterization. Heatmap shows genes driving the T cell reclusterization. Data is color coded to reflect gene expression Z-scores.

We performed GSEA of the remaining CD8+ subsets comparing cells inside p27K^{High} regions with cells outside. This revealed downregulation of multiple immune functions and signaling pathways in CD8+ T cells inside the QCC niche (Figure 50A). Additionally, we constructed a co-expression network, which showed downregulation of genes related to T cell activation in CD8+ T cells inside QCC areas (Figure 50B, C). Taken together, these analyses suggest that CD8+ T cells in the QCC niche are more dysfunctional and less fit for anti-tumor immunity.

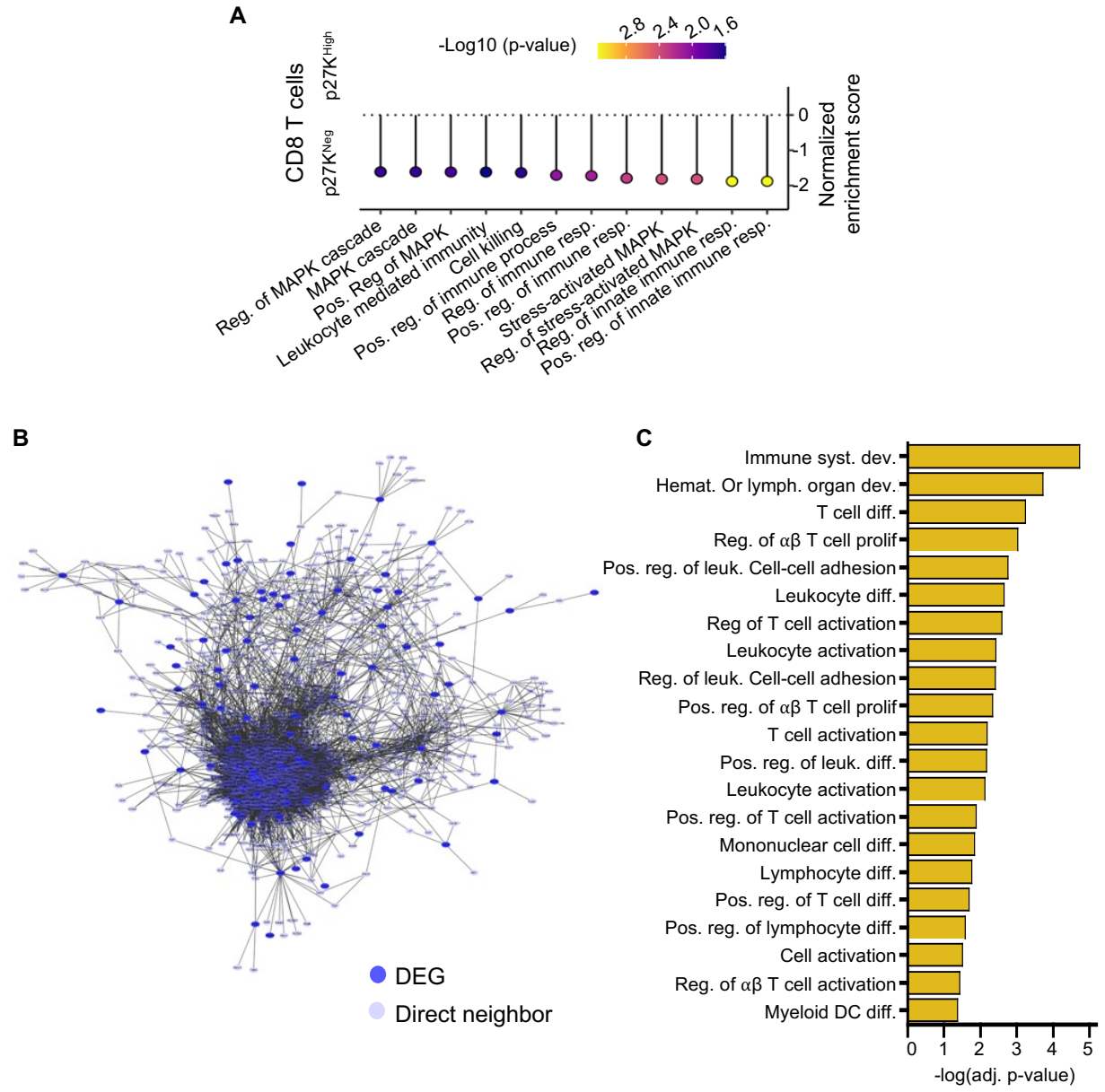

Figure 50. CD8 fitness analysis in QCC areas. A) Unsupervised gene-set enrichment analysis

performed in all CD8 T cells comparing $p27^{High}$ vs $p27^{Neg}$ areas. B) Co-expression gene network in CD8+ T cells visualized by Cytoscape (ver 3.7.1). The largest connected-component with only the DEGs and their direct neighbors are shown here. C) Pathway enrichment analysis from direct neighbors only from B. Graph shows only the T cell related-pathways ranked by lowest adjusted p-value.

Further, we classified the 4 identified sub-populations of CD8+ T cells using previous literature (18) (21) as: Terminally exhausted (*Prf1*, *Havcr2*, *Gzmb*, *Il2rb*), Intermediate exhausted (*Tnfrsf4*, *Lag3*, *Ifng*, *Ccl3*, *Tnfrsf9*, *Csf1*), Proliferative (*mKi67*, *Cdk1*), and Progenitor exhausted (*Cd28*, *Cxcr3*, *Ifit1*, *Stat1*) (Figure 48, 51).

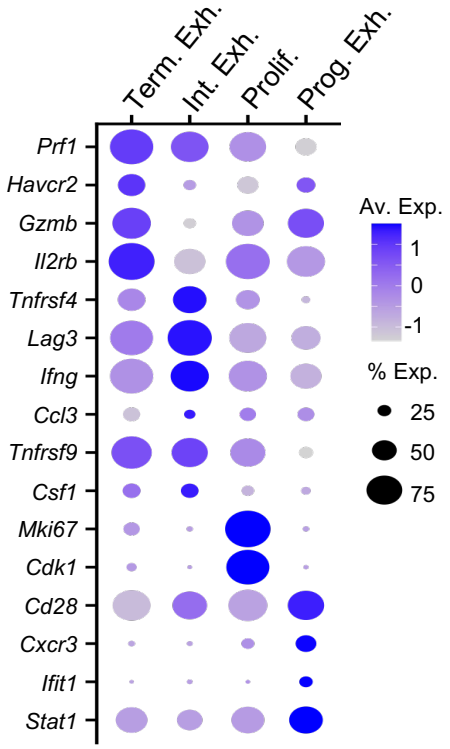

Figure 51. Expression of exhaustion state markers across the CD8 populations. Graph shows expression levels and percentage of expression in every CD8 cluster from figure 48. Depicted genes were used for identification of CD8 T cell populations from (Beltra et al., 2020 (21); Miller et al., 2019 (18)).

The percentage of Terminally exhausted CD8+ T cells was higher inside the QCC niche, whereas Proliferative CD8+ T cells were more frequent outside the QCC niche (Figure 52). Terminally exhausted T cells displayed the highest expression of *Havcr2* (TIM3+) a hallmark of the most dysfunctional T cells inside QCC areas (data not shown) (138) (139).

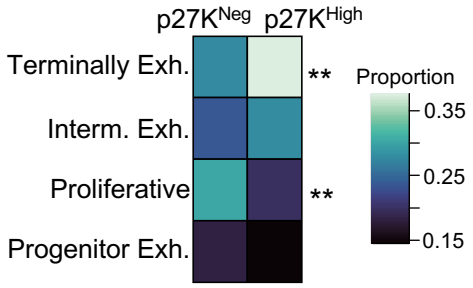

Figure 52. CD8 T cell states composition in QCC and proliferative areas. Distribution of CD8+ T cell sub-populations identified in F. **adj. p-value<0.01.

Thus, to validate this T cell exhaustion signature inside the QCC niche, we quantified PD1+ TIM3+ CD8+ T cells by flow cytometry using the same photo-labeling system (Figure 53).

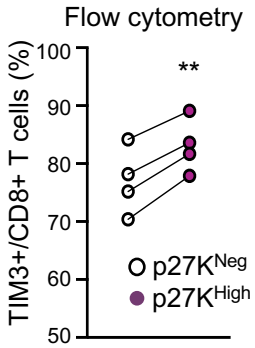

Figure 53. T cell exhaustion analysis in QCC areas by flow cytometry after PADME. Flow cytometry analysis of infiltrating cells in tdTomato-p27K^{High} areas versus tdTomato-p27K$^{Neg.}$ Graph show percentage of Tim3+ CD8+ T cells in each photoconverted area. (n=4 mice).

Additionally, we used CODEX (Akoya®) for multiplexed immunofluorescence to quantify exhausted T cells with respect to p27+ cells (Figure 54A, B, C). Both approaches

confirmed that less exhausted TIM3- CD8+ T cells were more abundant in proliferative tumor areas (Figure 53, 54). CODEX analysis also confirmed a significant reduction in overall immune infiltration inside the QCC nice (Figure 54D).

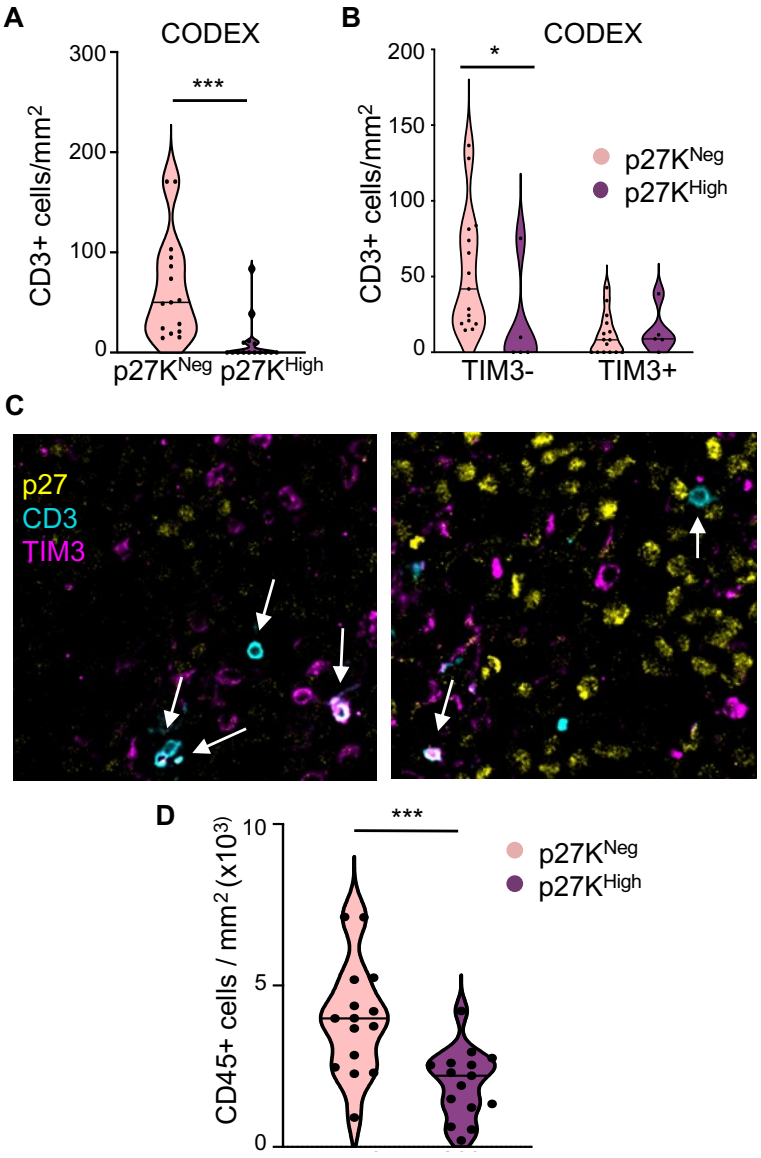

Figure 54. T cell exhaustion and immune infiltration analysis in QCC areas by CODEX®. Untreated 4T07 tumors were processed for CODEX®. A) CD3+ T cell density in p27K^{High} areas and p27K^{Neg}. B) Exhausted (TIM3+) and non-exhausted (TIM3-) CD3+ T cells inside p27K^{High} vs p27K^{Neg} areas (multiple areas from 4 tumors). Non-parametric Wilcoxson test was used. C) Representative picture of CODEX visualization for p27, CD3 and TIM3 markers. Arrows point to T cells. D) CD45+ cell density quantification from tumors in figure 45. Multiple regions were quantified from 4 different

tumors. *P<0.05, ***P<0.001.

Furthermore, we used CODEX to characterize T cell exhaustion in GFP-expressing tumors upon treatment with Jedi T cells. This confirmed that the small clusters of surviving GFP+ cancer cells after Jedi attack (described in Figure 13) displayed lower T cell infiltration (Figure 55A). The few T cells that were able to infiltrate GFP+ areas were more exhausted (Figure 55B, C, D). Thus, all these data demonstrated that the QCC niche was less infiltrated, with more exhausted T cells.

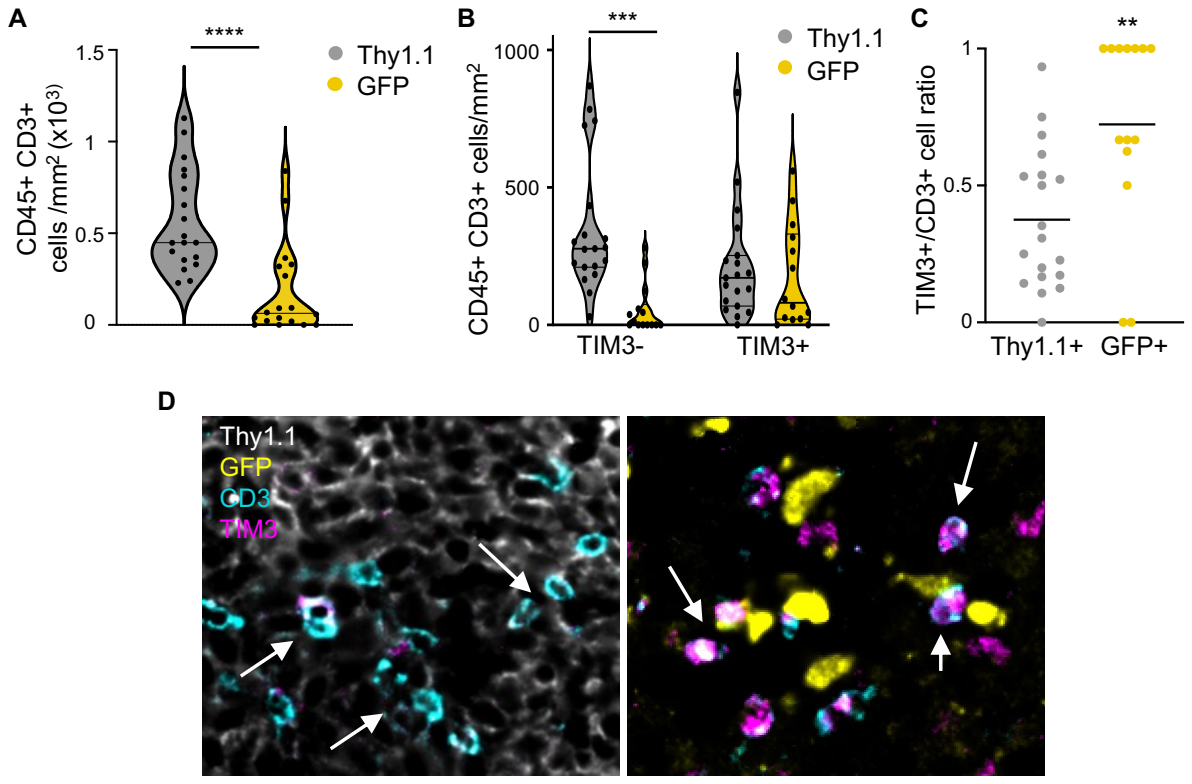

Figure 55. T cell exhaustion in areas with GFP cells surviving T cell killing. 4T07 Thy1.1:GFP mix tumors after treatment with 5M Jedi T cells were processed for CODEX® (Multiple areas from 3 tumors). A) Quantification of CD3+ cells density in the different tumor areas from GFP surviving cells of Thy1.1 control cancer cells. B) Exhausted (TIM3+) and non-exhausted (TIM3-) CD3+ T cells in GFP+ vs Thy1.1+ regions. C) TIM3+/CD3+ T cell ratio in GFP+ areas versus Thy1.1+ areas. D) Representative image, arrows point to T cells. **P<0.01, ***P<0.001, ****P<0.0001.

3.9. Dendritic cells inside clusters of QCCs express lower levels of key genes for T cell immunity

To uncover the immune populations that could contribute to T cell dysfunction in response to local hypoxia, we quantified a hypoxic signature comparing cells inside and outside QCC regions. All subsets of conventional dendritic cells (cDCs)), considered the most important antigen presenting cells, showed the largest enrichment in hypoxia-induced genes: DC1 (identified by *Clec9a*, *Xcr1*, *Wdfy4*), DC2 (*Itgax*, *Sirpa*, *Cd209a*), and mregDCs (*Ccr7*, *Cd80*, *Cd200*, *Cd247*) (53)(Figure 56, 57, 58).

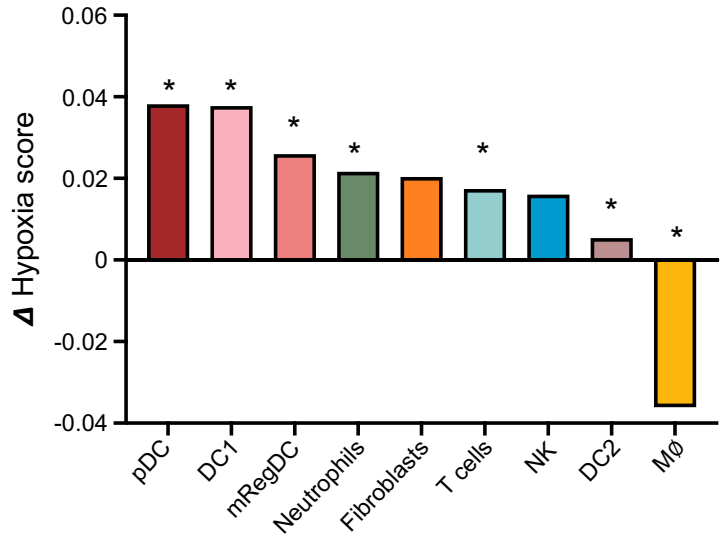

Figure 56. Hypoxic score evaluation across PADME-seq populations. Difference in expression of hypoxic signature comparing cells from p27K^{High} vs p27K^{Neg} regions from figure 44. *adj. p-value<0.05

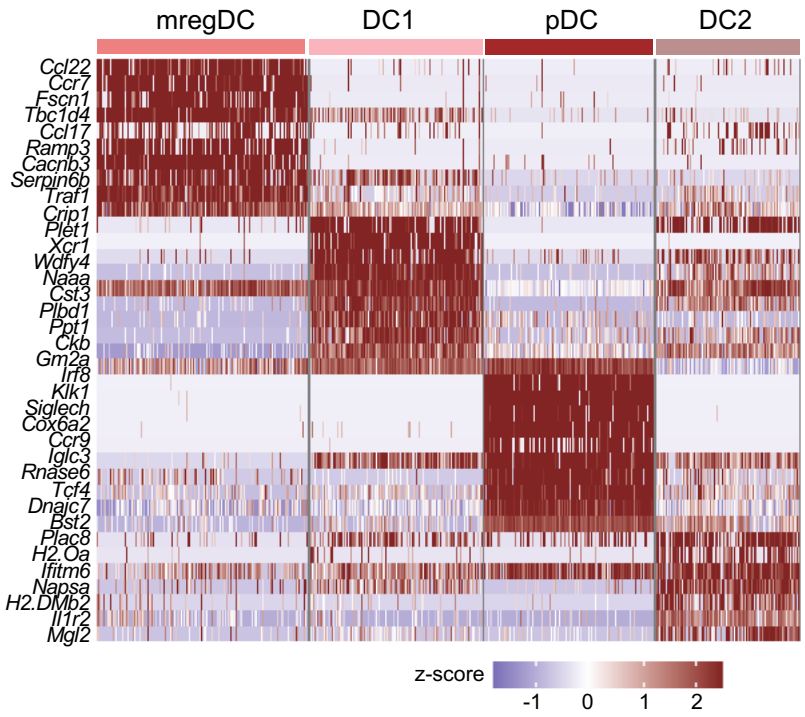

Figure 57. Top differentially expressed genes in DC clusters. Heatmap shows genes driving the DC clusterization in figure 33. Data is color coded to reflect gene expression Z-scores.

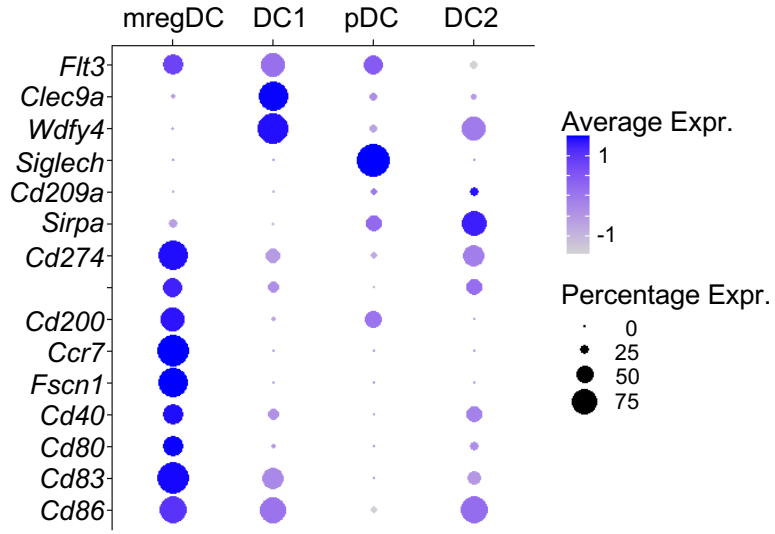

Figure 58. Expression of key markers to identify DC populations. Dot-plot graph shows expression levels and percentage of expression in every DC cluster from figure 44. Depicted genes were used for identification of DC populations.

Unsupervised GSEA of all cDCs showed a downregulation of innate immunity and immune-response pathways inside the QCC niche (Figure 59A). DC2s displayed a similar result, presenting a highly immune-dysfunctional state (Figure 59B, C). Key IFN-induced genes and other important genes for DC function were reduced in DC2 located in the QCC niche (Figure 59D).

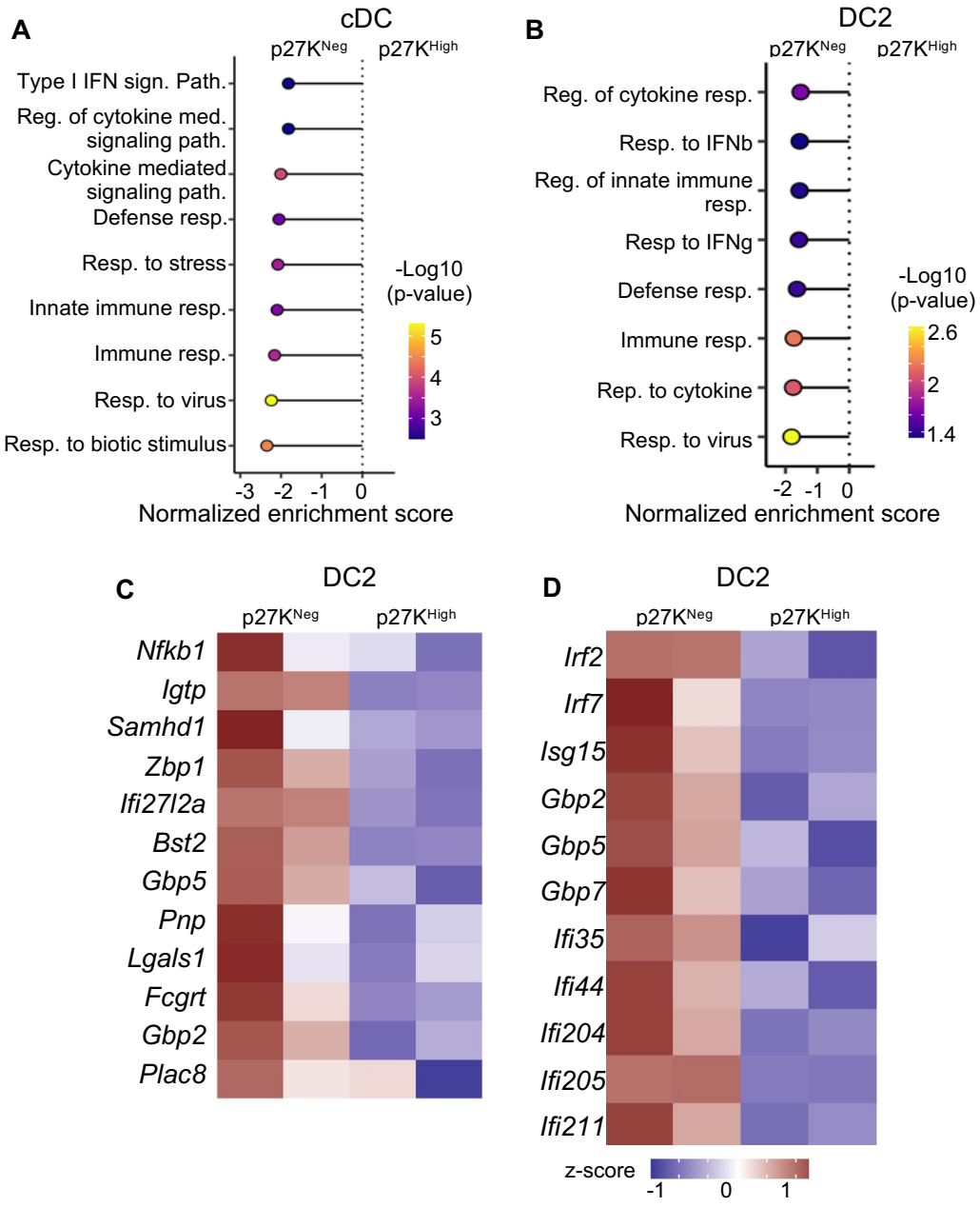

Figure 59. Differential expression of activation and IFNg response genes in DCs based on their location in tumor. A-B) Unsupervised gene-set enrichment analysis performed in all cDC (A) and

DC2 specifically (B) comparing p27^{High} vs p27^{Neg} areas. C) Heatmap differential expression of relevant genes in Figure 51 across cDC from p27K^{High} vs p27K^{Neg} areas. D) Heatmap of differentially-expressed interferon-induced genes comparing DC2 from p27K^{High} vs p27K^{Neg} areas. Z-score normalized data is shown.

We then focused on mregDCs, which are DCs that have taken up tumor antigen, being key for anti-tumor immunity (53). Since this is a newly identified subset, we analyzed expression of functionally relevant genes based on literature (Figure 60). mregDCs in the QCC niche displayed lower expression of MHCI and MHCII-related genes, suggesting a diminished ability to present antigen. They also displayed lower expression of *Cd81* and *Il12a* and *Il12b*, a key cytokine for T cell responses (54). Moreover, mregDCs in the QCC niche had lower expression of *Fscn1* (Fascin1), which is expressed in migratory DCs (140), suggesting a reduced capacity to migrate to lymph nodes.

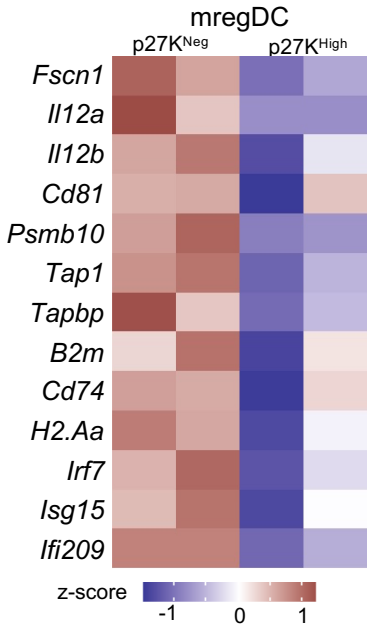

Figure 60. Differential expression of key genes involved in mregDC function. Heatmap of differentially-expressed key functional genes in mregDC from p27K^{High} vs p27K^{Neg} areas. Z-score normalized data is shown.

To validate our findings about cDCs from PADME-seq at the protein level, we quantified MHCII in DCs by both conventional immunofluorescence (Figure 61) and CODEX (Figure 62). In both settings, DCs displayed lower MHCII when they were located inside QCCs areas. Therefore, DCs within the QCC niche displayed a phenotype consistent with an impaired ability to recruit and activate T cells.

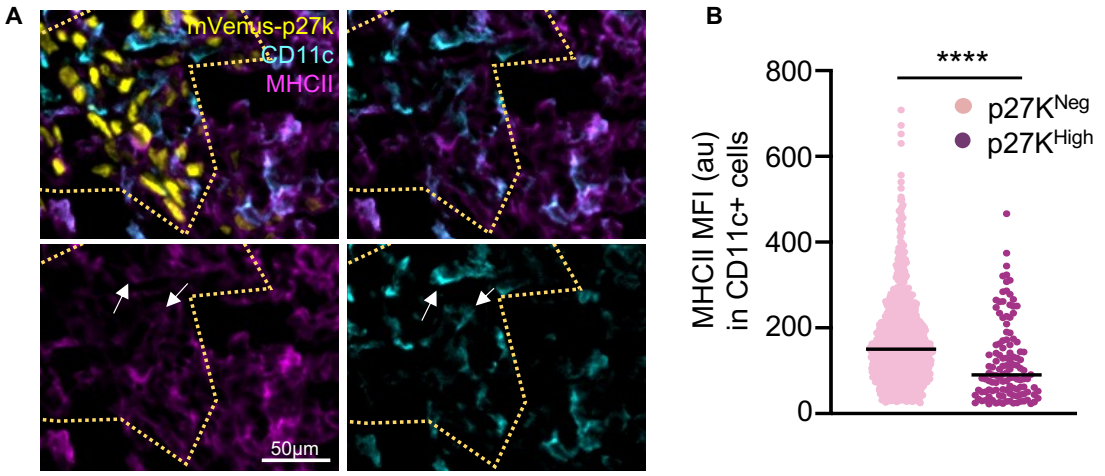

Figure 61. Conventional immunofluorescence analysis of MHCII expression in QCC areas. A) Representative immunofluorescence image of MHCII and CD11c staining in mVenus-p27K-expressing tumors (n=3 tumors). B) MHCII intensity in CD11c+ cells from A (4 images from 3 tumors). ****P<0.0001.

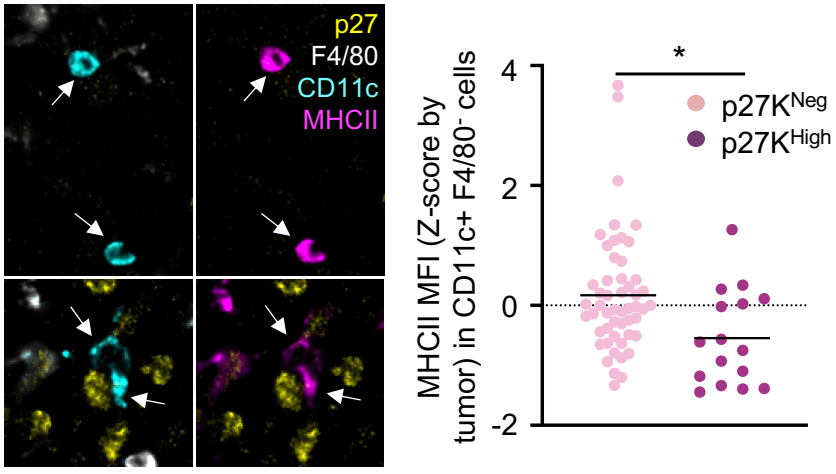

Figure 62. MHCII expression analysis using CODEX®. MHCII intensity in DCs from untreated 4T07 tumors. DCs were identified as CD45+ CD11c+ F4/80- CD3- (n=4 tumors). A) Representative picture. Arrow marks DCs. B) Intensity in the different DCs analyzed. Bar marks population mean. *P<0.05

Moreover, we quantified MHCII in GFP+ surviving areas from setting in Figure 13. In this setting cDC also presented downregulation of MHCII inside GFP regions (Figure 63). These results further emphasize the importance of DC in reinvigoration of T cells since the majority of T cells inside GFP areas were exhausted (Figure 55)

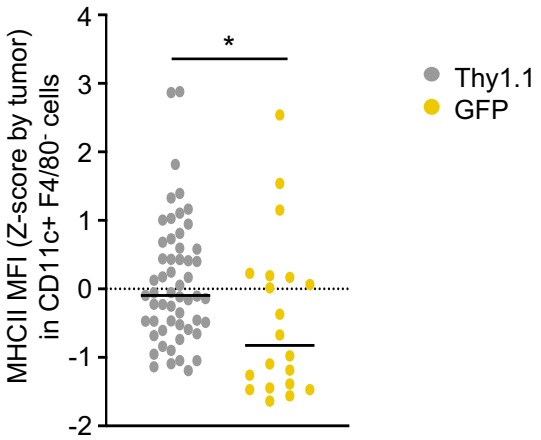

Figure 63. MHCII evaluation in DCs from GFP:Thy1.1 tumors. 4T07 Thy1.1:GFP mix tumors after treatment with 5M Jedi T cells were processed for CODEX® (Multiple areas from 3 tumors). DCs were identify as CD45+ CD11c+ F4/80- CD3-. MHCII was interrogated in all DCs found and plotted based on the area they were located. *P<0.05

Next, we investigated whether dysfunction in DCs was the direct effect of hypoxia by exposing bone marrow-derived DCs (141) to low oxygen levels. Steady-state DCs did not display any difference in key functional markers during hypoxia (Figure 64). Upon treatment with Lipopolysaccharide (LPS) and polyI:C, all DCs similarly became activated and upregulated MHCII, CD86 and CD40 regardless of oxygen concentrations. Thus, low oxygen had no effect on the ability of DCs to respond to danger signals (Figure 64).

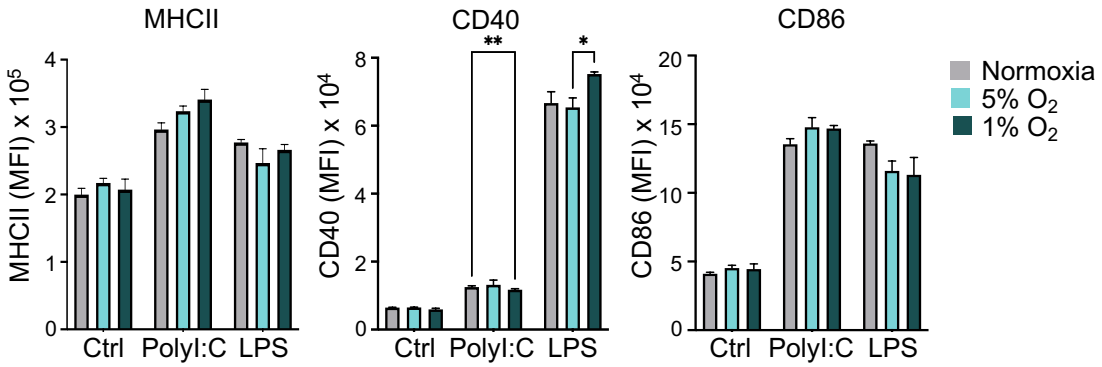

Figure 64. Effect of oxygen concentration in DC activation. Bone marrow-derived DCs were treated with LPS or PolyI:C for 18h while exposed to different oxygen levels. DCs were pre-conditioned at the specified oxygen concentration for 2h prior to adjuvant treatment. Graph shows mean±sem of MFI for depicted activation markers (n=3). *P<0.05, **P<0.01.

3.10. Specific activation of HIF1a in tumor cells abrogates anti-tumor immunity.

Since QCCs displayed a transcriptional signature related to hypoxia, we assessed whether the immune-suppressive niche orchestrated by QCCs was the result of HIF1a activation in tumor cells. To this end, we engineered 4T07 cells to express a constitutively active form of HIF1a that was named as HIF1a stable or HIF1a^{STBL} (108). HIF1a^{STBL}-expressing cells grew slower in vitro (Figure 65) but upon in vivo injection, breast carcinomas showed no statistical differences in weight compared to WT tumor cells (Figure 66).

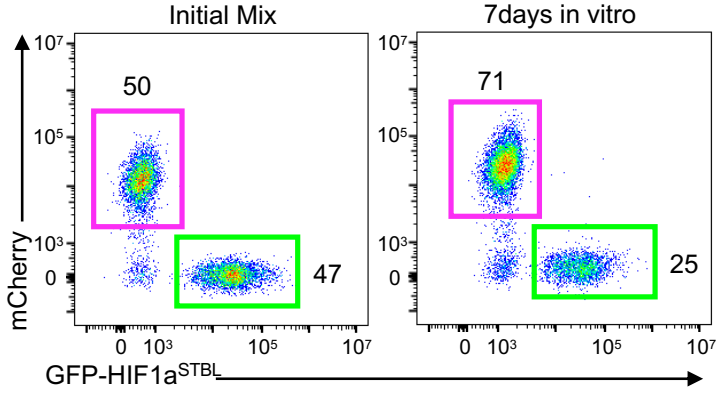

Figure 65. In vitro cell cycle evaluation of constitutive Hif1a stabilization. WT mCherry+ 4T07 cells were seeded 1:1 ratio with HIF1α^{STBL} GFP+ 4T07 cells and cultured for 1 week. Representative flow cytometry plots are shown.

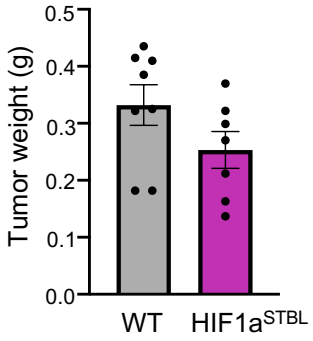

Figure 66. Hif1a constitutive stabilization in cancer cells does not affect tumor weight. 4T07 cells were transduced with either mCherry or mCherry ires Hif1aSTBL that results in a mutated Hif1a protein stable in normoxic conditions. Tumors were grown with either WT or Hif1a STBL cells in Balb/c mice. Graph shows tumor weight at end point. (n=7)

HIF1a^{STBL} displayed a reduced infiltration of CD8+ T cells, and specifically of the less exhausted subset of TIM3- T cells (Figure 67). Moreover, membrane MHCII protein levels were lower in DCs as measured by flow cytometry (Figure 68), similar to the phenotypes that we observed in infiltrating T cells and DCs inside the clusters of QCCs.

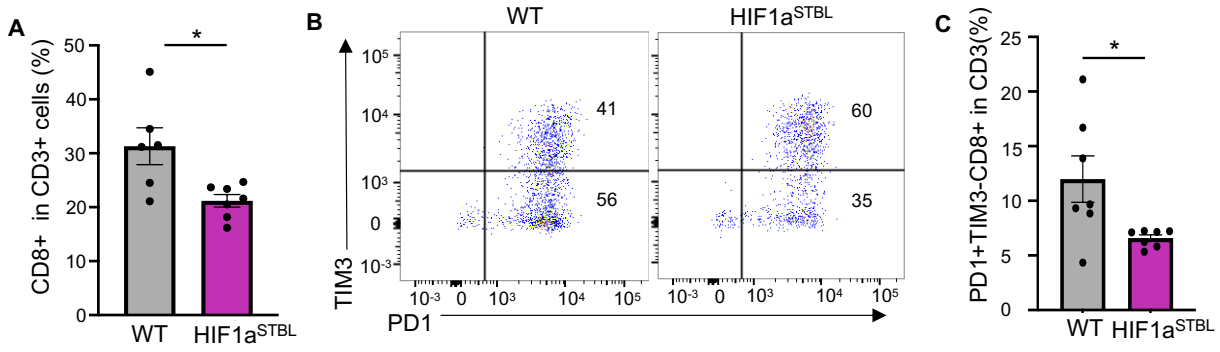

Figure 67. Effect on T cell infiltration and exhaustion in tumors with constitutive Hif1a stabilization. A) Percentage of CD8+ T cells in WT or Hif1a^{STBL} 4T07 tumors (n=5 mice). (B-C) T cell

exhaustion in CD8+ T cells from A. (B) Representative plot. (C) Mean±sem of PD1+ TIM3- CD8+ T cells (n=6 mice). *P<0.05.

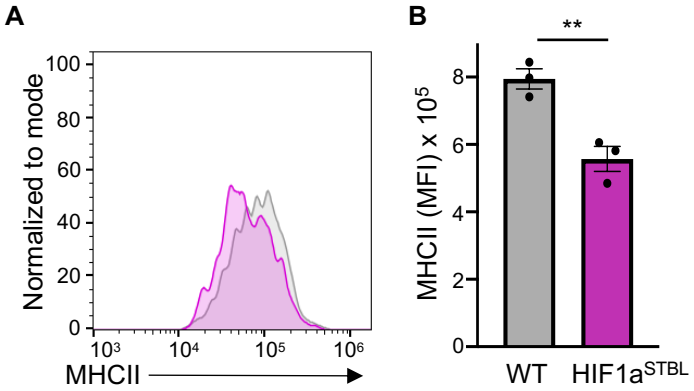

Figure 68. Effect on DCs with constitutive Hif1a stabilization. A) MHCII protein levels in DCs from WT or Hif1a^{STBL} 4T07 tumors (n=5 mice). B) Mean±sem of MFI. **P<0.01.

To investigate whether these alterations could cause resistance to anti-tumor T cell immunity, we generated breast tumors from Cherry+ 4T07 cells mixed with either GFP+ wild-type or GFP+ HIF1a^{STBL} cells (Figure 69).

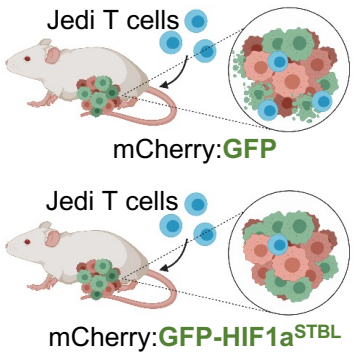

Figure 73. Experimental diagram to assess Hif1a constant stabilization in cancer cells immune evasive properties. Mix GFP:mCherry tumors were grown with GFP cells being either WT or Hif1aSTBL. 7M Jedi T cells were adoptively transfer 1 week after tumor implantation.

Although only a fraction of cancer cells had HIF1a^{STBL}, DCs showed a trend to lower MHCII levels (Figure 74A, B). Moreover, mixed mCherry with GFP-HIF1a^{STBL}-expressing

tumors showed a ~50% reduction in CD8+ T cell infiltration and the infiltrating T cells were mostly excluded from GFP+ regions (Figure 74C, D).

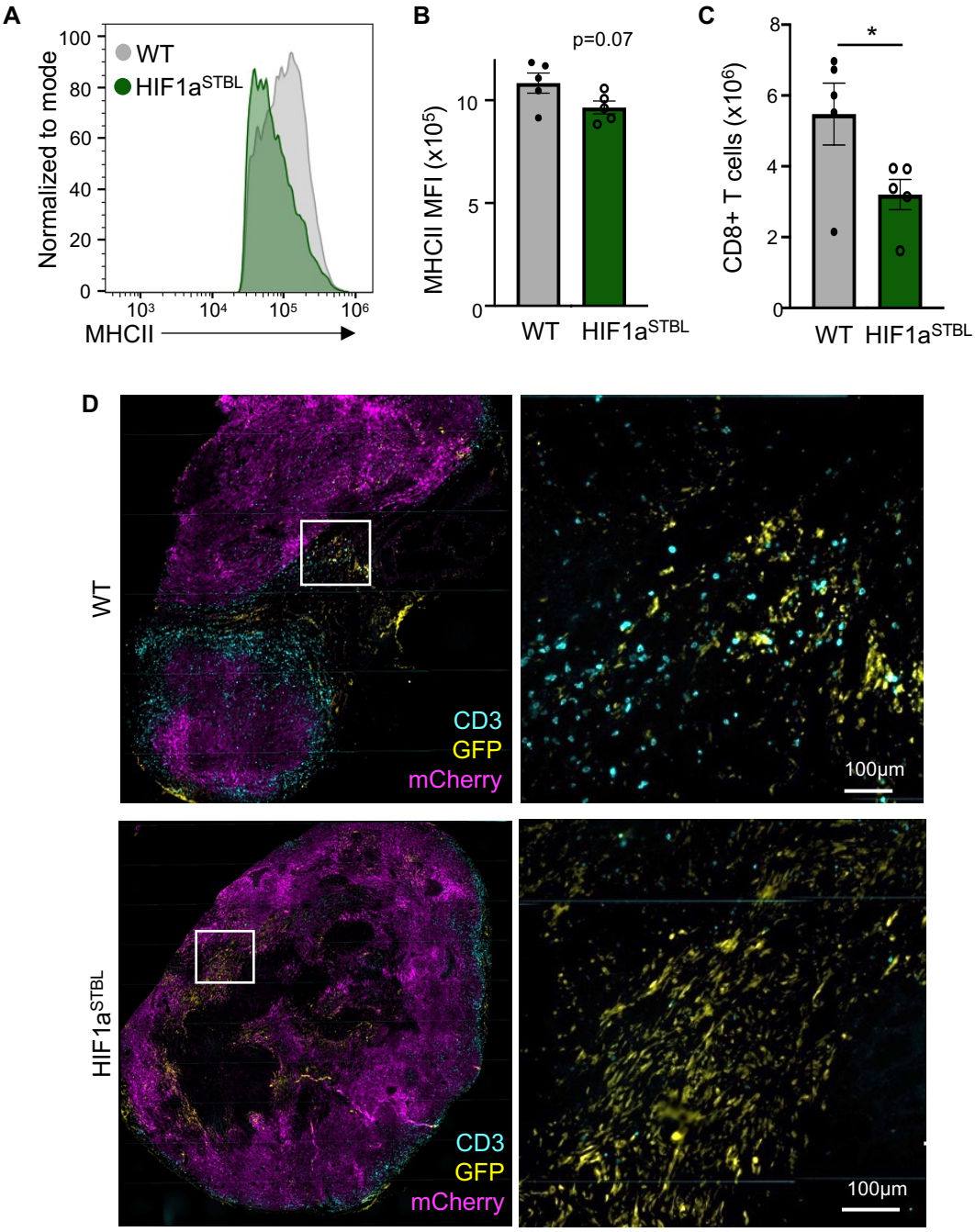

Figure 74. Analysis of TME from GFP:mCherry tumors with or without Hif1a stabilization. A,B) MHCII staining in tumors from Figure 73. A) Representative histogram. B) Graphical representation of mean±sem of MFI. C) Total CD8+ T cells analyzed by flow cytometry in WT or Hif1a^{STBL} 4T07 tumors.

D) Representative tumor section with CD3 immunofluorescence. Images on the right show GFP and CD3 from corresponding inset of images on the left. (n=5 mice). *P<0.05.

Upon adoptive transfer of Jedi T cells, WT tumors showed <6% of surviving GFP+ cells, demonstrating efficient killing. Conversely, ~26% of GFP+ HIF1a^{STBL} cells survived, constituting a 4-fold increase (Figure 75).

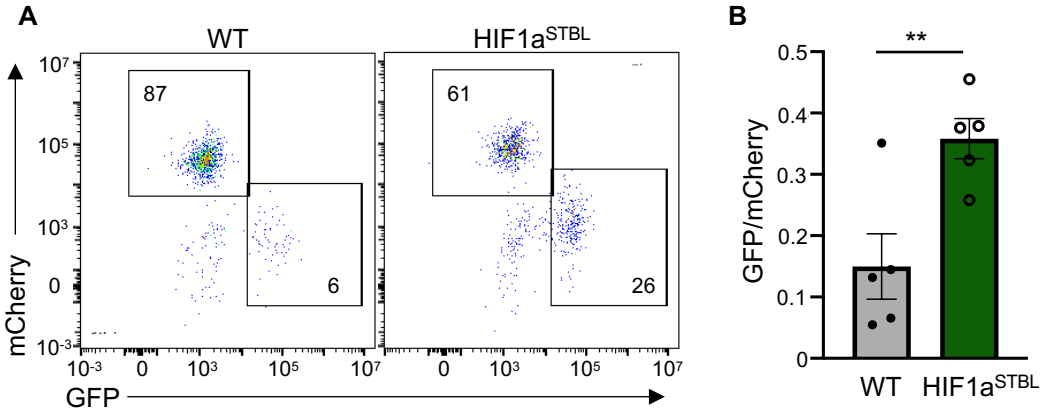

Figure 75. GFP survival is increased by Hif1a constitutive stabilization. A) Representative flow cytometry of surviving GFP+ cells in tumors from Figure 73. B) Mean±sem of GFP:mCherry cells ratio in tumors from A. (n=5).

Then, we sought to investigate the possible therapeutic benefit of modulating HIF1a in cancer cells to enhance anti-tumor immune responses. To address this, we generated *Hif1a* knockout GFP+ 4T07 cells using CRISPR/Cas9 (Figure 76).

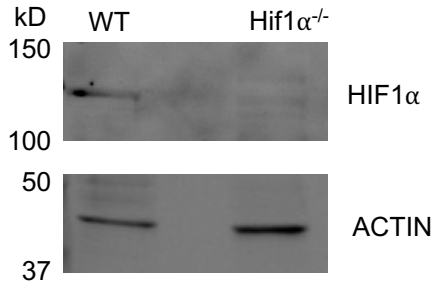

Figure 76. Hif1a KO confirmation by western blot. HIF1A levels in WT and *Hif1a*-/- 4T07 cell lines by Western-blot. Actin was used as loading control.

Mice with either WT GFP+ or *Hif1a*-/- GFP+ tumors were treated with Jedi T cells. This led to a larger reduction in size in *Hif1a*-/- tumors compared to WT (Figure 77A). Both endogenous CD8+ T cells and adoptively transferred CD45.1+ Jedi T cells displayed increased numbers and reduced exhaustion in *Hif1a*-/- tumors (Figure 77B, C, D) compared to those infiltrating WT tumors.

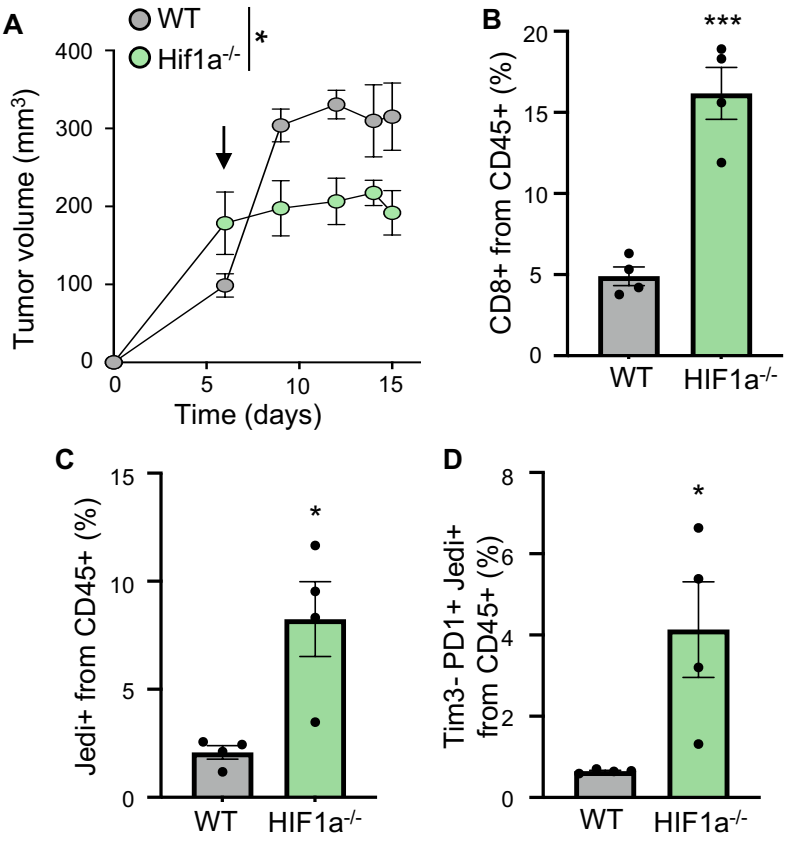

Figure 77. Therapeutic benefit of Hif1a KO in cancer cells. A) Area under the curve of tumor growth in *Hif1a*-/- GFP and WT GFP tumors upon treatment with 5M Jedi T cells (n=4 mice). B) Mean±sem of percentage of CD8+ T cells in tumors. C) Mean±sem of percentage of Jedi T cells (CD45.1+) in tumors. D) Mean±sem of percentage of TIM3- PD1+ Jedi T cells in tumors. (n=5). ***P<0.001.

To further understand the impact in the TME of the activation or absence of the HIF program in cancer cells; we performed scRNAseq in our mCherry+ 4T07 model WT, Hif1a-/- or HIF1a STBL. After data normalization and clusterization the UMAP representation showed 9 main clusters of cells (Figure 78A). We were able to identify the

main immune population based on well-known markers as done in our previous scRNAseq datasets (Figure 78B). We then analyzed the composition of each tumor type. WT tumors were a middle point between Hif1a-/- and HIF1a STBL tumors in regards of TME composition (Figure 78C). As expected HIF1a STBL tumors had a decreased population of lymphocytes. This emphasized the role of HIF1a as an immune modulator and the main factor driving QCC phenotype.

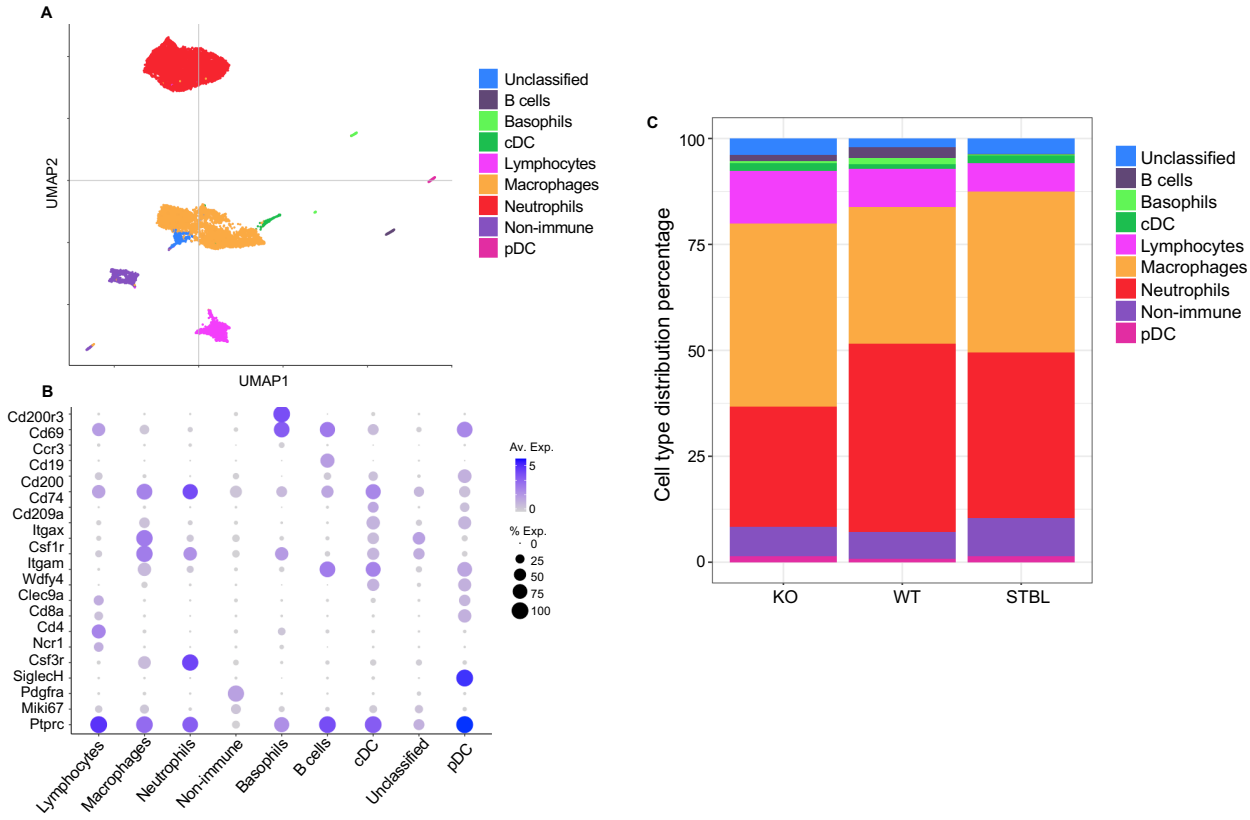

Figure 78. scRNAseq analysis of TME in tumors with different states of HIF1a activation. A) UMAP representation of all cells analyzed. B) Expression levels of markers used to define the different populations. C) TME composition in the different tumor types.

Since we observed also differences not only in T cell numbers but also in T cell state inside and outside QCC areas. We wanted to know if this phenotype was also recapitulated by HIF activation on our tumors. We reclustered the lymphocyte cluster to deepen in this population (Figure 79A). We obtained 10 new clusters that we identified

based on the markers previously described (Figure 79B). We identified a cluster of Tprog-exh T cells with Pd1+ Tim3- and a mixture population of both CD8 and CD4 T cells. This Tprog-exh cluster was more abundant in our Hif1a-/- tumors and reduced in the HIF1a STBL samples (Figure 79C). On the contrary, the Pd1+ Tim3+ CD8 T cells cluster that we identified as Tterm-exh was the predominant cluster in the HIF1a STBL tumors, even more so than in WT tumors. Thus, HIF1a stabilization was inducing T cell exhaustion as observed in QCC areas.

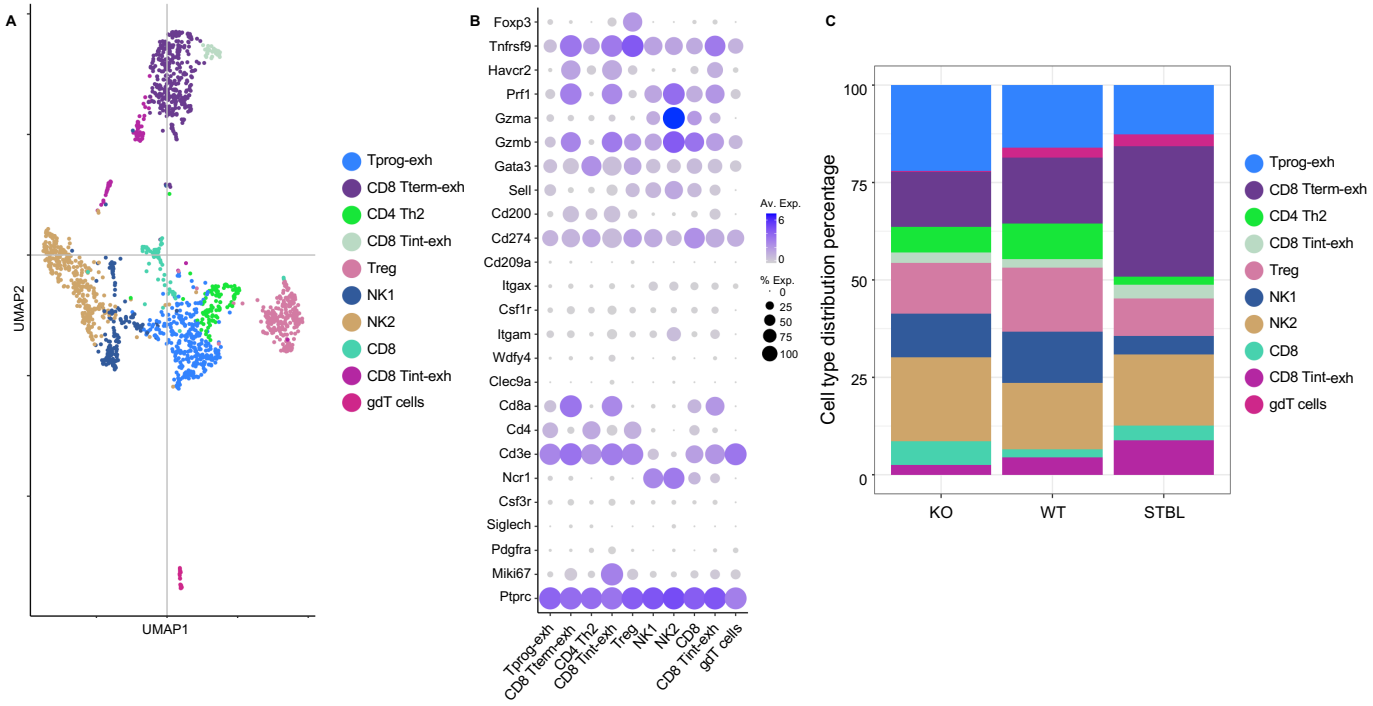

Figure 79. scRNAseq T cell analysis in tumors with different states of HIF1a activation. Lymphocyte cluster from Figure 78 was reclustered on its own. A) UMAP representation of reclustering B) Expression levels of markers used to define the different populations of T cells. C) T cell composition in the different tumor types.

3.11. HIF1a activation in tumor cells but not in DCs impairs DC activation.

These previous results suggest that HIF1a activation in cancer cells restricts T cell infiltration and increases T cell exhaustion, possibly through forcing DCs into a less activated phenotype (Figure 80).

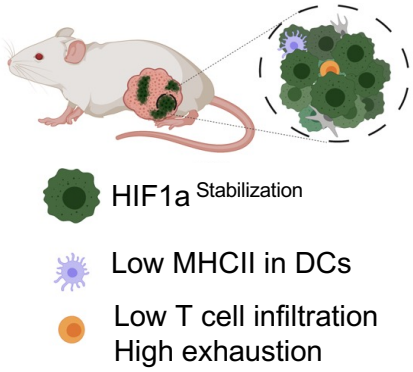

Figure 80. Schematic summary of the effects of HIFa^{STBL} in tumor cells.

We investigated further the state of DCs in 4T07 Hif1a STBL vs Hif1a KO tumors. The use of fluorescently labelled tumor cells allows for identification of DCs that have phagocyted tumor cells as they will show some fluorescent signal. Although we did not see statistically significant differences, we observed a trend to higher percentage of mCherry+ DCs in Hif1a KO tumors compared to Hif1a STBL (Figure 81A). This phenotype was observed in both DC1 and DC2 populations. DCs increase surface levels of the chemokine receptor CCR7 upon antigen uptake, which is key for their migration to the draining LN. We measured CCR7 in tumor DCs and we found that CCR7 expression was higher in Hif1a KO tumors (Figure 81B), indicating a more functional DC phenotype.

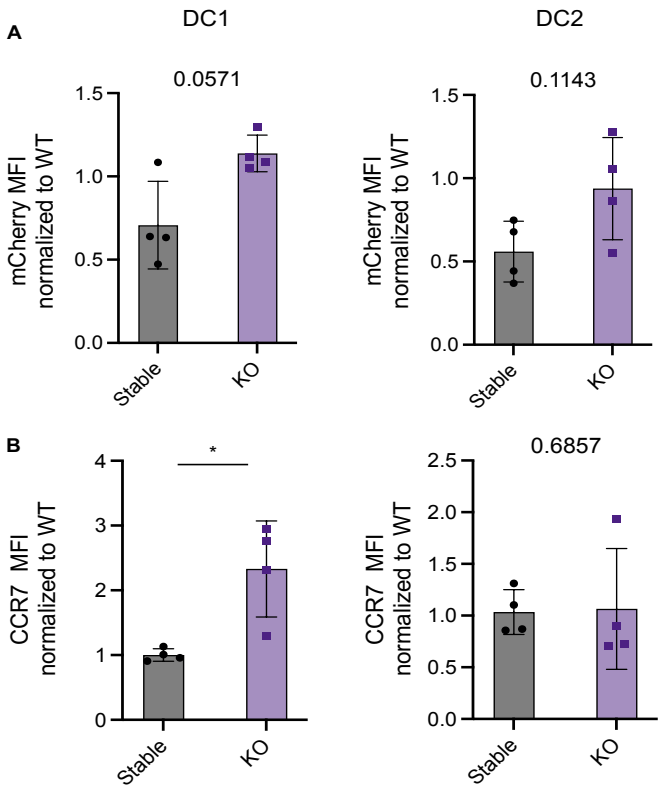

Figure 81. DC functionality in response to Hif1a state in tumor cells. 4T07 tumors transduced with mCherry Hif1aSTBL or mCherry, Hif1a KO was performed in the mCherry+ cells. These groups were injected into Balb/c mice and processed 2 weeks after injection by flow cytometry. A) MFI analysis of mCherry signal in DC subgroups normalized to the WT tumor. B) MFI analysis of CCR7 signal in DC subgroups normalized to the WT tumor. (n=4) *P<0.05**.**

We aimed to discern the possible deleterious effect of HIF1a in DCs in contraposition to the orthogonal role of HIF1a activation in tumor cells. To assess this, we generated mice that were knockout for HIF1a only in cDCs to investigate whether blocking HIF1a activation in DCs could improve their function in tumors. To this end, we obtained mice that express the CRE recombinase specifically in cDCs under the control of the Zbtb46 genes (Zbtb46-Cre) (142) and we bred them with mice carrying flox sequences in the Hif1a gene (Hif1a$^{fl/fl}$). We obtained mice that were homozygous for the Hif1afl/fl allele and carried the Cre transgene and we used littermates that were also homozygous for Hif1afl/fl and negative for Cre as controls (Figure 82). We inoculated these Hif1a-KO^{DC} and littermate controls with the well-established melanoma model B16F10, which is

known to be resistant to ICB treatment. The elimination of Hif1a in DCs did not affect the response to anti-PDL1 treatment (Figure 82). These results suggest that impairment of DC function in tumors related to hypoxia is not the result of HIF1a activation in DCs.

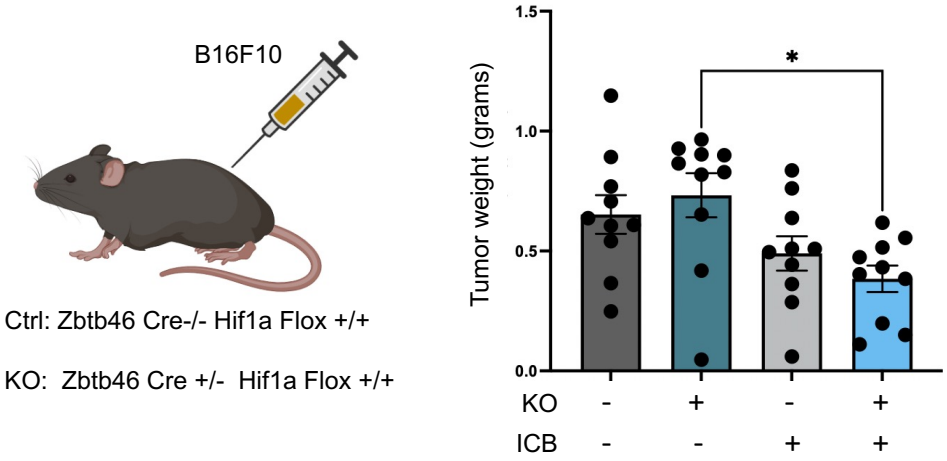

Figure 82. Hif1a loss in DC population does not affect ICB response. B16F10 melanoma tumors were implanted in either control mice (Zbtb-Cre-/- Hif1a+/+) or mice with DCs lacking Hif1a (ZbtbCre+/- Hif1a+/+). ICB treatment with 100ug/mouse of aPD1 antibody was started on day 10 after implantation and repeated every 4 days. Tumors were harvested at day 21. Graph depicts tumor weight. (n=10) *P<0.05.

3.12. Lactate may drive immune dysfunction of DCs.

Once we proved that DCs were not affected by their own HIF1a but instead by HIF1a in the tumor cells, we aimed to discover the mechanism of this bystander effect. QCCs were likely secreting something that turned near cells immune-suppressive. Since QCCs display high HIF1a activation and high glycolysis, our hypothesis was that the signal was a metabolite derived from the glycolytic pathway. Thus, we took advantage of scRNAseq-seq from the TME from Figure 44 and we analyzed the expression of metabolite transporter genes. We observed expression of Mct4 in all immune and stromal cells (Figure 83). Notably, Mct4 has been reported to be responsible for the uptake of lactate

from the environment (143). This suggests that immune cells may be taking up higher levels of lactate when they are close to QCCs than when they are far from them.

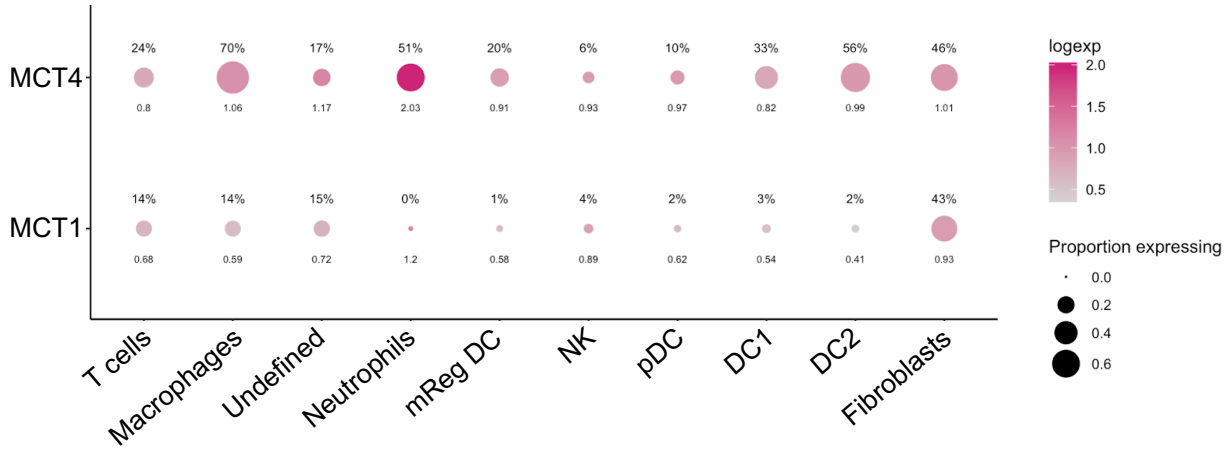

Figure 83. Lactate transporters are highly expressed in immune infiltrates. scRNAseq data from Figure 44. Graph shows expression levels of lactate transporters across different populations of tumor infiltrates.

We used Hif1a STBL and KO tumors to measure lactate by mass spectrometry to confirm that HIF1a activity in tumor cells increases lactate production. Lactate concentration was the highest in STBL tumors and lowest in the KO with the WT tumors showing intermediate levels (Figure 84).

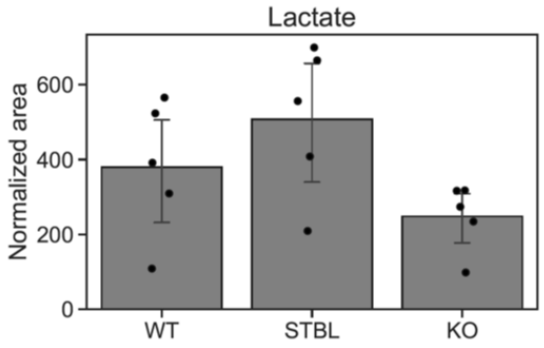

Figure 84. Lactate quantification in 4T07 tumors with different Hif1a states. 4T07 mCherry+ tumors either WT, Hif1a KO or transduced with mCherry Hif1a STBL were grown into Balb/c mice and harvested after 2 weeks. Graph depicts total lactate quantification normalized to internal control.

Next, we assessed if lactate could impair DC activation *in vitro*. CD86 expression in response to PolyI:C was inversely correlated to the lactate concentration in the media (Figure 85). We used a range of lactate concentration from physiological (2mM) where we did not observe any affect to tumoral concentrations that can range from 10 to 40mM (144). In the highest concentrations DC become highly dysfunctional being unable to upregulate CD86. This could explain why more dysfunctional DC are localized in QCC areas where lactate concentrations are expected to be the highest.

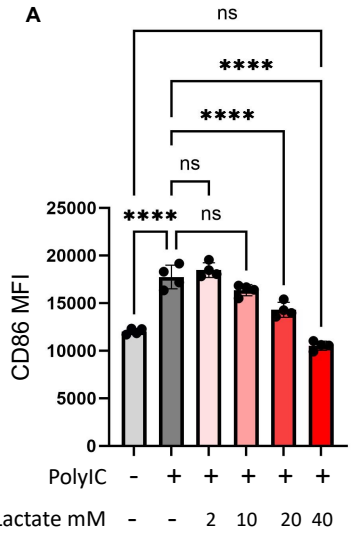

Figure 85. DC activation in vitro in response to lactate. Splenic DCs were isolated and cultured in vitro in presence or absence of PolyI:C and different lactate concentrations. Quantification of CD86 MFI as a surrogate of activation. (n=4) ****P<0.0001.

Our data, together with previous reports correlating HIF1a to chemotherapy-resistance (132), suggest that HIF1a activation in tumor cells induces a multi-resistance phenotype. This phenotype induces a highly glycolytic state that will result in elevated lactate concentration. Lactate could be potentially impairing the immune niche by inactivating DCs breaking the immune cycle and generating a dysfunctional niche unable to response to immunotherapy. Thus, our work has identified a crucial cancer population that orchestrates an immune suppressive TME and must be eliminated for treatment success.

4. DISCUSSION

Uncovering the mechanisms that regulate the abundance and distribution of immune cells inside tumors represents an outstanding question in biomedical research. Identifying these drivers can predict which patients will benefit from immunotherapy. Even more importantly, this is essential for developing strategies that allow resistant patients to respond. Focusing on breast cancer, here we discovered a population of tumor cells that formed intra-tumor clusters where immune infiltration was highly reduced, revealing an until now hidden driver of immune exclusion. These clusters of cancer cells were resistant to T cell attack and their most notable feature was quiescence. Rather than constituting an inert population in cell cycle arrest, these quiescent cancer cells (QCCs) displayed higher tumor initiation potential than other cancer cells. Our work exposed QCCs as “dangerous” cells that not only escape from T cell killing but also possess the ability to re-grow tumors. Our findings indicate that tumor dormancy is linked to immune evasion and suggest that QCCs may constitute the seeds for recurrent disease after immunotherapy.

Since most cancer studies focus on mechanisms controlling tumor growth, quiescence in the tumor mass has been less studied, with some exceptions (93) (94). In this study we identified quiescence as the top feature of tumor cells that escape from T cell killing in primary breast cancer. We showed that these surviving cancer cells were already in a p27+ quiescent state prior to T cell adoptive transfer. However, the transcriptomes of surviving GFP+ cancer cells from Jedi-treated mice and QCCs from untreated animals did not show a clear overlap, mostly due to an increase in IFN and inflammatory signatures in GFP+ cells in response to strong Jedi cell killing. Since IFN has been shown to induce dormancy in disseminated tumor cells (98) we studied its role in QCC formation. We focused on type I IFN since it was one of the top GO pathways in GFP+ resistant cells and because QCC were also present in the absence of an adaptive immune system. We showed type I IFN did not have a role in QCC. However, we did not explore further the similarity of QCC in immune deficient mice, with those of immune competent animals. The difference in number of GFP+ resistant cells vs QCCs point to some level of heterogeneity inside QCC population in immune competent animals. Therefore, it would be worth to further study this heterogeneity both in the presence and absence of the

immune system as it is still possible that other inflammatory ques, as well as type II IFN, can be playing a role in the induction of different QCC flavors.

This intra-tumor quiescent phenotype is different from the process known as cellular tumor dormancy, which has been described mainly in disseminated tumor cells (145) (146). Although they all share the same principle: G0/G1 cell cycle arrest; they might differ in the ques and cellular programs that induce this observation. While cellular dormancy of disseminated tumor cells has been described to be induced by IFN (98), eliminating IFNAR1-/- in our model did not impair QCC formation. In our system the quiescent state seems to be induced by hypoxia, another environmental queue abundant in the TME. Hypoxia induced cell cycle arrest has also been linked to senescence, a cellular arrest that occurs in response to harsh environmental conditions (147). Of note, senescent cells are usually associated to inflammation and increased immunogenicity, contrary to the immune evasive properties of QCCs. In fact, Cdk4/6 inhibition in breast cancer patients works by inducing senescence and enhancing tumor immunogenicity (148). In contrast to the G0 arrest of quiescence; senescence can be found in other cell cycle phases like G2 and it is considered a terminal state (149). Unlike senescent cells, QCCs are a plastic phenotype that can be reverted. Rather than a terminal state QCC phenotype shows a higher tumorigenic potential when compared to proliferative cells from the same tumor.

We did not uncover whether this enhanced potential was the result of an inherent resistance to cell death, their immune evasion properties, or higher stemness potential. We showed HIF1a program was sufficient to recapitulate them, however it is unclear if hypoxia alone is inducing this program or if there is a combinatorial effect. It is already known how glucose starvation can induce HIF1a but there is evidence of HIF1a activation in immune cells in homeostasis without either hypoxia or metabolic restriction. A recent study showed mechanical force sensed by macrophages can induce HIF1a stabilization (150). This connection is extremely important in the tumor setting where fast proliferation is increasing cell density and therefore the pressure and forces sensed by them. It is possible that high density triggers the HIF1a program inducing highly glycolytic cells that will drain nutrients from already crowded and competitive areas. Of note, QCC areas

seems to be present in highly compacted areas of TME and although they are labeled by the hypoxic marker pimonidazole, they do not always localize away from vessels. Further studies are needed to understand the connection between activation of HIF1a and cell cycle arrest.

Importantly, reports from the IMpassion130 trial analyzing RNA-seq data from >800 TNBC patients revealed “proliferation” as a feature that correlated with response to ICB. Conversely, “angiogenesis” (a hypoxia-induced pathway that we observed in QCCs) was associated with resistance to ICB (65). Thus, a metabolically distinct cancer sub-population of quiescent cells comprises the fittest to survive upon T cell attack, becoming reservoirs of resistance (and probably recurrence) during ICB treatment in TNBC.

One of the strongest mechanisms to escape from T cell killing is by downregulation of antigen presentation (151). For example, disseminated pancreatic cancer cells survive during anti-tumor T cell responses by losing MHCI protein (128) while quiescent stem cells decrease MHCI both at the RNA and protein level (152). Nevertheless, the quiescence program in primary breast tumors that we uncovered here did not reduce MHCI, illustrating an orthogonal mechanism to previously published means of T cell immune evasion. These differences may be the result of the surrounding environment around quiescent cells when they are in isolation in the liver as opposed to inside a complex tumor mass.

QCCs in TNBC were never found scattered, but instead, always formed clusters with low T cell infiltration. This pointed to a cooperative or environmentally driven mechanism of resistance to T cell-mediated immunity. To study complex tissular interactions in tumor areas it was of upmost importance to obtain single cell resolution. This requirement is not achieved by spatial capturing technologies, 10x Visium is currently at 10 cell resolution (153). Photolabeling techniques on the other hand do not provide specific spatial resolution for every cell, but they allow for true single cell transcriptomics (86). In our study we had a very well-defined area: we wanted to understand the QCC neighborhood; so photolabeling techniques were the perfect fit. However, Niche-seq performance in the tumor setting was very inefficient and lacked the capacity to have QCCs and control areas

from the same tumor. We developed PADME-seq to allow for multiple comparisons from the same tumor. It also democratizes the technique and ease the process since utilizes commonly used microscopy. Furthermore, PADME per se can be combined with other subsequent techniques such as flow cytometry, biochemical and metabolic approaches, or other “omics” high-throughput analyses (metabolomics, epigenomics…).

Using PADME-seq, we discovered that QCCs survived during adoptive T cell therapy through orchestration of a local hypoxic and immune-suppressive milieu that led to augmented T cell exhaustion. We exposed that while Terminally Exhausted CD8+ T cells were more abundant inside the QCC niche, Proliferating CD8+ T cells were more likely found outside these niches. Similarly, the percentage of PD1+ TIM3+ CD8+ T cells was greater inside clusters of QCCs. The underlying mechanism/s inducing this exhausted phenotype along with their location within the tumor mass had not been reported. Here we described the spatial distribution of these dysfunctional TIM3+ CD8+ T cells, identifying them near QCCs. We also found that HIF1a activation in tumor cells was sufficient to increase the numbers of these more exhausted T cells. Remarkably, genetic activation of HIF1a in T cells had been shown to improve their ability to eliminate tumors. Conversely, HIF1a loss in T cells had been demonstrated to impair anti-tumor T cell immunity (62) (154). Thus, these published data suggest that abrogated T cell function in regions of QQCs is not the result of HIF1a activation in T cells. Instead, we uncovered a circuit by which cancer metabolism altered T cells in an indirect manner through induction of suppressive fibroblasts and DCs. This finding can explain the incongruency of the previously reported beneficial role of HIF1a activation in T cells from the overall detrimental effect of hypoxia on response to immunotherapy (155) (63).

Nevertheless, we did not specifically identify a direct molecular link between HIF1a+ cancer cells and downstream impaired responses in DCs. Lack of oxygen and HIF1a did not alter DC function, but deprivation of nutrients along with unknown secreted factors by QCCs could be the underlying mechanisms. We showed that addition of lactate alone, a well-known byproduct of HIF1a activation, diminishes DC activation when present at tumor-like concentrations. Lactate is gaining importance as an immune modulator and its

role is clear in dampening the immune response; but the mechanisms governing this process remain unknown. A recent study has shown that lactate can bind histones in a process called lactylation (156). Histone lactylation can act as an epigenetic regulator and could be the responsible of immune dysregulation in the TME. Understanding this process might hold the key to revert immune dysfunction and tilt the balance toward successful anti-tumor immune responses.

In summary, our work discovered that primary TNBC contained a population of QCCs with the ability to resist T cell attack. These QCCs, through activation of HIF1a, orchestrated a micro-niche with unfit DCs, suppressive fibroblasts, reduced T cell infiltration, and enhanced T cell exhaustion. Development of strategies to overcome immune suppression around QCCs and eradicate these cells will be key to improving responses to immunotherapy in TNBC and prevent recurrence after these treatments.

Future perspective

1. **Study QCC heterogeneity:** scRNAseq analysis from p27High populations from immune competent and immune deficient animals would allow to stablish the heterogeneity of this population and determine the role of the immune system in its formation with inflammatory cytokines like IFN.
2. **Understand QCC higher tumorigenic potential in relationship with immune evasion and stemness**: QCCs are more efficient at generating tumors in immune competent mice but it is unclear if this is a stemness phenotype or the result of immune evasion. Perform reinjection experiments with limiting dilutions of p27High and p27Neg cells in both immune competent and deficient mice.
3. **Uncover mechanisms by with lactate alters DC function**: we would need first to clarify lactate effect in DC is the main responsible of immune disfunction. Ldha-/- tumors as well as WT tumors in animals missing the lactate transporters Mct1, Mct2 and Mct4 specifically in DC will help to clarify the role of lactate specifically on DC in immune dysfunction. Once proven, histone lactylation seems the most

straight forward regulation so we could check by flow cytometry with antibodies and perform cut&run to understand the genes that are being regulated.

4. Use computational tools and CRISPR screenings to **find cancer specific targets and regulators of HIF1a** that do not blunt HIF1a in T cells.
5. **Identify pharmacologic approaches to block HIF1a in tumor cells** as a possible therapeutic avenue exploring synergistic effects with ICB.

Graphical abstract

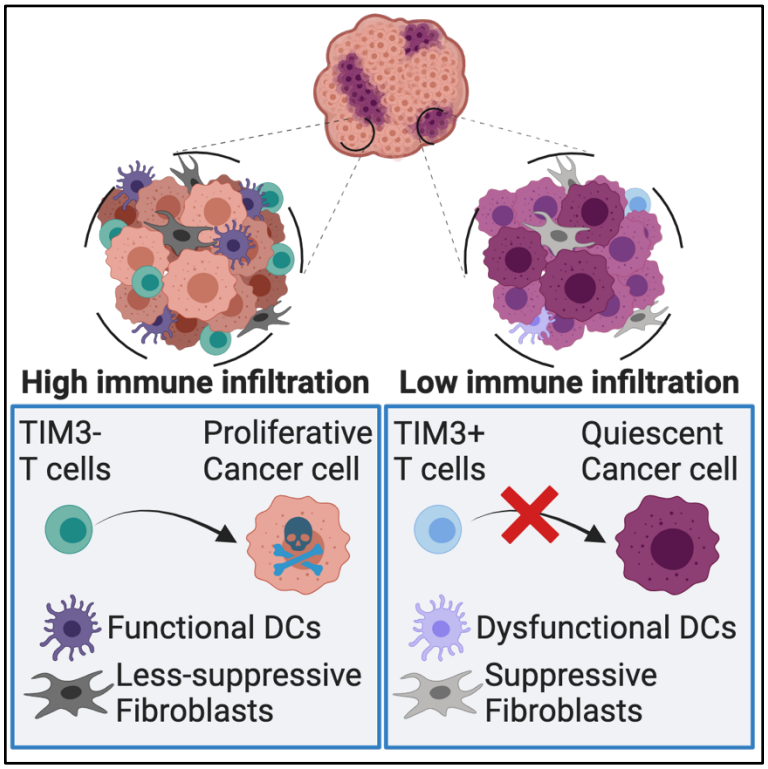

5. CONCLUSIONS

- Using a model antigen, we have discovered that inside tumors there is a phenotypically different population of cells, characterized by their quiescent state (QCCs), able to survive T cell killing.

- We have stablished PADME, a method to obtain single cell genomics with spatial resolution from different areas of the same tumor sample.

- Using PADME-seq we have uncovered that QCCs orchestrate the heterogeneous distribution of immune cells inside of a tumor, generating dysfunctional DCs, suppressive fibroblasts and inducing T cell exhaustion.

- We have demonstrated that QCC phenotype is regulated by HIF1a program which induction is sufficient to recapitulate the microenvironmental changes observed in QCC areas and improve survival to T cell killing.

6. MATERIAL AND METHODS

Materials and key resources

Table 1. List of all materials and key resources.

REAGENT or RESOURCE	SOURCE	IDENTIFIER
Antibodies		
aCCR7 Biotin	BioLegend	RRID:AB_389231 Clone:4B12
aCD11c PE	BioLegend	RRID: AB_313776 Clone:N418
aCD11c PE/Cy7	BioLegend	RRID: AB_493569 Clone:N418
aCD3 AF647	BioLegend	RRID: AB_389323 Clone:17A2
aCD3e biotin	BioLegend	RRID: AB_312668 Clone:145-2C11
aCD4 AF647	BioLegend	RRID: AB_493372 Clone:RM4-5
aCD40 PE/cy7	BioLegend	RRID: AB_10933422 Clone:3/23
aCD45 AF647	BioLegend	RRID: AB_493534 Clone:30-F11
aCD45 AF700	BioLegend	RRID: AB_493714 Clone:30-F11
aCD45.1 AF647	BioLegend	RRID: AB_492864 Clone:A20
aCD64 APC	BioLegend	RRID: AB_11219205 Clone:X54-5/7.1
aCD8 AF594	BioLegend	RRID: AB_2563237 Clone:53-6.7
aCD8 Pe/Cy7	BioLegend	RRID: AB_312760 Clone:53-6.7
aCD86 PE	BioLegend	RRID: AB_313150 Clone: GL-1
aGr1 APC	BioLegend	RRID: AB_313376 Clone:RB6-8C5
aH2Kd AF647	BioLegend	RRID: AB_493063 Clone:AF6-88.5
aH2Kd APC	BioLegend	RRID: AB_10640118 Clone:SF1-1.1
aHIF-1α XP® Rabbit mAb	Cell signaling	RRID: AB_2799095 Clone:D1S7W
aHuman CD3	Agilent	RRID: AB_2631163 Clone:F7.2.38
aHuman E-Cadherin	CST	RRID: AB_2291471 Clone:24E10
aHuman Ki67	Biocare	RRID: AB_2721189 Clone:SP6
aHuman p27K	BD	RRID: AB_397636 Clone:57/Kip1/p27
aIFNAR1 biotin	BioLegend	RRID: AB_1134250 Clone:MAR1-5A3
aKi67 mAb	Cell Signaling	RRID: AB_2620142 Clone:D3B5
aMHCII APC	BioLegend	RRID: AB_313328 Clone:M5/114.15.2
aMHCII PB	BioLegend	RRID: AB_493528 Clone:M5/114.15.2
aPD1 PerCP/Cy5.5	BioLegend	RRID: AB_10550092 Clone:29F.1A12
aTCRb biotin	BioLegend	RRID: AB_313426 Clone: H57-597
aTIM3 APC	BioLegend	RRID: AB_2562997 Clone:B8.2C12
Donkey anti-rabbit IgG AF647	BioLegend	RRID: AB_2563202 Clone:Poly4064
Goat anti-mouse AF555	Invitrogen	RRID: AB_2535849
IRDye 800CW Goat anti-Rabbit	LI-COR	RRID: AB_2651127
Rat IgG1, κ Isotype Ctrl	BioLegend	RRID: AB_11150772 Clone: RTK2071
Rat IgG2a, κ Isotype Ctrl	BioLegend	RRID: AB_11147167 Clone: RTK2758
Rat IgG2b, κ Isotype Ctrl	BioLegend	RRID: AB_11149687 Clone: RTK4530
Mouse IgG1, κ Isotype Ctrl	BioLegend	RRID: AB_11148942 Clone: MG1-45
American Hamster IgG Isotype Ctrl	BioLegend	RRID: AB_11203529 Clone: HTK888

Rabbit IgG Isotype Ctrl	Thermofisher scientific	RRID: AB_243593
Anti-mouse CD16/32	BioLegend	RRID: AB_2561482 Clone: 93
CD45-BX007—Alexa Fluor™ 750-RX007	Akoya Biosciences	Cat#4450002, Clone: 30-F11
MHCII-BX014—Atto 550-RX014	Akoya Biosciences	Cat#4250003, Clone: M5/114.15.2
CD3-BX021—Cy5-RX021	Akoya Biosciences	Cat#4350014, Clone: 17A2
CD11c-BX030—Cy5-RX030	Akoya Biosciences	Cat#4350013, Clone: N418
Anti-p27 KIP 1	Abcam	RRID: AB_2811037, Clone: Y236
Anti-GFP	Abcam	RRID: AB_305643
Anti-mouse CD90.1 (Thy-1.1)	BioLegend	RRID: AB_314013 Clone: OX-7
Anti-mouse F4/80	BD Biosciences	RRID: AB_2739222 Clone: T45-2342
Anti-mouse CD366 (Tim-3)	Biolegend	RRID: AB_1626128 Clone: B8.2C12
Bacterial and Virus Strains		
One Shot™ Stbl3™ Chemically Competent *E. coli*	Thermofisher scientific	cat#C737303
Biological Samples		
anonymized TNBC patients	Brighman's and Women's Hospital Pathology core	protocols 11-104 and 93-085
Chemicals, Peptides, and Recombinant Proteins		
Iscove's Modified Dulbecco's Medium (IMDM)	Thermofisher Scientific	Cat#31980030
USDA FBS	Life Technologies	Cat#10437028
Penicillin-Streptomycin	Life technologies	Cat#15140122
Glutamax	Life Technologies	Cat#35050061
Polybrene Transfection Reagent	Thermofisher Scientific	Cat#TR1003G
T4 Ligase	NEB	Cat#M0202L
BamHI-HF	NEB	Cat## R3136L
NheI-HF	NEB	Cat#R3131S
CutSmart® Buffer	NEB	Cat#B7204
AgeI-HF	NEB	Cat#R3552S
SalI-HF	NEB	Cat#R3138S
BsaBI	NEB	Cat#R0537S
Q5® High-Fidelity DNA Polymerase	NEB	Cat#M0491S
BclI-HF	NEB	Cat#R3160S
NotI-HF	NEB	Cat#R3189S
Calcium Chloride, Anhydrous (Pellets, 4-20 mesh, for Desiccators), Fisher Chemical™	Fisher Scientific	Cat#C614-500
UltraPure 0.5 M EDTA, pH 8.0	Life Technologies	Cat#15575020
Alt-R® S.p. Cas9 Nuclease V3	IDT	Cat#1081059

Hyaluronidase	StemCell	Cat#07461
Collagenase IV	StemCell	Cat#17104019
DNaseI	Sigma Aldrich	Cat#10104159001
RBC lysis buffer	Biolegend	Cat#420301
BSA	Cell Signaling Tchnology	Cat# 9998S
Dapi	Biolegend	Cat#422801
10X CODEX Buffer	Akoya Biosciences	Cat#7000001
CODEX Assay Reagent	Akoya Biosciences	Cat#7000002
Nuclear Stain	Akoya Biosciences	Cat#7000003
CODEX Storage Buffer	Akoya Biosciences	Cat#232107
BX002—Atto 550-RX002	Akoya Biosciences	Cat#5450023
BX006—Cy5-RX006	Akoya Biosciences	Cat#5450027
BX017—Atto 550-RX017	Akoya Biosciences	Cat#5250001
BX027—Cy5-RX027	Akoya Biosciences	Cat#5350004
BX042—Cy5-RX042	Akoya Biosciences	Cat#5350008
7-AAD	Biolegend	Cat#420404
Trizol LS	Life Technologies	Cat#10296010
Trizol	Life Technologies	Cat#15596018
D(+)-SUCROSE	Fisher Scientific	Cat#AC177140010
Sodium L-Lactate >99% (NT)	Sigma Aldrich	Cat#71718-100G
SODIUM L-LACTATE (13C3, 98%)	Cambridge Isotope laboratories	#CLM-1579-N-0.1MG
PARAFORMALDEHYDE 32% SOL. EM GRADE	VWR	Cat#100496-496
16% Paraformaldehyde Aqueous Solution, EM Grade	Fisher Scientific	Cat#50-980-487
FB OCT COMPOUND CLEAR 4OZ	Fisher Scientific	Cat#23730571
Normal Mouse Serum	Jackson ImmunoResearch Laboratories	Cat#015-000-120
Avidin/Biotin Blocking System	BioLegend	Cat#927301
ProLong Diamond Antifade Mountant	Life Technologies	Cat#P36961
Doxycycline hyclate	Biogems	Cat#2431450
Poly-L-lysine solution	Sigma Aldrich	Cat# P8920-500ML
2-NBDG	VWR	Cat#76021-666
Recombinant Murine Flt3-Ligand	VWR	Cat#10780-338

Lipopolysaccharides from Escherichia coli O111:B4 γ-irradiated	Sigma Aldrich	Cat#L4391-1MG
Poly I:C	Invitrogen	Cat#tlrl-pic
Pierce RIPA Buffer	VWR	Cat#PI89900
NuPAGE Sample Reducing Agent	Life Technologies	Cat#NP0009
Novex 4-20% Tris-Glycine gels	Life Technologies	Cat#P04205BOX
Nitrocellulose Sandwiches	Cell Signaling Technology	Cat#12369P2
Critical Commercial Assays		
QIAprep Spin Miniprep Kit	Qiagen	Cat#27106
EndoFree Plasmid Maxi Kit	Qiagen	Cat#12362
miRNeasy Micro Kit	Qiagen	Cat#217084
SF Cell Line 4D-NucleofectorTM X Kit S	Lonza	Cat#V4XC-2032
EasySep™ Mouse CD8+ T Cell Isolation Kit	StemCell	Cat#19853
QIAquick PCR Purification Kit	Qiagen	Cat#28104
QIAquick Gel Extraction Kit	Qiagen	Cat#28706
Hypoxyprobe-Biotin Kit	Hypoxyrpobe	Cat#HP10-1000kit
EdU-Click 647	BaseClick	Cat#BCK-EdU647
CODEX Staining Kit	Akoya Biosciences	Cat#7000008
CODEX Conjugation Kit	Akoya Biosciences	Cat#7000009
EasySep™ Mouse Pan-DC Enrichment Kit	STEMCELL	Cat#19763
Deposited Data		
Sequencing datasets	This paper	Available at NCBI accession # GSE198715
Experimental Models: Cell Lines		
4T07	Dr. Robert Weinberg, MIT	N/A
D2A1	Dr. Robert Weinberg, MIT	N/A
EMT6	ATCC	Cat#CRL-2755™
Hek293:Lenti-X™ 293T Cell Line	Takara	Cat#632180
B16F10	Dr. Brian Brown	N/A
Experimental Models: Organisms/Strains		
Mouse: Balb/c :BALB/cJ	The Jackson Laboratory	Strain #:000651
Mouse: NSG: NOD.Cg-Prkdc^{scid} Il2rg^{tm1Wjl}/SzJ	The Jackson Laboratory	Strain #:005557
Mouse: Jedi: Ptprc^{a} Tcrb^{Ln1Bdb} Tcra^{Ln1Bdb} H2^{d}/J	Dr. Brian Brown laboratory, Mount Sinai	N/A
Mouse:PD1-/-:B6.Cg-Pdcd1tm1.1Shr/J	The Jackson Laboratory	Strain #:028276

Mouse:B6:C57BL/6J	The Jackson Laboratory	Strain #:000664
Mouse:Kaede:Kaede	Dr. Osami Kanagawa, Univeristy of Lyon	N/A
Mouse:B6.129-Hif1a^{tm3Rsjo}/J	The Jackson Laboratory	Strain #:007561
Mouse:B6.Cg-Zbtb46$^{tm3.1(cre)Mnz}$/J	The Jackson Laboratory	Strain #:028538
Oligonucleotides		
Alt-R® CRISPR-Cas9 tracrRNA	IDT	Cat#1072533
Hif1a gRNA: AGTGCACCCTAACAAGCCGG	IDT	Alt-R® CRISPR-Cas9 crRNA
Ifnar1 gRNA: GCTCGCTGTCGTGGGCGCGG	IDT	Alt-R® CRISPR-Cas9 crRNA
Recombinant DNA		
3rd Generation Lentiviral packaging vectors	Dr. Brian Brown, Mount Sinai	N/A
PGK:eGFP Lentiviral vector	Dr. Brian Brown, Mount Sinai	N/A
mVenus:p27k reporter	Dr. Toshio Kitamura, University of Tokyo	N/A
PGK:mCherry Lentiviral vector	Dr. Brian Brown, Mount Sinai	N/A
H2B-mCherry	Addgene	Cat#51007
H2B-tdTomato	Addgene	Cat#58101
rtTA	Addgene	Cat#104543
TetON lentiviral expression vector	Addgene	Cat#131687
Hif1a STBL: mHif-1α MYC (P402A/P577A/N813A)	Addgene	Cat#44028
Software and Algorithms		
FlowJo 10	BD	https://www.flowjo.com
Prism 9	GraphPad	https://www.graphpad.com/scientific-software/prism/
FiJi® (v2.0.0-rc-69/1.52i)	ImageJ	https://imagej.net/software/fiji/
Seurat	Satija Lab	https://satijalab.org/seurat/articles/pbmc3k_tutorial.html
DESeq2	Bioconductor	https://bioconductor.org/packages/release/bioc/html/DESeq2.html
Akoya CODEX Processor®	Akoya	https://www.akoyabio.com/phenocycler/software/
clusterProfiler	Bioconductor	https://bioconductor.org/packages/release/bioc/html/clusterProfiler.html
bigSCale2	Iacono, G., *et al,* 2019	https://github.com/iaconogi/bigSCale2
Benchling	Benchling	ttps://www.benchling.com
Biorender	Biorender	https://biorender.com/
Other		
Compresstome®	Precisionary	VF-310-0Z

Experimental model and subject details

Mice

Two-month-old BALB/cJ females (Stock No. 000651) from Jackson Laboratories were used for all experiments as tumor-bearing mice, unless otherwise stated. NOD.Cg-Prkdc^{scid} Il2rg^{tm1Wjl}/SzJ a.k.a. NSG mice (Stock No. 005557 from Jackson Labs) were used as non-T cell bearing controls. Just EGFP Death Inducing (Jedi) mice (Ptprc^{a} Tcrb^{Ln1Bdb} Tcra^{Ln1Bdb} H2^{d}/J) (29) in BALB/cJ background were obtained from Dr. Brian Brown. These Jedi mice were bred with PD1$^{-/-}$ mice (B6.Cg-Pdcd1tm1.1Shr/J, Stock No. 028276, from Jackson Labs) to generate PD1$^{-/-}$ Jedi, ensuring the H2-Kd haplotype and CD45.1 congenital marker were also selected. F1 from BALB/cJ crossed with C57BL/6J mice (Stock No. 000664 from Jackson Labs) were used for tumor implantation in experiments using PD1$^{-/-}$ Jedi T cells adoptive transfer. Kaede mice were previously reported (85) and provided by Dr. Osami Kanagawa at RIKEN, Japan. Kaede mice were crossed with BALB/cJ one generation for injection of 4T07 breast cancer cells for tumor formation. To obtain animals with Hif1a deficiency in cDC we crossed Zbtb46Cre animals (Stock No. 028538 from Jackson Labs) that have Cre expression restricted to cDC population with Hif1a floxed animals (Stock No. 007561 from Jackson Labs). Zbtb46Cre$^{+/-}$ Hif1a$^{fl/fl}$ animals were obtained and Zbtb46Cre$^{-/-}$ Hif1a$^{fl/fl}$ liter mates were used as controls. All animal procedures were approved by Dana-Farber Cancer Institute IACUC and the Harvard Medical School IACUC and performed according to DFCI protocol #17-017 and HMS protocol # IS00002540. The study is compliant with all relevant ethical regulations regarding animal research.

Cell lines

4T07 and D2A1 breast cancer cell lines were a gift from Dr. Robert Weinberg. B16F10 melanoma cells were a gift from Dr. Brian Brown. EMT6 breast cancer cells were purchased from ATCC. HEK293T cells were purchased from Takara. All cell lines were cultured in Iscove's Modified Dulbecco's Medium (IMDM), 10% heat inactivated FBS

(Gibco), 1% Penicillin-Streptomycin (Gibco) and 1% Glutamax (Gibco). 4T07, EMT6 and D2A1 cells were engineered to express the desired fluorescent proteins and markers by stable transduction with lentiviral vectors (LV). All cells were tested for mycoplasma prior to injection.

GFP and mCherry-expressing 4T07 cells used in Figure 1 were subjected to RNA-sequencing analysis to ensure no bias had occurred during generation of the cell lines. This analysis revealed no differences between the cell lines.

Human FFPE samples and Bulk RNAseq data

This study was performed in accordance with the guidelines of ethical regulation for human samples under approved protocols 11-104 and 93-085 at Dana Farber Cancer Institute.

Sections from Formalin-Fixed Paraffin Embedded (FFPE) Primary Triple Negative Breast Cancer from treatment naïve unidentified patients were obtained from the Brigham and Women's Hospital Pathology core.

Bulk RNAseq data cohort was formed by 29 patients with confirmed mTNBC defined as <1% progesterone receptor, <1% estrogen receptor and HER2 negative by ASCO/CAP guidelines on a metastatic biopsy. Patient regimens: treated with an ICB alone (pembrolizumab, n = 6, NCT02447003; atezolizumab, n = 4, NCT01375842) or as part of a combination regimen with chemotherapy (pembrolizumab + eribulin, n = 8, NCT02513472; atezolizumab + nab-paclitaxel, n = 5, NCT0163970) or a targeted therapy (nivolumab + cabozantinib, n = 6, NCT03316586). Samples were sequenced before ICB treatment. PFS was defined as the date of starting immunotherapy to the date of progression, death, or last follow-up. Durable responders were considered as free of disease progression at time of analysis (5 patients) with a PFS of 26-60 months.

Plasmids

Third generation lentiviral packaging and lentiviral vector (LV) backbone with eGFP expression under PGK promoter were a gift from Dr. Brian Brown (157). The mVenus-p27K insert sequence was a gift from Dr. Kitamura (131). Fluorescent protein sequences were obtained from the following vectors: mCherry (Dr. Brian Brown gift), H2B-mCherry (Addgene #51007) and H2B-tdTomato (Addgene #58101). The eGFP lentiviral plasmid was used as backbone to generate vectors expressing mCherry, H2B-mCherry, mVenus-p27K, tdTomato-p27K and a shuttle vector for co-expressing two proteins with Internal Ribosome Entry Site (IRES) element by PCR, digestion by BamHI and SalI restriction enzymes and T4 DNA Ligase.

The mVenus fluorescent protein (yellow) was replaced by tdTomato by PCR from H2B-tdTomato and using BamHI and BsaBI restriction enzymes to make a tdTomato-p27k fusion protein in red color. Same strategy was used to create a fusion protein with rtTA-p27K for the genetic circuit in Figure 1O. The rtTA sequence was obtained from Addgene #104543. The doxycycline expression vector was obtained from Addgene #131687 in which H2B-tdTomato fluorescent protein was introduced using BclI and NotI.

The fluorescent proteins mCherry or eGFP were cloned into the same third generation LV backbone with a normoxia-stable form of HIF1a, mHif-1α MYC (P402A/P577A/N813A) (Addgene #44028), here referred as HIF1a^{STBL}. The resulting vectors had therefore the following structure mCherry-IRES-HIF1a^{STBL} and GFP-IRES-HIF1a^{STBL}. DNA was extracted by miniprep or maxiprep kits (QIAGEN) after transformation in Stbl3 E.coli (ThermoFisher). All plasmids were verified by Sanger sequencing.

Methos details

Tumor injection

Breast tumors were induced by intra-mammary fat pad injection of indicated breast cancer cell lines (4T07, EMT6 and D2A1). The injections were performed after introducing a 2mm

incision to visualize the 4th mammary fat pad under isoflurane anesthesia. A total of 250,000 cells in 50µL sterile PBS were injected in the fat pad of the mammary gland. Local analgesic was used for pain relieve. Tumors were measured with a caliper and monitored twice a week and tumor volume was calculated as (length*width*width)/2.

Lentiviral production and transduction

Third generation lentivirus were produced by $Ca_3(PO_4)_2$ transfection into HEK293T cells (157). Supernatants were collected, passed through a 0.22μm filter, aliquoted and frozen, or directly used to transduce breast cancer cell lines.

For LV transduction, tumor cells were cultured with filtered LV in the presence of 1:2000 Polybrene Transfection Reagent (Millipore) for 16-24 hours, expanded, and subsequently FACS-sorted with Aria III cell sorter (BD Biosciences) using the expressed fluorescent reporter. All transgenes introduced by LV transduction were expressed under the ubiquitous promoter PGK.

Generation of knockout cell lines

Amaxa 4D-Nucleofector X Unit device (Lonza) was used to generate knockout cells lines through CRISPR/Cas9-mediated genome editing. Briefly, 2.5µL 200µM trRNA, 2.5µL 200µM gRNA and 5µL 20µM recombinant CAS9 (Integrated DNA Technologies) were mixed to make Cas9/gRNA ribonucleoprotein (RNP). The RNP was delivered into tumor cell lines using program A549 by SF Cell Line 4D-NucleofectorTM X Kit S (Lonza). 200,000 cells were used per reaction and recovered in 6-well plate for 4 days after nucleofection, and then subjected to a 2nd round of the same process. The efficiency of Ifnar1-/- was validated by flow cytometry analysis. *Hif1a*-/- cells were validated by western blot using HIF-1a (D1S7W) rabbit antibody from Cell Signaling Technology. The guide RNA sequences were: HIF1a (AGTGCACCCTAACAAGCCGG), Ifnar1 (GCTCGCTGTCGTGGGCGCGG).

Adoptive transfer of CD8+ T cells

Jedi CD8+ T cells as well as PD1$^{-/-}$ Jedi CD8+ T cells were purified from spleens and lymph nodes (LNs) after obtaining a single cell suspension by mechanical disruption and filtering through a 70µm cell strainer. CD8+ T cells were selected with the mouse CD8+ T cells isolation kit (STEMCELL) following manufacturer's instruction. 5-7×10^6 T cells (unless stated otherwise) were injected via tail vein per mouse in 200µL sterile PBS.

Flow cytometry and FACS-sorting

Tumors were collected and placed in 500µL of digestion solution (400U/mL CollagenaseIV, 6.8U/mL Hyaluronidase, 20μg/mL DNaseI and 10%FBS in HBSS). After mincing, they were transferred to a 10mL tube with 5mL digestion solution and incubated at 37 °C for 20 minutes on a rotator. Digested samples were then filtered through a 100μm cell strainer followed by red blood cell (RBC) lysis (Biolegend) for 5 minutes at room temperature (RT). Single cell suspensions were blocked with 1:100 dilution of TruStain FcX (#101319 Biolegend) in flow buffer (2mM EDTA 0.1% BSA PBS). Samples were then stained with the appropriate antibodies. DAPI (1:10,000) or 7AAD (1:100) were used as viability markers. Samples were analyzed by CytoFLEX (Beckman). Cells were FACS-sorted by Aria III cell sorter (BD Biosciences) and collected in 15mL tubes with 5mL of media. Data were analyzed using FlowJo v.10 software.

Bulk RNA-sequencing

GFP+ and mCherry+ 4T07 cells in Figure 1 were directly FACS-sorted into TRIzol LS (Invitrogen) and submitted directly for RNA extraction and low-input RNA-sequencing to GENEWIZ. FACS-sorted mVenusp27K^{High} and mVenus-p27K^{Neg} 4T07, EMT6 and D2A1 cells from primary tumors were collected in media, centrifuged, and resuspended in 1mL TRIzol (Invitrogen). RNA was extracted with miRNeasy Micro kit (QIAGEN) following the

manufacturer's instructions. RNA samples were submitted to GENEWIZ for bulk RNA-sequencing.

Immunofluorescence

Tumors were harvested and fixed in 20% Sucrose 4% Paraformaldehyde (PFA) solution in PBS overnight at 4°C. They were then embedded in OCT compound (Fisher Health Care) and stored in -80°C. Sections (10µm) were blocked in 10% Fetal Bovine Serum, 2% Normal Mouse Serum, 0.1% Tween-20 TBS for 1 hour at RT and incubated for 3 hours at RT or overnight at 4°C with primary antibodies. Tissue was washed and, when needed, incubated with secondary fluorescently labelled antibodies for 2 hours before nuclear staining with DAPI (ThermoFisher). For Nuclear marker Ki67, samples were permeabilized with 1% TritonX-100 at 37 °C for 30min prior to staining. For biotin antibodies, an extra blocking step was done with Avidin/Biotin Blocking System (Biolegend) following the instruction of the Kit. Antibodies were used at 1:100 dilution in blocking buffer. The stained tissue was then mounted on ProLong™ Diamond Antifade Mountant (Invitrogen) and covered with a #1.5 coverslip.

For assessment of tumor hypoxia, Pimonidazole (75mg/Kg of body weight) was intraperitoneally injected 30-60min prior to euthanasia. Staining was performed with Hypoxyprobe® following manufacturer instructions.

Microscopy methods

Microscopy methods are reported following the guidance of (158).

Images for Figures 21A, 29 (4T07), 38A were acquired in Yokogawa CSU-W1 single disk (50 μm pinhole size) spinning disk confocal unit attached to a fully motorized Nikon Ti inverted microscope equipped with a Nikon linear-encoded motorized stage with a PI 250 □m range Z piezo insert, an Andor Zyla 4.2 plus (6.5 μm photodiode size) sCMOS camera using a Nikon Plan Apo 20x/0.75 NA DIC air objective. The final

digital resolution of the image was 0.325 μm/pixel. Fluorescence from mVenus, Alexa Fluor 555 (or mCherry) and Alexa Fluor 647 was collected by illuminating the sample with solid-state directly modulated 488 nm diode 100 mW (at the fiber tip) laser line, a solid state, directly modulated 561 nm DPSS 100mW (laser tip) laser line or a solid state, directly modulated 640 nm diode 100mW (laser tip) laser line in a Toptica iChrome MLE laser launch, respectively. A hard-coated Semrock Di01-T405/488/568/647 multi-bandpass dichroic mirror was used for all channels. Signal from each channel was acquired sequentially with either a hard-coated Chroma ET525/36 nm, Chroma ET605/52 nm or Chroma ET705/72m emission filters in a filter wheel placed within the scan unit, for mVenus, Alexa Fluor 555 (or mCherry) and Alexa Fluor 647 channels, respectively. Fluorescence from DAPI was collected by illuminating the sample with a Lumencore SOLA 395 LED based light engine using a Chroma 49000 filter cube. Nikon Elements AR 5.02 acquisition software was used to acquire the data. Data was saved as ND2 files.

Images for Figures 21C, 22, 27, 29 (EMT6, D2A1), 30, 31A,B, 65 were acquired using a motorized Nikon Ti inverted widefield microscope equipped with a SOLA SE LED light engine, Prior ProScan II linear encoded motorized stage, a Shutter Instruments Lambda 10-3 motorized excitation filter wheel, a LUDL MAC3000 motorized emission filter wheel located in front of the camera on the side port. A Hamamatsu Orca Flash 4.0 v3, 6.5 μm photodiode size sCMOS camera was used for detection. Images were acquired using a Nikon Plan Apo 20x/075 Ph2 air objective lens. Final digital resolution of the image was 0.325 μm/pixel. Signal from DAPI, FITC, RED, FAR RED was collected by illuminating the sample with a hard-coated Chroma AT350/50x, Chroma ET490/20X, Chroma ET555/25x and Chroma ET 645/30x excitation filter, a hard-coated Chroma ET 69002bs multiband dichroic DAPI/FITC/TRITC/Cy5 and a Chroma ET455/50m, Chroma ET525/50m, Chroma ET605/52M, Chroma ET700/75m emission filter, respectively. Images from each experiment were collected under identical imaging conditions using Nikon Elements 5.2 AR acquisition software and a 12-bit low gain digitizer. Images were saved as ND2 files.

Images for Figures 15, 17, 20, 31C, 32, 38B, 39, 75 were acquired using a motorized Zeiss Axio Observer 7 inverted microscope equipped with a LED Colibri 7 fluorescence light source, and motorized scanning stage with a Z-piezo insert of 500 μm range. A Photometrics Prime BSI sCMOS 6.5 um photodiode size was used for detection. Images were acquired using a Zeiss 20x Plan Apo 20x/0.8 DICII air or a Zeiss Plan Apo 63x/1.4 DICII oil objective lens with Zeiss 518F immersion oil; the final digital resolution of the image was 0.325 μm/pixel or 0.1 μm/pixel, respectively. Signal from DAPI, GFP/mVenus, Alexa Fluor 555, mCherry, Alexa Fluor 647 and Alexa Fluor 750, was collected by illuminating the sample with a Zeiss 90 HE DAPI/GFP/Cy3/Cy5 multi-band pass filter cube or a Zeiss 110 HE DAPI/GFP/Cy3.5/Cy7 multi-band-pass filter cube. Images were collected using Zen Blue (Zen 2.6 Pro) acquisition software and saved as *.czi* files.

In images for Figures 38A and 6H tile scans of the whole tumor section were collected with a 10% of overlap between each tile and stitched automatically in the acquisition software using the "blending algorithm", using the DAPI signal as the reference channel.

Evaluation of cell cycle

To evaluate cell proliferation *in vivo*, animals were injected intraperitoneally with 10mg/Kg of EdU (5-ethynyl-2'-deoxyuridine) daily during the last 5-8 days of tumor growth. Tumors were harvested and processed for immunofluorescence staining as described above. EdU was stained using the immunofluorescence BCK-EdU647 staining kit (BaseClick) following manufacturer's instructions.

Evaluation of cell cycle state prior to adoptive transfer of Jedi T cells was performed using a genetic circuit as explained in Figure 1O. 4T07 cells carrying both GFP and the genetic circuit were injected in the mammary fat pad. Animals received one intraperitoneal injection of Doxycycline (50mg/kg diluted in sterile PBS) 30h prior to adoptive transfer of Jedi T cells to ensure doxycycline had been eliminated from the system (159) (160). 5

million Jedi T cells were injected on day 6 of tumor growth. H2B-tdTomato+ tumor cells were quantified by flow cytometry on day 12 of tumor growth.

Tumor initiation assay

To test the tumor initiation potential of Jedi-resistant cancer cells: GFP or mCherry-expressing 4T07 cells were mixed 1:1 ratio and injected into the mammary fat pad of BALB/c mice. 7 days after tumor inoculation 5M of Jedi T cells were adoptively transfer. In parallel, double transduced tdTomato-p27K and GFP-expressing 4T07 were injected into mammary fat pad of NSG mice as controls with no T cell killing. 14 days after tumor inoculation tumors from both groups were processed and surviving GFP+ cells were FACS-sorted. 500 live (DAPI-) were injected into mammary fat pad of new BALB/c mice.

To test the tumor initiation potential of $p27K^{High}$ cells: mCherry and mVenus-p27K expressing breast tumors (4T07, D2A1 or EMT6) were processed to obtain single cell suspensions by collagenase digestion. mCherry+ mVenus–$p27K^{Neg}$ and mCherry+ mVenus-$p27K^{High}$ cells were FACS-sorted. Tumor initiation potential was assessed by injecting 500 live (DAPI-) cells (for EMT6) and 1,000 cells (4T07 and D2A1) into mammary fat pad of new BALB/c mice.

Glucose uptake

Tumor single cell suspensions were resuspended in 200μM 2NBDG (BioVision) in flow buffer for 20 min at 37 °C, using equivalent number of cells across tumors. Samples were then analyzed by flow cytometry.

Photo-conversion of Areas to Dissect Micro-Environments (PADME-seq)

Step by step description of the protocol is described in Annexes I of this thesis work. tdTomato-p27K-expressing 4T07 cells were injected into the mammary fat pad of Kaede

x BALB/c F1 females. Tumors were embedded in 2% low melting agarose and cut into 300µm slices by the Compresstome VF 310-0Z vibrating microtome (Precisionary Instruments). Setting of the machine were 3 for vibration and 1-2 for speed depending on tumor consistency. Tumors were sectioned to obtain 2 consecutive slices together from 2 depths/regions from each tumor mass. Consecutive slices were used to photoconvert cells infiltrating tdTomato-negative areas and then cells in regions with tdTomato-p27K^{High} cells. Slices were kept in a 12 well plate with IMDM media on ice. Photoconversion was performed in a Zeiss LSM710 single point-scanning confocal unit with galvanometer mirrors attached to a fully motorized Axio-Observer Z1 equipped with a Zeiss motorized stage using a Zeiss Plan Apochromat 20x/0.8 NA DIC air objective. Photoconversion of Kaede was performed using a 405nm 30mW diode AOTF modulated line set to 0.2 % transmittance laser and a time series of 325 cycles at a 1.58µsec/pixel pixel dwell times, using a 405 long-pass dichroic mirror. Kaede green and red (after photoconversion) fluorescence was collected by illuminating the sample with an argon multi-line 488 nm 25 mW Argon AOTF modulated line set to 0.2 % transmittance and a 561 nm 20mW DPSS AOTF modulated line set to 0.2 % transmittance, using a multi-bandpass dichroic mirror with 488/561cut off wavelengths (MBS 488/561). The emission wavelength range for the green and red fluorescence signal was set to 499-560 nm and 571-735 and collected by multi-alkali PMTs. No offset was applied. The microscope was controlled by ZEN Black SP2 acquisition software, scanned unidirectionally with a pixel dwell time of 1.58µsec/pixel, no averaging, a 12-bit digitizer, zoom 1.0x, a pixel size of 0.83 µm and pinhole set to 1 A.U. for 488 nm wavelength. Images were saved with the .czi file format.

Photoconverted slices were digested in collagenase IV + DNase I as described above. Samples were digested for 15 min at 37°C and pass through a 100µm cell strainer followed by RBC lysis. Cells were washed and resuspended in 1mL flow buffer with DAPI (1:10,000) for sorting. Green/red double positive live cells were considered as the successful photoconverted ones and FACS-sorted into 1.5mL Eppendorf tubes with 500µL media at AriaIII.

Co-detection by indexing (CODEX) tissue staining.

mCherry from the original Figure 1 setting was replaced by Thy1.1 as a tumor marker. The CODEX technology requires three spectrally distinct dyes (Atto 550, Cy5, Alexa Fluor™ 750) for each imaging cycle and Atto550 overlaps with mCherry. Thy1.1 was not immunogenic in BALB/c mice and antibody in the panel was used to detect Thy1.1 (as the non-GFP cancer cells). Wildtype (untransduced) or Thy1.1:GFP-expressing mixed 4T07 tumors were harvested and dehydrated in 20% sucrose in PBS overnight at 4°C. Tumors were then embedded in OCT compound and stored in -80°C. Sections (8µm) were obtained onto poly-L-lysine-coated coverslips and blocked for 1h at RT in Akoya CODEX Blocking Buffer® with IgG isotype controls and anti-mouse Fc receptors (93, Biolegend #101330). Then tissues were stained overnight at 4°C with the oligonucleotides-barcoded primary antibody cocktail (Table 3), which were prepared following Akoya Biosciences CODEX Fresh-Frozen Tissue Staining protocol. The following primary antibodies were purchased from Akoya Biosciences: CD45, MHCII, CD3, CD11c. The rest primary antibodies were conjugated to Akoya barcodes according to Akoya Biosciences CODEX Antibody Conjugation protocol: p27, GFP, Thy1.1, F4/80, TIM3. Secondary fluorophore-tagged oligonucleotides (reporters) and DAPI (Akoya #7000003) were automatically added and washed away for each imaging cycle using Akoya CODEX system to allow multiplexed visualization on a single tissue section. Images (Figure 4L, S4F, 5G) were acquired using a motorized Zeiss Axio Observer 7 inverted microscope equipped with a LED Colibri 7 fluorescence light source, and motorized scanning stage with a Z-piezo insert of 500 μm range. A Photometrics Prime BSI sCMOS 6.5 um photodiode size was used for detection. Images were acquired using a Zeiss 20x Plan Apo 20x/0.8 DICII air; the final digital resolution of the image was 0.325 μm/pixel. Signal from DAPI, Atto 550, Cy5 and Alexa Fluor™ 750, was collected by illuminating the sample with a Zeiss 90 HE DAPI/GFP/Cy3/Cy5 multi-band pass filter cube or a Zeiss 110 HE DAPI/GFP/Cy3.5/Cy7 multi-band-pass filter cube. Images were collected using Zen Blue (Zen 2.6 Pro) acquisition software and saved as *.czi* files.

Analysis was done using CODEX Multiplex Analysis Viewer CODEXMAV (v1.5.0.8) plugin in Fiji (v2.1.0/1.53c).

Bone marrow derived dendritic cell (BM-DC) generation and culture in different oxygen concentrations.

BM-DCs were generated using Flt3l as already described in (141). At day 9 BMDC were recovered with flow buffer 10mM EDTA and 90,000 live cells/well were seeded in a 96 well U bottom plate. Cells were conditioned for 2 hours to the required oxygen level (normoxia, 5% or 1%O2). Then either LPS (50ng/ml) or PolyI:C (5μg/ml) was added. Cells were kept with either LPS or PolyI:C for 18h at the corresponding oxygen level (so total 20h). Cells were detached with flow buffer 10mM EDTA and processed for flow cytometry assay.

Western blot

Whole cell lysate (WCL) was collected from 1 million WT or *Hif1a*-/- cells using RIPA buffer (Cell Signaling Technology, CST) with Pierce Protease Inhibitor (Thermo Fisher Scientific). After incubating for 10 min on ice, WCL was spined for 15 min at 13,000 rpm at 4°C to get the supernatant. 3X loading buffer with DTT (CST) was added and boiled at 100°C for 5 min to denature. Protein samples were separated by Novex 4-20% Tris-Glycine gels (Invitrogen) and transferred to nitrocellulose membranes (Cell Signaling Technology, CST). The membranes were blocked by 5% milk TBST (0.1% Tween 20), then incubated with rabbit anti-HIF1A (D1S7W, 1:1000, CST) and mouse anti-Actin (8H10D10, 1: 5000, CST) overnight at 4°C. Followed by washing use TBST for 3 times, the membranes were incubated with AF555 Goat anti-mouse (1:5000,Invitrogen) and IRDye 800CW Goat anti-Rabbit (1:5000, LI-COR Biosciences) fluorescent secondary antibodies for 2 hours at room temperature. The membranes were imaged using Bio-Rad ChemiDoc MP Imaging System.

scRNA-seq

mCherry+ 4T07 tumors either WT, Hif1a KO or HIF1a STBL were processed and FACS sorted for Dapi- following above instructions. Cells were sorted into conditioned media and then washed in PBS 0.01% ultrapure BSA. Cells were counted and resuspended to obtain a 1K/μL dilution. A target population of 10K ells were submitted for 10x processing at the single cell genomics core of Dana Farber - Broad Institute.

Lactate quantification by mass spectrometry

About 50mg of mCherry+ 4T07 tumors either WT, Hif1a KO or HIF1a STBL were snap freeze in liquid nitrogen. Samples were submitted to the metabolomics sore at Dana Farber for ethanol extraction. Lactate quantification was performed by relative quantification using labbeled 13C L-Lactate as internal control.

Splenic cDC isolation

cDC were purified from spleens and lymph nodes (LNs) after obtaining a single cell suspension by mechanical disruption and filtering through a 70µm cell strainer. cDC cells were selected with the mouse EasySep™ Mouse Pan-DC Enrichment Kit (STEMCELL) following manufacturer's instruction. 300K cDC cells were cultured in 200μL of media +/- L-sodium lactate addition at the specified concentration.

Quantification and statistical analysis

Computational analysis of immunofluorescent images of mouse tumors

All images were analyzed using FiJi® (v2.0.0-rc-69/1.52i) (161).

Colocalization analysis for nuclear markers (Ki67, mVenus-p27K and EdU) was done using DAPI channel for segmentation with the Trainable Weka Segmentation (v3.2.29)

plugin. Nuclear particles were converted into a binary mask to analyze the fluorescent intensity in the different channels with the function Analyze Particles. Intensities of the different channels in the same particle were plotted to assess correlation or exclusion patterns.

T cell density per area was analyzed in tumors from Figures 15 and 29 after CD3 staining. Areas were drawn using mVenus-p27K, GFP or mCherry and blindly to CD3 signal. After drawing the regions of interest (ROIs), CD3 signal was revealed, and T cells were counted manually. Area was calculated by FiJi after scaling images. Density of T cells was calculated as number of T cells/area (mm^2).

Images from H2B-mCherry and mVenus-p27K expressing tumors that had been stained with CD3 were processed with FiJi (v2.0.0-rc-69/1.52i). DAPI channel was used for segmentation using the Trainable Weka Segmentation (v3.2.29) plugin. The generated mask was used to measure the mean intensity in each cell of H2B-mCherry, mVenus-p27K and CD3. A computational reconstruction of every image was obtained using the mean intensity values for each channel. To assess CD3 exclusion the distribution of mVenus-p27KHigh cells was randomized among H2B-mCherry+ cells. The average distance from a CD3 cell to the 10 closest mVenus-p27KHigh cells was measured in the real and in the random distribution and then plotted and analyzed with the Kolmogorov-Smirnoff statistic.

Quantification of MHCII fluorescent intensity in DCs (Figure 5G) was performed on immunofluorescence images with CD11c and MHCII staining on mVenus-p27K-expressing 4T07 breast tumors. ROIs were drawn using only mVenus-p27K, being blind to both CD11c and MHCII. Afterwards, CD11c channel was used to create a binary mask after thresholding with Otsu method. Fluorescent intensity of the MHCII channel was measured using Analyze Particles function using particles generated by the CD11c mask.

Analysis of immunofluorescent FFPE sections from human TNBC

FFPE sample slides from 10 anonymized TNBC patients were stained by the BWH Pathology Core with E-Cadherin (24E10, CST), p27K (57/Kip1/p27, BD), Ki67 (SP6, Biocare) and CD3 (F7.2.38, Agilent). Samples were imaged with Zeiss Axio Observer 7 inverted microscope as explained in the immunofluorescence method section. For T cell enrichment analysis areas surrounding T cells that were able to infiltrate E-Cadherin+ areas were drawn and then evaluated for Ki67 or p27 positive cells. Total number of positive cells were normalized by area to obtain density of p27+ and Ki67+ cells in the vicinity of T cells.

Mouse Bulk RNAseq analysis

GENEWIZ performed basic computational analysis for quality controls and constructed the gene matrices. Gene matrices were normalized using DESeq2 size factors and filtering for a minimum of 10 read per condition (60-80 rowSums). The resulting genes with adjusted p-Value <0.05 were considered significant for GO term enrichment analysis at https://david.ncifcrf.gov/. Log2 fold change ≥ 0.5 was considered as upregulated and ≤ -0.5 as downregulated genes. Volcano plots were generated with the package EnhancedVolcano from Bioconductor. Heatmaps were generated in excel using Z-score across different samples in a given gene after after counts per million mapped reads (CPM) normalization.

CODEX image processing and analysis.

Raw images were processed using Akoya CODEX Processor® for background subtraction, deconvolution, extended depth of field and shading correction. CODEXMAV plugin in ImageJ was used for visualization and selection of cell populations. To assess T cell exhaustion, p27 positive versus negative areas or Thy1.1+ versus GFP+ areas in tumor images were drawn and then evaluated for TIM3 expression on T cells (CD45+ CD3+ MHCII- CD11c- F4/80-). To assess DC function, same selected areas were used.

DCs were considered as CD45+CD11c+F4/80-CD3-. MHCII intensities were recorded for each DC. T cells were normalized dividing the total number of T cells by the area (μm^2) of the ROI. MHCII intensities from DC were normalized and centered using a Z-score to be able to pool the different experiments eliminating the batch effect.

RNA-seq analysis from TNBC patient cohort

RNAseq data was aligned using the STAR software (162). Further transcript per million (TPM) quantification was performed using RSEM (163). Canonical pathways compiled in MSigDB from pathway databases, namely the C2 CP gene sets, were used for gene set enrichment analysis (GSEA) analysis using 1000 permutations by phenotype (164).

PADME-seq and murine scRNA-seq 10X genomics and analysis

Count matrix generation

FACS-sorted live cells were submitted to the Bigham and Women's Hospital Single Cell Genomics Core for 10x genomics. Samples from different areas were tagged using hashed antibodies and then pooled to reduce technical variability in the preparation of the 10X library following an approved protocol from the core (Table 2). The BWH Single Cell Genomics Core performed basic computational analysis using Cell Ranger pipeline and provided us the filtered matrix of read counts per gene in each cell.

Table 2. PADMEseq library preparation information.

Sample ID	Library ID	Hashing antibody	Input cell number
Tumor 1 p27K+ area	BRI-703	Mouse hashing antibody 7	7K
Tumor 1 p27K- area	BRI-703	Mouse hashing antibody 8	7K

Tumor 2 p27K+ area	BRI-705	Mouse hashing antibody 9	5.6K
Tumor 2 p27K- area	BRI-705	Mouse hashing antibody 10	7.1K

Filtering, normalization, clustering and UMAP generation

Seurat v4.0.3 package (165) for R was used to analyze the scRNAseq-seq data. Following Seurat-guided clustering tutorial (Source: vignettes/pbmc3k_ tutorial.Rmd), cells were filtered using <15% of mitochondrial genes reads to eliminate dead cells. We distinguish unique hashtags from each cell by excluding the cells that have > 250 read count in both hashtags. We excluded cells outlier to the 200-25000 read count (nCount RNA) to eliminate doublets and debris. Having filtered our data, we normalized, scaled and log-transformed the matrix (NormalizeData function) and then we centered the mean to 0 and the variance to 1 (ScaleData function) without regressing out variables.

Next, we performed a linear dimensional reduction by PCA using the top 2,000 most variable genes (FindVariableFeatures using the vst method and a span of 0.3). Based on an elbow plot (function ElbowPlot) we selected 30 PCs to calculate the shared nearest neighbor graph based on the calculated Euclidean distance (FindNeighbors function) and clustered our data using the Louvain algorithm (166) with a resolution of 0.5, with the Seurat function FindClusters (167) (168) (169) (170). Clustered data was displayed using the UMAP dimensional reduction (RunUMAP function, (171)). Clusters were identified using well known markers for immune populations and fibroblasts as described in the Figure 4C, S4A,E,H, S5A,B.

Cells from the T cell cluster were subjected to another round of unsupervised clustering as described above, except 10 PCs were used, to find further differences among QCC and non-QCC areas.

Differential expression analysis

Differential expression analysis was performed using the Seurat function FindMarkers. Genes were pre-filtered for a minimum log fold change of 0.25 and detectable expression in at least 10% of cells in the cluster, then compared for differential expression using DESeq2 (170). Genes with an FDR-adjusted p-value less than 0.1 were selected as input for gene-set enrichment analysis using GO biological processes as implemented in the clusterProfiler package from Bioconductor (172), using a set size between 3 and 800 genes and an FDR-adjusted p-value cutoff of 0.05. Relevant genes were curated from the GSEA to generate heatmaps. Average gene expression for each tumor and area was generated using AverageExpression.

Heatmaps from Figures 49 and 57 were generated with the individual cell values and the top 10 differentially expressed genes per cluster. Heatmaps with specific genes selected from the differential analysis between QCC and non-QCC areas and selected signatures among the same cluster were generated using the average value of cells coming from the same tumor and area with the function AverageExpression.

Cell abundance comparisons

We performed a Fisher's exact test for each cell type between the two different groups followed by Benjamini-Hochberg (BH) correction to obtain adjusted p value.

Co-expression gene network construction and analysis in CD8 T cells

To understand differences in the regulation of CD8+ T cells, we generated a co-expression gene network. Because of the zero-inflated and highly noisy nature of single-cell transcriptome data, we inferred co-expression of gene pairs using BigSCale2 (173), which pools cells with similar expression profile. We considered the set of genes from the co-expression network that were direct neighbors of the 124 genes that had been identified as downregulated in the DEG analysis, and we refer to this as the DEG module. The DEG module was visualized by cytoscape (ver 3.7.1) (174). We obtained the enriched pathways for the DEG module by GO enrichment analysis (175) implemented in Gene Ontology website (http://geneontology.org/).

Hypoxic score

Hypoxic signature scores were calculated using the Seurat function AddModuleScore that calculates the average expression of a given signature per cell and subtracts it from the average expression of randomly selected control features. AddModuleScore (176) was run using 100 control features. Scores were averaged within all cells from the same cluster and tumor region (p27K+ or p27K- areas). To compare the hypoxic signature across populations we generated a delta score subtracting the average score of p27K- areas to that of p27K+ areas for each cluster of cells. Hypoxic signature was formed by: Hif1a, Slc2a1, Vegfa, Hmox1, Bnip3, Nos2, Mmp2, Sod3, Cited2, Ldha. This list is constituted by genes from the GO:0001666 “Response to hypoxia” that were upregulated in mVenus-p27K+ QCCs. Statistical analysis was performed by two-sided Wilcoxon rank sum test followed by BH correction.

Statistical analysis

All analysis was performed using data from at least three independent biological replicates (exact number of replicates are stated in the figure legend). Unless stated otherwise, all statistical analyses were performed in PRISM6 software using paired or unpaired Student’s t test.

7. REFERENCES

References

1. *Ueber den jetzigen stand der Karzinomforschung.* **Ehrlich, P.** (1909)., Ned.Tijdschr. Geneeskd. 5, 273–290 .

2. **Silverstein, A. M.** *A History of Immunology.* s.l. : Academic, San Diego, CA, 1989.

3. *Tumor antigens.* **Klein, G.** s.l. : Annu. Rev. Microbiol. 20, 223–252, (1966).

4. *The concept of immunological surveillance.* **Burnet, F. M.** s.l. : Prog. Exp.Tumor Res. 13, 1–27, (1970).

5. *Cellular and Humoral Aspects of the Hypersensitive States.* **Thomas, L.** Hoeber-Harper, New York, : ed. Lawrence, H. S.) 529–532, 1959).

6. *Demonstration of an interferon γ-dependent tumor surveillance system in immunocompetent mice.* **Kaplan, D. H. et al.** s.l. : Proc. Natl.Acad. Sci. USA 95, 7556–7561, (1998).

7. *Perforin and interferon-γ activities independently control tumor initiation, growth, and metastasis.* **Street, S. E., Cretney, E. & Smyth, M. J.** s.l. : Blood 97, 192–197 , (2001).

8. *Sarcomas in organ allograft recipients.* **Penn, I.** s.l. : Transplantation 60, 1485–1491, (1995).

9. *Solid tumors after heart transplantation: lethality of lung cancer. .* **Pham, S. M. et al.** s.l. : Ann.Thorac. Surg. 60, 1623–1626, (1995).

10. *CD8+ T cells infiltrated within cancer cell nests as a prognostic factor in human colorectal cancer. .* **Naito, Y. et al.** s.l. : Cancer Res. 58, 3491–3494, (1998).

11. *IFN-γ and lymphocytes prevent primary tumour development and shape tumour immunogenicity. .* **Shankaran V, Ikeda H, Bruce AT, et al..** s.l. : Nature 410: 1107-1111., (2001).

12. *Cancer immunoediting: from immunosurveillance to tumor escape.* **Dunn GP, Bruce AT, Ikeda H, Old LJ, Schreiber RD.** s.l. : Nat Immunol. Nov;3(11):991-8. doi: 10.1038/ni1102-991. PMID: 12407406., 2002.

13. *Adaptive immunity maintains occult cancer in an equilibrium state.* **Koebel CM, Vermi W, Swann JB, et al..** s.l. : Nature 450: 903-907., (2007).

14. *Cancer immunoediting hypothesis: history, clinical implications and controversies.* **W., Lasek.** s.l. : Cent Eur J Immunol. 47(2):168-174. doi: 10.5114/ceji.2022.117376. Epub 2022 Jun 30. PMID: 36751395; PMCID: PMC9894085., 2022.

15. **Abbas, A.K., Lichtman, A.H. and Pillai, S.** *Cellular and Molecular Immunology. .* s.l. : 8th Edition, Elsevier Saunders, Philadelphia, 199-337, (2015) .

16. *CD8+ T cells in the cancer-immunity cycle.* **Giles JR, Globig AM, Kaech SM, Wherry EJ.** s.l. : Immunity. 2023 Oct 10;56(10):2231-2253. doi: 10.1016/j.immuni.2023.09.005. PMID: 37820583., 2023.

17. *Viral persistence alters CD8 T-cell immunodomi- nance and tissue distribution and results in distinct stages of functional impairment. .* **Wherry, E.J., Blattman, J.N., Murali-Krishna, K., van der Most, R., and Ahmed, R.** s.l. : J. Virol. 77, 4911–4927., (2003). .

18. *Subsets of exhausted CD8+ T cells differentially mediate tumor control and respond to checkpoint blockade.* **Miller, B.C., Sen, D.R., Al Abosy, R., Bi, K., Virkud, Y.V., LaFleur, M.W., Yates, K.B., Lako, A., Felt, K., Naik, G.S., et al.** s.l. : Nat. Immunol. 20, 326–336. , 2019.

19. *T cell exhaustion.* **Wherry, E.J.** s.l. : Nat. Immunol. 12, 492–499., (2011). .

20. *Defining CD8+ T cells that provide the proliferative burst after PD-1 therapy. .* **Im SJ, Hashimoto M, Gerner MY, Lee J, Kissick HT, Burger MC, Shan Q, Hale JS, Lee J, Nasti TH, Sharpe AH, Freeman GJ, Germain RN, Nakaya HI, Xue HH, Ahmed R.** s.l. : Nature. 2016 Sep 1, 2016.

21. *Developmental relationships of four exhausted CD8+ T cell subsets reveals underlying transcriptional and epigenetic landscape control mechanisms.* **Beltra, J.C.,**

Manne, S., Abdel-Hakeem, M.S., Kurachi, M., Giles, J.R., Chen, Z., Casella, V., Ngiow, S.F., Khan, O., Huang, Y.J., et al. s.l. : Immunity 52, 825–841.e8. , 2020.

22. *Hypoxia drives CD39-dependent suppressor function in exhausted T cells to limit antitumor immunity. .* **Vignali, P.D.A., DePeaux, K., Watson, M.J. et al.** s.l. : Nat Immunol 24, 267–279 (2023)., 2023.

23. *Cytotoxic T cells recognize fragments of the influenza nucleoprotein.* **Townsend AR, Gotch FM, Davey J.** s.l. : Cell 42, 457–467, (1985).

24. *Intradermal immunization of C3H mice against a sarcoma that originated in an animal of the same line. .* **L., Gross.** s.l. : Cancer Res. 1943;3(5):326–333.

25. *Immunogenic (tum-) variants of mouse tumor P815: cloning of the gene of tum- antigen P91A and identification of the tum- mutation. .* **De Plaen E, et al.** s.l. : Proc Natl Acad Sci U S A. 1988;85(7):2274–2278. doi: 10.1073/pnas.85.7.2274.

26. *A unique tumor antigen produced by a single amino acid substitution. .* **Monach PA, Meredith SC, Siegel CT, Schreiber H.** 1995 : Immunity. 1995;2(1):45–59. doi: 10.1016/1074-7613(95)90078-0.

27. *A major chromatin regulator determines resistance of tumor cells to T cell-mediated killing. .* **Pan, D., Kobayashi, A., Jiang, P., De Andrade, L.F., Tay, R.E., Luoma, A.M., Tsoucas, D., Qiu, X., Lim, K., Rao, P., et al.** s.l. : Science 359, 770–775., (2018).

28. *Identification of essential genes for cancer immunotherapy. .* **Patel, S.J., Sanjana, N.E., Kishton, R.J., Eidizadeh, A., Vodnala, S.K., Cam, M., Gartner, J.J., Jia, L., Steinberg, S.M., Yamamoto, T.N., et al.** s.l. : Nature 548, 537–542., (2017).

29. *GFP-specific CD8 T cells enable targeted cell depletion and visualization of T-cell interactions.* **Agudo J, Ruzo A, Park ES, Sweeney R, Kana V, Wu M, Zhao Y, Egli D, Merad M, Brown BD.** s.l. : Nat Biotechnol. 2015 Dec;33(12):1287-1292. doi: 10.1038/nbt.3386. Epub , 2015.

30. *Stromal circuits involving tumor-associated macrophages and cancer-associated fibroblasts. .* **Timperi E, Romano E.** s.l. : Front Immunol. 2023 Jun 5;14:1194642. doi: 10.3389/fimmu.2023.1194642. PMID: 37342322; PMCID: PMC10277481., 2023.

31. *TGF-β-associated extracellular matrix genes link cancer-associated fibroblasts to immune evasion and immunotherapy failure.* **Chakravarthy, A., Khan, L., Bensler, N. P., Bose, P. & Carvalho, D. D. D.** s.l. : Nat. Commun. 9, 4692., (2018).

32. *Single-Cell RNA Sequencing Reveals Stromal Evolution into LRRC15+ Myofibroblasts as a Determinant of Patient Response to Cancer Immunotherapy.* **Dominguez CX, Müller S, Keerthivasan S, Koeppen H, Hung J, Gierke S, Breart B, Foreman O, Bainbridge TW, Castiglioni A, Senbabaoglu Y, Modrusan Z, Liang Y, Junttila MR, Klijn C, Bourgon R, Turley SJ.** 2020 : Cancer Discov. 2020 Feb;10(2):232-253. doi: 10.1158/2159-8290.CD-19-0644. Epub 2019 Nov 7. PMID: 31699795.

33. *LRRC15+ myofibroblasts dictate the stromal setpoint to suppress tumour immunity.* **Krishnamurty AT, Shyer JA, Thai M, Gandham V, Buechler MB, Yang YA, Pradhan RN, Wang AW, Sanchez PL, Qu Y, Breart B, Chalouni C, Dunlap D, Ziai J, Elstrott J, Zacharias N, Mao W, Rowntree RK, Sadowsky J, Lewis GD, Pillow TH, Nabet BY, Banchereau R, Tam L,.** 2022 : Nature. 2022 Nov;611(7934):148-154. doi: 10.1038/s41586-022-05272-1. Epub 2022 Sep 28. PMID: 36171287; PMCID: PMC9630141.

34. *Single-cell analysis reveals fibroblast clusters linked to immunotherapy resistance in cancer. .* **Kieffer Y, Hocine HR, Gentric G, Pelon F, Bernard C, Bourachot B, et al.** 2020 : Cancer Discovery (2020) 10:1330–51. doi: 10.1158/2159-8290.CD-19-1384.

35. *Identification of a novel cell type in peripheral lymphoid organs of mice. i. morphology, quantitation, tissue distribution. .* **Steinman RM, Cohn ZA.** s.l. : J Exp Med (1973) 137 (5):1142–62. doi: 10.1084/jem.137.5.1142, 1973.

36. *Dendritic cells as shepherds of T cell immunity in cancer. .* **Pittet MJ, Di Pilato M, Garris C, Mempel TR.** s.l. : Immunity. 2023 Oct 10;56(10):2218-2230. doi:

10.1016/j.immuni.2023.08.014. Epub 2023 Sep 13. PMID: 37708889; PMCID: PMC10591862., 2023.

37. *Melanoma-intrinsic beta-catenin signalling prevents anti-tumour immunity. .* **Spranger, S., Bao, R., and Gajewski, T.F.** 2015 : Nature 523, 231–235. https://doi.org/10.1038/nature14404.

38. *A natural killer-dendritic cell axis defines checkpoint therapy-responsive tumor microenvironments.* **Barry KC, Hsu J, Broz ML, Cueto FJ, Binnewies M, Combes AJ, Nelson AE, Loo K, Kumar R, Rosenblum MD, Alvarado MD, Wolf DM, Bogunovic D, Bhardwaj N, Daud AI, Ha PK, Ryan WR, Pollack JL, Samad B, Asthana S, Chan V, Krummel MF.** s.l. : Nat Med. 2018 Aug;24(8):1178-1191. doi: 10.1038/s41591-018-0085-8. Epub 2018 Jun 25. PMID: 29942093; PMCID: PMC6475503., 2018.

39. *Impaired function of dendritic cells within the tumor microenvironment. .* **Xiao Z, Wang R, Wang X, Yang H, Dong J, He X, Yang Y, Guo J, Cui J, Zhou Z.** s.l. : Front Immunol. 2023 Jun 27;14:1213629., 2023.

40. *Expansion and Activation of CD103(+) Dendritic Cell Progenitors at the Tumor Site Enhances Tumor Responses to Therapeutic PD-L1 and BRAF Inhibition.* **Salmon H, Idoyaga J, Rahman A, Leboeuf M, Remark R, Jordan S, Casanova-Acebes M, Khudoynazarova M, Agudo J, Tung N, Chakarov S, Rivera C, Hogstad B, Bosenberg M, Hashimoto D, Gnjatic S, Bhardwaj N, Palucka AK, Brown BD, Brody J, Ginhoux F, Merad M.** s.l. : Immunity. 2016 Apr 19;44(4):924-38., 2016.

41. *Critical Role for CD103(+)/CD141(+) Dendritic Cells Bearing CCR7 for Tumor Antigen Trafficking and Priming of T Cell Immunity in Melanoma.* **Roberts EW, Broz ML, Binnewies M, Headley MB, Nelson AE, Wolf DM, Kaisho T, Bogunovic D, Bhardwaj N, Krummel MF.** s.l. : Cancer Cell. 2016 Aug 8;30(2):324-336., 2016.

42. *Molecular mechanisms of T cell co-stimulation and coinhibition. .* **Chen L, Flies DB.** s.l. : Nat Rev Immunol (2013) 13(4):227–42. doi: 10.1038/nri3405, 2013.

43. *Trans-endocytosis of CD80 and CD86: a molecular basis for the cell-extrinsic function of CTLA-4. .* **Qureshi OS, Zheng Y, Nakamura K, Attridge K, Manzotti C, Schmidt EM,**

et al. s.l. : Sci (New York NY). (2011) 332(6029):600–3. doi: 10.1126/science.1202947, 2011.

44. *Silencing IDO2 in dendritic cells: a novel strategy to strengthen cancer immunotherapy in a murine lung cancer model.* **Liu Y, Xu P, Liu H, Fang C, Guo H, Chen X, et al. Silencing IDO2 in dendritic cells: a novel strategy to strengthen cancer immunotherapy in a murine lung cancer model.** s.l. : Int J Oncol (2020) 57(2):587–97. doi: 10.3892/ijo.2020.5073, 2020.

45. *Hepatic carcinoma-associated fibroblasts induce IDO-producing regulatory dendritic cells through IL-6-mediated STAT3 activation. .* **Cheng JT, Deng YN, Yi HM, Wang GY, Fu BS, Chen WJ, et al.** s.l. : Oncogenesis (2016) 5(2):e198. doi: 10.1038/oncsis.2016.7, 2016.

46. *The receptor DNGR-1 signals for phagosomal rupture to promote cross-presentation of dead-cell-associated antigens.* **Canton, J., Blees, H., Henry, C.M., Buck, M.D., Schulz, O., Rogers, N.C., Childs, E., Zelenay, S., Rhys, H., Domart, M.C., et al.** s.l. : Nat. Immunol. 22,140-153. https://doi.org/10.1038/s41590-020-00824-x, 2021.

47. *Batf3 deficiency reveals a critical role for CD8alpha+ dendritic cells in cytotoxic T cell immunity.* **Hildner, K., Edelson, B.T., Purtha, W.E., Diamond, M., Matsushita, H., Kohyama, M., Calderon, B., Schraml, B.U., Unanue, E.R., Diamond, M.S., et al.** s.l. : Science 322,1097-1100. https://doi.org/10.1126/science.1164206, 2008.

48. *Dissecting the tumor myeloid compartment reveals rare activating antigen-presenting cells critical for T cell immunity.* **Broz, M.L., Binnewies, M., Boldajipour, B., Nelson, A.E., Pollack, J.L., Erle, D.J., Barczak, A., Rosenblum, M.D., Daud, A., Barber, D.L., et al.** s.l. : Cancer Cell 26, 938. https://doi.org/10.1016/j.ccell.2014.11.010., 2014.

49. *NK Cells Stimulate Recruitment of cDC1 into the Tumor Microenvironment Promoting Cancer Immune Control. .* **Böttcher JP, Bonavita E, Chakravarty P, Blees H, Cabeza-Cabrerizo M, Sammicheli S, Rogers NC, Sahai E, Zelenay S, Reis e Sousa C.** s.l. : Cell. 2018 Feb 22;172(5):1022-1037.e14. doi: 10.1016/j.cell.2018.01.004. Epub 2018 Feb 8. PMID: 29429633; PMCID: PMC5847168., 2018.

50. *Intratumoral Activity of the CXCR3 Chemokine System Is Required for the Efficacy of Anti-PD-1 Therapy. .* **Chow, M.T., Ozga, A.J., Servis, R.L., Frederick, D.T., Lo, J.A., Fisher, D.E., Freeman, G.J., Boland, G.M., and Luster, A.D.** s.l. : Immunity 50, 1498-1, (2019). .

51. *Tumor-infiltrating dendritic cell states are conserved across solid human cancers. .* **Gerhard, G.M., Bill, R., Messemaker, M., Klein, A.M., and Pittet, M.J.** s.l. : J. Exp. Med. 218, e20200264. https://doi.org/10.1084/ jem.20200264, (2021).

52. *A pan-cancer single-cell transcriptional atlas of tumor infiltrating myeloid cells. .* **Cheng, S., Li, Z., Gao, R., Xing, B., Gao, Y., Yang, Y., Qin, S., Zhang, L., Ouyang, H., Du, P., et al.** s.l. : Cell 184, 792–809.e23. https:// doi.org/10.1016/j.cell.2021, (2021).

53. *A conserved dendritic-cell regulatory program limits antitumour immunity. .* **Maier, B., Leader, A.M., Chen, S.T., Tung, N., Chang, C., LeBerichel, J., Chudnovskiy, A., Maskey, S., Walker, L., Finnigan, J.P., et al.** s.l. : Nature 580, 257–262., (2020).

54. *Successful anti-PD-1 cancer immunotherapy requires T cell-dendritic cell crosstalk involving the cytokined IFN-gamma and IL-12.* **Garris, C.S., Arlauckas, S.P., Kohler, R.H., Trefny, M.P., Garren, S., Piot, C., Engblom, C., Pfirschke, C., Siwicki, M., Gungabeesoon, J., et al.** s.l. : Immunity 49, 1148-1161.e7.https://doi.org/10.1016/j.immuni.2018.09.024., (2018).

55. *CXCR6 positions cytotoxic T cells to receive critical survival signals in the tumor microenvironment.* **Di Pilato, M., Kfuri-Rubens, R., Pruessmann, J.N., Ozga, A.J., Messemaker, M., Cadilha, B.L., Sivakumar, R., Cianciaruso, C., Warner, R.D., Marangoni, F., et al.** s.l. : Cell 184, 4512-4530.e22. https://doi.org/10.1016/j.cell.2021.07.015., 2021.

56. *Interleukin-12 from CD103+ Batf3-dependent dendritic cells required for NK-cell suppression of metastasis.* **Mittal, D., Vijayan, D., Putz, E.M., Aguilera, A.R., Markey, K.A., Straube, J., Kazakoff, S., Nutt, S.L., Takeda, K., Hill, G.R., et al.** s.l. : Cancer Immunol. Res. 5, 1098-1108. https://doi.org/10.1158/2326-6066.CIR-17-0-341., (2017).

57. *HIFs, angiogenesis, and metabolism: elusive enemies in breast cancer. .* **de Heer EC, Jalving M, Harris AL.** s.l. : J Clin Invest. 2020 Oct 1;130(10):5074-5087. , 2020.

58. *The proteoglycan-like domain of carbonic anhydrase IX mediates non-catalytic facilitation of lactate transport in cancer cells. .* **Ames S, Pastorekova S, Becker HM.** s.l. : Oncotarget. 2018;9(46):27940–27957., 2018.

59. *Hypoxia as a potential inducer of immune tolerance, tumor plasticity and a driver of tumor mutational burden: Impact on cancer immunotherapy.* **Abou Khouzam R, Janji B, Thiery J, Zaarour RF, Chamseddine AN, Mayr H, Savagner P, Kieda C, Gad S, Buart S, Lehn JM, Limani P, Chouaib S.** s.l. : Semin Cancer Biol. 2023 Dec;97:104-123., 2023.

60. *Hypoxia increases melanoma-associated fibroblasts immunosuppressive potential and inhibitory effect on T cell-mediated cytotoxicity. .* **Ziani L, Buart S, Chouaib S, Thiery J.** s.l. : Oncoimmunology. 2021 Jul 25;10(1):1950953., 2021.

61. *PD-L1 is a novel direct target of HIF-1α, and its blockade under hypoxia enhanced MDSC-mediated T cell activation.* **Noman MZ, Desantis G, Janji B, Hasmim M, Karray S, Dessen P, Bronte V, Chouaib S.** s.l. : J Exp Med. 2014 May 5;211(5):781-90. doi: 10.1084/jem.20131916. Epub 2014 Apr 28. PMID: 24778419; PMCID: PMC4010891., 2014.

62. *Hypoxia-inducible factors enhance the effector responses of CD8+ T cells to persistent antigen. .* **Doedens, A.L., Phan, A.T., Stradner, M.H., Fujimoto, J.K., Nguyen, J.V., Yang, E., Johnson, R.S., and Goldrath, A.W.** s.l. : Nat. Immunol. 14, 1173–1182. , (2013).

63. *Efficacy of PD-1 blockade is potentiated by metformin-induced reduction of tumor hypoxia. .* **Scharping, N.E., Menk, A.V., Whetstone, R.D., Zeng, X., and Delgoffe, G.M.** s.l. : Cancer Immunol. Res. 5, 9–16. , (2017). .

64. *The prognostic value of hypoxia-inducible factor-1α in advanced cancer survivors: a meta-analysis with trial sequential analysis. .* **Han S, Huang T, Hou F, Yao L, Wang X,**

Wu X. s.l. : Ther Adv Med Oncol. 2019 Sep 24;11:1758835919875851. doi: 10.1177/175883591987585, 2019.

65. *The tumor microenvironment (TME) and atezolizumab + nab-paclitaxel (A+nP) activity in metastatic triple-negative breast cancer (mTNBC): IMpassion130.* **Emens, L.A., Goldstein, L.D., Schmid, P., Rugo, H.S., Adams, S., Barrios, C.H., Schneeweiss, A., Dieras, V., Iwata, H., Chang, C.-W., et al.** s.l. : J. Clin. Oncol. 39, 1006. , 2021.

66. *Hypoxia and hypoxia-inducible factor-1 alpha modulate lipopolysaccharide-induced dendritic cell activation and function.* **Jantsch J, Chakravortty D, Turza N, Prechtel AT, Buchholz B, Gerlach RG, Volke M, Gläsner J, Warnecke C, Wiesener MS, Eckardt KU, Steinkasserer A, Hensel M, Willam C.** s.l. : J Immunol. 2008 Apr 1;180(7):4697-705., 2008.

67. *(Influence of hypoxia-inducible factor 1α on dendritic cell differentiation and migration.* **Köhler, T., Reizis, B., Johnson, R.S., Weighardt, H., and Förster, I.** s.l. : Eur. J. Immunol. 42, 1226–1236., 2012).

68. *CCR7 Chemokine Receptor-Inducible lnc-Dpf3 Restrains Dendritic Cell Migration by Inhibiting HIF-1α-Mediated Glycolysis.* **Liu, J., Zhang, X., Chen, K., Cheng, Y., Liu, S., Xia, M., Chen, Y., Zhu, H., Li, Z., and Cao, X.** s.l. : Immunity 50, 600-615.e15., 2019.

69. *Role of solute carrier transporters in regulating dendritic cell maturation and function. .* **Shao L, Yang M, Sun T, Xia H, Du D, Li X, Jie Z.** s.l. : Eur J Immunol. 2023 Dec 11:e2350385., 2023.

70. *Antiparallel segregation of notch components in the immunological synapse directs reciprocal signaling in allogeneic Th:DC conjugates. .* **Luty, W. H., Rodeberg, D., Parness, J. and Vyas, Y. M.,.** s.l. : J. Immunol. 2007. 179: 819–829., 2007.

71. *The tumor micro- environment represses T cell mitochondrial biogenesis to drive intratu- moral T cell metabolic insufficiency and dysfunction.* **Scharping, N.E., Menk, A.V., Moreci, R.S., Whetstone, R.D., Dadey, R.E., Watkins, S.C., Ferris, R.L., and Delgoffe, G.M.** s.l. : Immunity 45, 374–388. , 2016.

72. *PD-1 alters T-cell metabolic reprogramming by inhibiting glycolysis and promoting lipolysis and fatty acid oxidation.* **Patsoukis, N., Bardhan, K., Chatterjee, P., Sari, D., Liu, B., Bell, L.N., Kar- oly, E.D., Freeman, G.J., Petkova, V., Seth, P., et al.** s.l. : Nat. Commun. 6, 6692. , 2015.

73. *Metabolic Control of CD8+ T Cell Fate Decisions and Antitumor Immunity. .* **Zhang L, Romero P.** s.l. : Trends Mol Med. 2018 Jan;24(1):30-48., 2018.

74. *LDHA-Associated Lactic Acid Production Blunts Tumor Immunosurveillance by T and NK Cells.* **Brand A, Singer K, Koehl GE, Kolitzus M, Schoenhammer G, Thiel A, Matos C, Bruss C, Klobuch S, Peter K, Kastenberger M, Bogdan C, Schleicher U, Mackensen A, Ullrich E, Fichtner-Feigl S, Kesselring R, Mack M, Ritter U, Schmid M, Blank C, Dettmer K, et al.** s.l. : Cell Metab. 2016 Nov 8;24(5):657-671., 2016.

75. *Dendritic cell reprogramming by endogenously produced lactic acid. .* **Nasi, A., Fekete, T., Krishnamurthy, A., Snowden, S., Rajnavölgyi, E., Catrina, A. I., Wheelock, C. E., et al.,.** s.l. : J. Immunol. 2013. 191: 3090– 3099., 2013.

76. *Lactate dependent regulation of immune responses by dendritic cells and macrophages. .* **Manoharan, I., Prasad, D., Thangaraju, M. and Manicassamy, S.,.** s.l. : Front. Immunol. 2021. 12: 691134, 2021.

77. *Monocarboxylate transporter 1 blockade with AZD3965 inhibits lipid biosynthesis and increases tumour immune cell infiltration.* **Beloueche-Babari, M., Casals Galobart, T., Delgado-Goni, T.,Wantuch, S., Parkes, H. G., Tandy, D., Harker, J. A., et al.,.** s.l. : Br. J. Cancer. 2020. 122: 895–903., 2020.

78. *Deep profiling of mouse splenic architecture with CODEX multiplexed imaging. .* **Goltsev Y, Samusik N, Kennedy-Darling J, Bhate S, Hale M, Vazquez G, Black S, Nolan GP.** s.l. : Cell 174, 968–981.e15 , (2018).

79. *Highly multiplexed imaging of single cells using a high-throughput cyclic immunofluorescence method. .* **Lin JR, Fallahi-Sichani M, Sorger PK.** s.l. : Nat Commun. 2015 Sep 24;6:8390. doi: 10.1038/ncomms9390. PMID: 26399630; PMCID: PMC4587398., 2015.

80. *Multiplexed ion beam imaging of human breast tumors.* **Angelo M, Bendall SC, Finck R, Hale MB, Hitzman C, Borowsky AD, Levenson RM, Lowe JB, Liu SD, Zhao S, Natkunam Y, Nolan GP.** s.l. : Nat Med. 2014 Apr;20(4):436-42. doi: 10.1038/nm.3488. Epub 2014 Mar 2. PMID: 2, 2014.

81. *Visualization and Analysis of Gene Expression in Tissue Sections by Spatial Transcriptomics.* **PL, Stahl, et al.** s.l. : Science 2016, 353 (6294), 78–82. 10.1126/science.aaf2403., 2016.

82. *Genome-Wide RNA Tomography in the Zebrafish Embryo. .* **P., Junker J., et al.** s.l. : Cell 2014, 159 (3), 662–675. 10.1016/j.cell.2014.09.038., 2014.

83. *Spatially Resolved, Highly Multiplexed RNA Profiling in Single Cells. .* **H., Chen K., et al.** s.l. : Science 2015, 348 (6233), 1360–1363. 10.1126/science.aaa6090., 2015.

84. *Spatial Transcriptome Profiling by MERFISH Reveals Subcellular RNA Compartmentalization and Cell Cycle-Dependent Gene Expression.* **C., Xia, et al.** s.l. : Proc. Natl. Acad. Sci. U. S. A. 2019, 116 (39), 19490–19499. 10.1073/pnas.19124, 2019.

85. *Monitoring cellular movement in vivo with photoconvertible fluorescence protein "Kaede" transgenic mice.* **Tomura, M., Yoshida, N., Tanaka, J., Karasawa, S., Miwa, Y., Miyawaki, A., and Kanagawa, O.** s.l. : Proc. Natl. Acad. Sci. USA 105, 10871–10876. , 2008.

86. *Spatial reconstruction of immune niches by combining photoactivatable reporters and scRNA-seq. .* **Medaglia C, Giladi A, Stoler-Barak L, De Giovanni M, Salame TM, Biram A, David E, Li H, Iannacone M, Shulman Z, Amit I.** s.l. : Science. 2017 Dec 22;358(6370):1622-1626, 2017.

87. **Society, American Cancer.** Key statistics for Breast Cancer. [Online] https://www.cancer.org/cancer/types/breast-cancer/about/how-common-is-breast-cancer.html.

88. —. Triple Negative Breast Cancer. [Online] https://www.cancer.org/cancer/types/breast-cancer/about/types-of-breast-cancer/triple-negative.html.

89. *Cancer progression and the invisible phase of metastatic colonization. .* **CA., Klein.** s.l. : Nat Rev Cancer 20: 681–694. doi:10.1038/s41568-020-00300-6, 2020.

90. *Analysis of pattern, time and risk factors influencing recurrence in triple-negative breast cancer patients .* **Pien´kowski, Katarzyna Pogoda • Anna Niwin´ska • Magdalena Murawska • Tadeusz.** s.l. : Med Oncol (2013) 30:388 DOI 10.1007/s12032-012-0388-4, 2013.

91. *Disseminated tumour cells from the bone marrow of early breast cancer patients: results from an international pooled analysis.* **Hartkopf AD, Brucker SY, Taran FA, Harbeck N, von Au A, Naume B, Pierga JY, Hoffmann O, Beckmann MW, Rydén L, et al.** s.l. : Eur J Cancer 154: 128– 137. doi:10.1016/j.ejca.2021.06.028, 2021. .

92. *Models, mechanisms and clinical evidence for cancer dormancy. .* **JA., Aguirre-Ghiso.** s.l. : Nat Rev Cancer 7: 834– 846. doi:10.1038/nrc2256, 2007. .

93. *Phenotypic heterogeneity of disseminated tumour cells is preset by primary tumour hypoxic microenvironments.* **Fluegen, G., Avivar-Valderas, A., Wang, Y., Padgen, M.R., Williams, J.K., Nobre, A.R., Calvo, V., Cheung, J.F., Bravo-Cordero, J.J., Entenberg, D., et al.** s.l. : Nat. Cell Biol. 19, 120–132. , 2017.

94. *Targeting metastasis-initiating cells through the fatty acid receptor CD36.* **Pascual, G., Avgustinova, A., Mejetta, S., Martı´n, M., Castellanos, A., Attolini, C.S.O., Berenguer, A., Prats, N., Toll, A., Hueto, J.A., et al.** s.l. : Nature 541, 41–45. , (2017).

95. *Persistent cancer cells: the deadly survivors. .* **Shen S, Vagner S, Robert C.** s.l. : Cell 183: 860–874. doi:10.1016/j.cell .2020.10.027, 2020. .

96. *Type I interferon/IRF7 axis instigates chemotherapy-induced immunological dormancy in breast cancer. .* **Lan Q, Peyvandi S, Duffey N, Huang YT, Barras D, Held W, Richard F, Delorenzi M, Sotiriou C, Desmedt C, et al.** s.l. : Oncogene 38: 2814–2829. doi:10.1038/s41388-018- 0624-2, 2019. .

97. *CD39+ PD-1+ CD8+ T cells mediate metastatic dormancy in breast cancer. .* **allón de Lara P, Castañón H, Vermeer M, Núñez N, Silina K, Sobottka B, Urdinez J,**

Cecconi V, Yagita H, Movahedian Attar F, et al. s.l. : Nat Commun 12: 769–769. doi:10.1038/s41467-021-2, 2021.

98. *Hepatic stellate cells suppress NK cell-sustained breast cancer dormancy. .* **Correia AL, Guimaraes JC, Auf der Maur P, De Silva D, Trefny MP, Okamoto R, Bruno S, Schmidt A, Mertz K, Volkmann K, et al.** s.l. : Nature 594: 566–571. doi:10.1038/s41586-021-03614-z, 2021.

99. *HIF-1 mediates metabolic responses to intratumoral hypoxia and oncogenic mutations. .* **GL., Semenza.** s.l. : J Clin Invest. 2013;123(9):3664–3671., 2013.

100. *Hypoxia-inducible factors: coupling glucose metabolism and redox regulation with induction of the breast cancer stem cell phenotype. .* **GL., Semenza.** s.l. : EMBO J. 2017 Feb 1;36(3):252-259. doi: 10.15252/embj.201695204. Epub 2016 Dec 22. PMID: 28007895; PMCID: PMC52, 2016.

101. *Levels of hypoxia-inducible factor-1 alpha during breast carcinogenesis. .* **Bos R, Zhong H, Hanrahan CF, Mommers EC, Semenza GL, Pinedo HM, Abeloff MD, Simons JW, van Diest PJ, van der Wall E.** s.l. : J Natl Cancer Inst. 2001 Feb 21;93(4):309-14. doi: 10.1093/jnci/9, 2001.

102. *Targeting Hypoxia-Induced Carbonic Anhydrase IX Enhances Immune-Checkpoint Blockade Locally and Systemically. .* **Chafe SC, McDonald PC, Saberi S, Nemirovsky O, Venkateswaran G, Burugu S, Gao D, Delaidelli A, Kyle AH, Baker JHE, Gillespie JA, Bashashati A, Minchinton AI, Zhou Y, Shah SP, Dedhar S.** s.l. : Cancer Immunol Res. 2019 Jul;7(7):1064-1078. doi: 10.1158/2326-6066.CIR-18-0657. Epub 2019 May 14. PMID: 31088846., 2019.

103. *Hypoxia-inducible factors promote breast cancer stem cell specification and maintenance in response to hypoxia or cytotoxic chemotherapy. .* **Xiang L, Semenza GL.** s.l. : Adv Cancer Res. 2019;141:175-212. doi: 10.1016/bs.acr.2018.11.001. Epub 2018 Dec 19. PMID: 30691, 2019.

104. *BRCA1-IRIS promotes human tumor progression through PTEN blockade and HIF-1α activation.* **Li AG, Murphy EC, Culhane AC, Powell E, Wang H, Bronson RT, Von**

T, Giobbie-Hurder A, Gelman RS, Briggs KJ, Piwnica-Worms H, Zhao JJ, Kung AL, Kaelin WG Jr, Livingston DM. s.l. : Proc Natl Acad Sci U S A. 2018 Oct 9;115(41):E9600-E9609. doi: 10.1073/pnas.1807112115. Epub 2018 Sep 25. PMID: 30254159; PMCID: PMC6187201., 2018.

105. *HIF-1α overexpression in ductal carcinoma in situ of the breast in BRCA1 and BRCA2 mutation carriers.* **van der Groep P, van Diest PJ, Smolders YH, Ausems MG, van der Luijt RB, Menko FH, Bart J, de Vries EG, van der Wall E.** s.l. : PLoS One. 2013;8(2):e56055. doi: 10.1371/journal.pone.0056055. Epub 2013 Feb 8. PMID: 23409121; PMCID: PMC3568038., 2013.

106. *Comprehensive molecular portraits of human breast tumours. .* **Network., Cancer Genome Atlas.** s.l. : Nature. 2012 Oct 4;490(7418):61-70. doi: 10.1038/nature11412. Epub 2012 Sep 23. PMID: 23000897; PMCID: PMC3465532., 2014.

107. *Molecular Portrait of Hypoxia in Breast Cancer: A Prognostic Signature and Novel HIF-Regulated Genes. .* **Ye IC, Fertig EJ, DiGiacomo JW, Considine M, Godet I, Gilkes DM.** s.l. : Mol Cancer Res. 2018 Dec;16(12):1889-1901. doi: 10.1158/1541-7786.MCR-18-0345. Epub 2018, 2018.

108. *The N-terminal transactivation domain confers target gene specificity of hypoxia-inducible factors HIF-1alpha and HIF-2alpha. .* **Hu CJ, Sataur A, Wang L, Chen H, Simon MC.** s.l. : Mol Biol Cell. 2007 Nov;18(11):4528-42. Epub 2007 Sep 5. 10.1091/mbc.e06-05-0419, 2007.

109. *Safety and tumor responses with lambrolizumab (anti-PD-1) in melanoma. .* **Hamid O, Robert C, Daud A et al.** s.l. : N. Engl. J. Med. 369(2), 134–144 (2013)., 2013.

110. *Improved survival with ipilimumab in patients with metastatic melanoma. .* **Hodi FS, O'day SJ, Mcdermott DF et al.** s.l. : N. Engl. J. Med. 363(8), 711–723 , (2010).

111. *Inhibitory B7-family molecules in the tumour microenvironment. .* **Zou W, Chen L.** s.l. : Nat. Rev. Immunol. 8(6), 467–477 , (2008).

112. *Safety and tumor responses with lambrolizumab (anti-PD-1) in melanoma. .* **Hamid O, Robert C, Daud A et al.** s.l. : N. Engl. J. Med. 369(2), 134–144 , (2013).

113. *Pembrolizumab monotherapy for previously untreated, PD-L1-positive, metastatic triple-negative breast cancer: cohort B of the phase II KEYNOTE-086 study. .* **Adams S, Loi S, Toppmeyer D, et al.** s.l. : Ann Oncol. 2019 Mar;30(3):405–411. doi: 10.1093/ANNONC/MDY518 , 2019.

114. *Pembrolizumab monotherapy for previously treated metastatic triple-negative breast cancer: cohort a of the phase II KEYNOTE-086 study. .* **Adams S, Schmid P, Rugo HS, et al.** s.l. : Ann Oncol. 2019 Mar;30(3):397–404. doi: 10.1093/ANNONC/MDY517, 2019.

115. *Avelumab, an anti-PD-L1 antibody, in patients with locally advanced or metastatic breast cancer: a phase 1b JAVELIN solid tumor study. .* **Dirix LY, Takacs I, Jerusalem G, et al.** s.l. : Breast Cancer Res Treat. 2018 Oct;167(3):671–686. doi: 10.1007/S10549-017-4537-5, 2018.

116. *A pilot study of durvalumab and tremelimumab and immunogenomic dynamics in metastatic breast cancer. .* **Santa-Maria CA, Kato T, Park J-H, et al.** s.l. : Oncotarget. 2018 Apr;9(27):18985. doi: 10.18632/ ONCOTARGET.24867, 2018.

117. *Pembrolizumab plus chemotherapy versus placebo plus chemotherapy for previously untreated locally recurrent inoperable or metastatic triple-negative breast cancer (KEYNOTE-355): a randomised, placebo-controlled, double-blind, phase 3 clinical trial.* **Cortes J, Cescon DW, Rugo HS, et al.** s.l. : Lancet. 2020 Dec;396(10265):1817–1828. doi: 10.1016/S0140-6736(20) 32531-9, 2020.

118. *I-SPY 2: an adaptive breast cancer trial design in the setting of neoadjuvant chemotherapy. .* **Barker AD, Sigman CC, Kelloff GJ, et al.** s.l. : Clin Pharmacol Ther. 2009 Jul;86(1):97–100. doi: 10.1038/CLPT. 2009.68, 2009.

119. *Pembrolizumab plus chemotherapy as neoadjuvant treatment of high-risk, early-stage triple-negative breast cancer: results from the phase 1b open-label, multicohort KEYNOTE-173 study. .* **Schmid P, Salgado R, Park YH, et al.** s.l. : Ann Oncol. 2020 May;31(5):569–581. , 2020.

120. *Neoadjuvant atezolizumab in combination with sequential nab-paclitaxel and anthracycline-based chemotherapy versus placebo and chemotherapy in patients with*

early-stage triple-negative breast cancer (IMpassion031): a randomised, double-blind, phase 3 tria. **Mittendorf EA, Zhang H, Barrios CH, et al.** s.l. : Lancet. 2020 Oct;396(10257):1090–1100. doi: 10.1016/S0140-6736(20) 31953-X, 2020.

121. *KEYNOTE-522, IMpassion031 and GeparNUEVO: changing the paradigm of neoadjuvant immune checkpoint inhibitors in early triple-negative breast cancer. .* **Rizzo A, Cusmai A, Acquafredda S, et al.** s.l. : Future Oncol. 2022 Jun;18(18):2301–2309. doi: 10.2217/ FON-2021-16, 2022.

122. *Therapeutic potential of combining PARP inhibitor and immunotherapy in solid tumors. .* **Vikas P, Borcherding N, Chennamadhavuni A, et al.** s.l. : Front Oncol. 2020 Apr;10. doi: 10.3389/FONC.2020. 00570, 2020.

123. *Olaparib and durvalumab in patients with germline BRCA-mutated metastatic breast cancer (MEDIOLA): an open-label, multicentre, phase 1/2, basket study. .* **Domchek SM, Postel-Vinay S, Im S-A, et al.** s.l. : Lancet Oncol. 2020 Sep;21(9):1155–1164. doi: 10.1016/ S1470-2045(20)30324-7, 2020.

124. *Open-label clinical trial of niraparib combined with pembrolizumab for treatment of advanced or metastatic triple-negative breast cancer.* **Vinayak S, Tolaney SM, Schwartzberg L, et al.** s.l. : JAMA Oncol. 2019 Aug;5(8):1132–1140. doi: 10.1001/JAMAONCOL.2019.1029, 2019.

125. *Durvalumab with olaparib and paclitaxel for high-risk HER2-negative stage II/III breast cancer: results from the adaptively randomized I-SPY2 trial. .* **Pusztai L, Yau C, Wolf DM, et al.** s.l. : Cancer Cell. 2021 Jul;39(7):989–998.e5. doi: 10.1016/J.CCELL.2021.05.009, 2021.

126. *The role of immune checkpoint inhibition in triple negative breast cancer.* **Kidist Tarekegn, Merve Keskinkilic, Tyler J. Kristoff, Sean T. Evans & Kevin Kalinsky.** s.l. : Expert Review of Anticancer Therapy, 23:10, 1095-1106, DOI: 10.1080/14737140.2023.2265059, 2023.

127. *PD-1 regulates self-reactive CD8 + T cell responses to antigen in lymph nodes and tissues. .* **Keir, M.E., Freeman, G.J., and Sharpe, A.H. .** s.l. : J. Immunol. 179, 5064–5070. , (2007).

128. *Unresolved endoplasmic reticulum stress engenders immune-resistant, latent pancreatic cancer metastases.* **Pommier, A., Anaparthy, N., Memos, N., Kelley, Z.L., Gouronnec, A., Yan, R., Auffray, C., Albrengues, J., Egeblad, M., Iacobuzio-Donahue, C.A., et al.** s.l. : Science 360, 1–15., 2018.

129. *Nerve growth factor receptor increases the tumor growth and metastatic potential of triple-negative breast cancer cells. .* **Wu, R., Li, K., Yuan, M., and Luo, K.Q. .** s.l. : Oncogene 40, 2165–2181. , (2021b).

130. *MYC and MCL1 cooperatively promote chemotherapy-resistant breast cancer stem cells via regulation of mitochondrial oxidative phosphorylation.* **Lee, K.-M., Giltnane, J.M., Balko, J.M., Schwarz, L.J., Guerrero-Zotano, A.L., Hutchinson, K.E., Nixon, M.J., Estrada, M.V., Sa´ nchez, V., Sanders, M.E., et al.** s.l. : Cell Metab. 26, 633–647.e7., 2017.

131. *A novel cell-cycle- indicator, mVenus-p27K -, identifies quiescent cells and visualizes G0-G1 transition.* **Oki, T., Nishimura, K., Kitaura, J., Togami, K., Maehara, A., Izawa, K., Sakaue- Sawano, A., Niida, A., Miyano, S., Aburatani, H., et al.** s.l. : Sci. Rep. 4, 4012. , 2014.

132. *Chemotherapy-induced Ca2+ release stimulates breast cancer stem cell enrichment.* **Lu, H., Chen, I., Shimoda, L.A., Park, Y., Zhang, C., Tran, L., Zhang, H., and Semenza, G.L.** s.l. : Cell Rep. 18, 1946–1957. , (2017).

133. *KDM5 histone demethylase activity links cellular transcriptomic heterogeneity to therapeutic resistance.* **Hinohara, K., Wu, H.J., Vigneau, S., McDonald, T.O., Igarashi, K.J., Yamamoto, K.N., Madsen, T., Fassl, A., Egri, S.B., Papanastasiou, M., et al.** s.l. : Cancer Cell 34, 939–953.e9. , (2018). .

134. *Metastatic stem cells: sources, niches, and vital pathways. .* **Oskarsson, T., Batlle, E., and Massague´ , J.** s.l. : Cell Stem Cell 14, 306–321. , (2014).

135. *Cancer stem cells: the architects of the tumor ecosystem. .* **Prager, B.C., Xie, Q., Bao, S., and Rich, J.N.** s.l. : Cell Stem Cell 24, 41–53. , (2019).

136. *Targeting hypoxic response for cancer therapy.* **Paolicchi, E., Gemignani, F., Krstic-Demonacos, M., Dedhar, S., Mutti, L., and Landi, S.** s.l. : Oncotarget 7, 13464–13478. , (2016). .

137. *Differential roles of hypoxia-inducible factor 1a (HIF-1a) and HIF-2a in hypoxic gene regulation. .* **Hu, C.-J., Wang, L.-Y., Chodosh, L.A., Keith, B., and Simon, M.C.** s.l. : Mol. Cell. Biol. 23, 9361–9374. , (2003).

138. *A distinct gene module for dysfunction uncoupled from activation in tumor-infiltrating T cells.* **Singer, M., Wang, C., Cong, L., Marjanovic, N.D., Kowalczyk, M.S., Zhang, H., Nyman, J., Sakuishi, K., Kurtulus, S., Gennert, D., et al.** s.l. : Cell 166, 1500–1511.e9. , 2016.

139. *Targeting Tim-3 and PD-1 pathways to reverse T cell exhaustion and restore anti-tumor immunity.* **Sakuishi, K., Apetoh, L., Sullivan, J.M., Blazar, B.R., Kuchroo, V.K., and Anderson, A.C.** s.l. : J. Exp. Med. 207, 2187–2194. , (2010).

140. *Deciphering the transcriptional network of the dendritic cell lineage.* **Miller, J.C., Brown, B.D., Shay, T., Gautier, E.L., Jojic, V., Cohain, A., Pandey, G., Leboeuf, M., Elpek, K.G., Helft, J., et al.** s.l. : Nat. Immunol. 13, 888–899. , (2012). .

141. *The miR-126–VEGFR2 axis controls the innate response to pathogen-associated nucleic acids.* **Agudo, J., Ruzo, A., Tung, N., Salmon, H., Leboeuf, M., Hashimoto, D., Becker, C., Garrett-Sinha, L.-A., Baccarini, A., Merad, M., et al.** s.l. : Nat. Immunol., (2013).

142. *Absence of MHC class II on cDCs results in microbial-dependent intestinal inflammation. .* **Loschko J, Schreiber HA, Rieke GJ, Esterházy D, Meredith MM, Pedicord VA, Yao KH, Caballero S, Pamer EG, Mucida D, Nussenzweig MC.** s.l. : J Exp Med. 2016 Apr 4;213(4):517-34., 2016.

143. *Role of Human Monocarboxylate Transporter 1 (hMCT1) and 4 (hMCT4) in Tumor Cells and the Tumor Microenvironment. .* **Liu T, Han S, Yao Y, Zhang G.** s.l. : Cancer Manag Res. 2023 Sep 4;15:957-975., 2023.

144. *Lactate in the Tumor Microenvironment: An Essential Molecule in Cancer Progression and Treatment. .* **Pérez-Tomás R, Pérez-Guillén I.** s.l. : Cancers (Basel). 2020 Nov 3;12(11):3244., 2020.

145. *Metastasis prevention by targeting the dormant niche. .* **Ghajar, C.M.** s.l. : Nat. Publ. Gr. 15, 238–247. , (2015).

146. *Mechanisms of disseminated cancer cell dormancy: an awakening field. .* **Sosa, M.S., Bragado, P., and Aguirre-Ghiso, J.A.** s.l. : Nat. Rev. Cancer 14, 611–622. , (2014).

147. *Cellular senescence: defining a path forward. .* **Gorgoulis V, Adams PD, Alimonti A, Bennett DC, Bischof O, Bishop C, Campisi J, Collado M, Evangelou K, Ferbeyre G, et al.** s.l. : Cell 179: 813–827. doi:10.1016/j.cell.2019.10 .005, 2019. .

148. *CDK4/6 inhibition triggers anti-tumour immunity.* **Goel S, DeCristo MJ, Watt AC, BrinJones H, Sceneay J, Li BB, Khan N, Ubellacker JM, Xie S, Metzger-Filho O, Hoog J, Ellis MJ, Ma CX, Ramm S, Krop IE, Winer EP, Roberts TM, Kim HJ, McAllister SS, Zhao JJ.** s.l. : Nature. 2017 Aug 24;548(7668):471-475., 2017.

149. *Cell cycle responses to Topoisomerase II inhibition: Molecular mechanisms and clinical implications. .* **Soliman TN, Keifenheim D, Parker PJ, Clarke DJ.** s.l. : J Cell Biol. 2023 Dec 4;222(12):e202209125., 2023.

150. *Mechanosensation of cyclical force by PIEZO1 is essential for innate immunity.* **Solis AG, Bielecki P, Steach HR, Sharma L, Harman CCD, Yun S, de Zoete MR, Warnock JN, To SDF, York AG, Mack M, Schwartz MA, Dela Cruz CS, Palm NW, Jackson R, Flavell RA.** s.l. : Nature. 2019 Sep;573(7772):69-74., 2019.

151. *Identification of essential genes for cancer immunotherapy. .* **Patel, S.J., Sanjana, N.E., Kishton, R.J., Eidizadeh, A., Vodnala, S.K., Cam, M., Gartner, J.J., Jia, L., Steinberg, S.M., Yamamoto, T.N., et al.** s.l. : Nature 548, 537–542. , (2017).

152. *Quiescent tissue stem cells evade immune surveillance. .* **Agudo, J., Park, E.S., Rose, S.A., Alibo, E., Sweeney, R., Dhainaut, M., Kobayashi, K.S., Sachidanandam, R., Baccarini, A., Merad, M., and Brown, B.D.** s.l. : Immunity 48, 271–285.e5. , (2018).

153. *Cutting-Edge Platforms for Analysis of Immune Cells in the Hepatic Microenvironment-Focus on Tumor-Associated Macrophages in Hepatocellular Carcinoma.* **Millian DE, Saldarriaga OA, Wanninger T, Burks JK, Rafati YN, Gosnell J, Stevenson HL.** s.l. : Cancers (Basel). 2022 Apr 7;14(8):1861., 2022.

154. *An HIF-1a/ VEGF-A axis in cytotoxic T cells regulates tumor progression.* **Palazon, A., Tyrakis, P.A., Macias, D., Velic¸ a, P., Rundqvist, H., Fitzpatrick, S., Vojnovic, N., Phan, A.T., Loman, N., Hedenfalk, I., et al.** s.l. : Cancer Cell 32, 669–683.e5. , 2017.

155. *Targeted hypoxia reduction restores T cell infiltration and sensitizes prostate cancer to immunotherapy.* **Jayaprakash, P., Ai, M., Liu, A., Budhani, P., Bartkowiak, T., Sheng, J., Ager, C.R., Nicholas, C., Jaiswal, A.R., Sun, Y., et al.** s.l. : J. Clin. Invest. 128, 5137–5149. , 2018.

156. *Metabolic regulation of gene expression by histone lactylation.* **Zhang D, Tang Z, Huang H, Zhou G, Cui C, Weng Y, Liu W, Kim S, Lee S, Perez-Neut M, Ding J, Czyz D, Hu R, Ye Z, He M, Zheng YG, Shuman HA, Dai L, Ren B, Roeder RG, Becker L, Zhao Y.** s.l. : Nature. 2019 Oct;574(7779):575-580., 2019.

157. *Endogenous microRNA regulation suppresses transgene expression in hematopoietic lineages and enables stable gene transfer.* **Brown, B.D., Venneri, M.A., Zingale, A., Sergi, L.S., and Naldini, L.** s.l. : Nat. Med. 12, 585–591., (2006).

158. *Best practices and tools for reporting reproducible fluorescence microscopy methods.* **Montero Llopis, P., Senft, R.A., Ross-Elliott, T.J., Stephansky, R., Keeley, D.P., Koshar, P., Marque´ s, G., Gao, Y.S., Carlson, B.R., Pengo, T., et al.** s.l. : Nat. Methods 18, 1463–1476. , 2021.

159. *Plasma and brain concentrations of doxycycline after single and repeated doses in wild-type and APP23 mice.* **Lucchetti, J., Fracasso, C., Balducci, C., Passoni, A.,**

Forloni, G., Salmona, M., and Gobbi, M. s.l. : J. Pharmacol. Exp. Ther. 368, 32–40., 2019.

160. *Comparison of distribution of doxycycline in mice after oral and intravenous application measured by a high-performance liquid chromatographic method.* **Böcker R, Estler CJ, Maywald M, Weber D.** s.l. : Arzneimittelforschung. 1981;31(12):2116-7. PMID: 7199309., 1981.

161. *Fiji: an open-source platform for biological-image analysis.* **Schindelin, J., Arganda-Carreras, I., Frise, E., Kaynig, V., Longair, M., Pietzsch, T., Preibisch, S., Rueden, C., Saalfeld, S., Schmid, B., et al.** s.l. : Nat. Methods 9, 676–682. , 2012.

162. *STAR: ultrafast universal RNA-seq aligner. .* **Dobin A, Davis CA, Schlesinger F et al.** s.l. : Bioinformatics 29 (1): 15-21., (2019).

163. *RSEM: accurate transcript quantification from RNA-Seq data with or without a reference genome. .* **Li B, Dewey CN.** s.l. : BMC Bioinformatics 12: 323., (2011). .

164. *Gene set enrichment analysis: a knowledge-based approach for interpreting genome-wide expression profiles. .* **Subramanian A, Tamayo P, Mootha VK et al.** s.l. : Proc Natl Acad Sci U S A 102 (43): 15545-15550., (2005).

165. *Integrated analysis of multimodal single-cell data.* **Hao, Y., Hao, S., Andersen-Nissen, E., Mauck, W.M., Zheng, S., Butler, A., Lee, M.J., Wilk, A.J., Darby, C., Zager, M., Hoffman, P., Stoeckius, M., Papalexi, E., Mimitou, E.P., Jain, J., Srivastava, A., Stuart, T., Fleming, L.M., Yeung, B., et al.** s.l. : Cell 184,12:3573-3587, 2021.

166. *Fast unfolding of communities in large networks. .* **Blondel, V.D., Guillaume, JL., Lambiotte, R., Lefebvre, E.** s.l. : Stat. Mech., (2008).

167. *Data exploration, quality control and testing in single-cell qPCR-based gene expression experiments. .* **McDavid A, Finak G, Chattopadyay PK, Dominguez M, Lamoreaux L, Ma SS, Roederer M, Gottardo R.** s.l. : Bioinformatics. Feb 15;29(4):461-7., (2013).

168. *The dynamics and regulators of cell fate decisions are revealed by pseudotemporal ordering of single cells.* **Trapnell, C., Cacchiarelli, D., Grimsby, J., Pokharel, P., Li, S., Morse, M., Lennon, N. J., Livak, K. J., Mikkelsen, T. S., & Rinn, J. L.** s.l. : Nature biotechnology, 32 (4), 381-386, (2014).

169. *MAST: Model-based Analysis of Single Cell Transcriptomics. R package version 1.2.1.* **McDavid, A., Finak, G., Yajima, M.** s.l. : https://github.com/RGLab/MAST/., (2017).

170. *"Moderated estimation of fold change and dispersion for RNA-seq data with DESeq2." .* **Love MI, Huber W and Anders S.** s.l. : Genome Biology., (2014).

171. *UMAP: Uniform Manifold Aproximation and Projection of Dimension Reduction. .* **McInnes, L., Healy, J., Melville, J.** s.l. : arXiv., (2020).

172. *"clusterProfiler 4.0: A universal enrichment tool for interpreting omics data.".* **Wu T, Hu E, Xu S, Chen M, Guo P, Dai Z, Feng T, Zhou L, Tang W, Zhan L, Fu x, Liu S, Bo X, Yu G.** s.l. : The Innovation, 2(3), 100141., (2021). .

173. *Single-cell transcriptomics unveils gene regulatory network plasticity. .* **Iacono, G., Massoni-Badosa, R., and Heyn, H.** s.l. : Genome Biol. 20, 1–20., (2019).

174. *Cytoscape: a software environment for integrated models of biomolecular interaction networks. .* **Shannon P, Markiel A, Ozier O, Baliga NS, Wang JT, Ramage D, Amin N, Schwikowski B, Ideker T.** s.l. : Genome Res. Nov;13(11):2498-504., (2003).

175. *PANTHER version 14: more genomes, a new PANTHER GO-slim and improvements in enrichment analysis tools.* **Mi H, Muruganujan A, Ebert D, Huang X, Thomas PD.** s.l. : Nucleic Acids Res. Jan 8;47(D1):D419-D426., 2019.

176. *Dissecting the multicellular ecosystem of metastatic melanoma by single-cell RNA-seq.* **Tirosh I, Izar B, Prakadan SM, Wadsworth MH 2nd, Treacy D, Trombetta JJ, Rotem A, Rodman C, Lian C, Murphy G, Fallahi-Sichani M, Dutton-Regester K, Lin JR, Cohen O, Shah P, Lu D, Genshaft AS, Hughes TK, Ziegler CG, Kazer SW, Gaillard A, Kolb KE, et al.** s.l. : Science. Apr 8;352(6282):189-96. , 2016.

8. ANNEXES I

8.1. Photo-conversion of Areas to dissect Micro-Environments (PADME)

Baldominos P, Barreiro O, von Andrian U, Sirera R, Montero-Llopis P, Agudo J.

STAR Protoc. 2022 Oct 28;3(4):101795. doi: 10.1016/j.xpro.2022.101795. PMID: 36325581; PMCID: PMC9619724.

My contribution was essential for the publication of this work. I designed all the experimental settings under the guidance of my thesis directors and in collaboration with Olga Barreiro. I performed all the experiments and analysis present in this work. I also contributed to a major part of the manuscript writing. The entirety of this paper is presented.

Before you begin

PADME is a versatile microscopy-based technique that enables the characterization of specific cell populations within a living tissue at the single cell level that retains information of their intra-tissue location. As an example, we developed this technique to study the transcriptional profile of cells that infiltrate specific niches within a tumor mass. This is achieved by localized photo-labelling of cells in a discrete region of interest that express a photoconvertible protein. In this specific tumor setting, the regions of interest can be defined as those enriched in a tumor sub-population with a distinctive phenotype. Visualization of such regions can be achieved, for example, by transducing tumor cells with fluorescent reporters that are uniquely expressed in the tumor sub-population of interest. Once the infiltrating cells are photolabeled by direct illumination using an optimal light source, they can be FACS-sorted and processed for scRNA-seq.

PADME can be used in a large variety of tissular contexts as long as there is a reporter or tracer to label the specific areas of interest to guide photoconversion. Furthermore, PADME *per se* can be combined with subsequent techniques such as flow cytometry,

biochemical and metabolic approaches, or other “omics” high-throughput analyses (metabolomics, epigenomics or transcriptomics to name a few).

Here we show isolation of specific intra-tumor infiltrating cells in murine primary breast cancer. Such infiltrating cells reside in micro-regions of abundant quiescent cancer cells (QCCs). In this experimental setting, tumor cells were engineered to express a reporter to visualize quiescent cells (i.e., a construct expressing tdTomato-p27K). Photo-labelled immune and stromal populations within regions enriched in QCCs could then be flow-sorted and used for scRNA-seq.

Institutional permissions

All animal procedures were approved by Dana-Farber Cancer Institute IACUC and the Harvard Medical School IACUC and performed according to DFCI protocol #17-017 and HMS protocol # IS00002540. The study is compliant with all relevant ethical regulations regarding animal research.

Note: All experiments must be compliant with the specific regulations of animal care and receive the approval from the relevant institutional review board.

Mice

PADME requires the use of transgenic animals ubiquitously expressing a photoconvertible protein such as Kaede (M. Tomura., PNAS 2008), Kikume (KikGR (Nowotschin S and Hadjantonakis AK, 2009)), Dendra2 (Miller *et al*., 2021), EosFP (Wacker *et al.,* 2007) or PS-CFP2 (Nowotschin S and Hadjantonakis AK, 2009). Alternatively, the use of photoactivatable proteins such as PA-GFP (Victora *et al.,*2010) is also feasible. However, photoconversion is advantageous since it allows for cell detection before and after photolabeling, while cells of interest are not readily visible before photoactivation. In our model, we make extensive use of Kaede (Ando *et al.,* 2002), a fluorescent protein that emits in the green spectrum but shifts its emission to red upon exposure to violet light. We used 10-week females from an F1 cross of Kaede mice

(C57BL/6 background) with Balb/c to avoid rejection of the tumor cell line models we used. Balb/c mice are commercially available and we obtained them from Jackson laboratories. Kaede mice were obtained from Dr. Michio Tomura upon MTA approval.

Cell lines

4T07 cells were a gift from Dr. Robert Weinberg and were cultured in Iscove's Modified Dulbecco's Medium (IMDM), 10% heat inactivated FBS (Gibco), 1% Penicillin-Streptomycin (Gibco) and 1% Glutamax (Gibco). Protocol was optimized to work with cellular reporters to label regions of interest inside the tumor but it can be easily modified to use antibody staining among other experimental designs.

CRITICAL: Take into account excitation, emission, and photoconversion wavelengths needed in your specific mouse model when adapting the experimental design.

Cells were engineered to express a modified quiescent reporter from Dr. Kitamura (Oki et al., 2014), tdTomato-p27k using lentiviral system. Although tdTomato and photoconverted Kaede fluorescent emissions overlap, they are expressed in different cell types. Kaede-expressing cells are either green (non photoconverted) or double-positive (green, red - photoconverted), thus cannot be confused with tdTomato-p27k single positive tumor cells.

CRITICAL: Transduced cells were selected by FACS sorting at confluency to maximize expression of the quiescent reporter.

Tumor injection

Timing: 2 weeks

Tumors were induced by intra-mammary fat pad injection.

1. Prepare cell suspension for injection.
    a. Obtain a single-cell suspension of the cells in culture following standard cell culture passaging technique.

   b. Wash cells 2x in sterile PBS.
   c. Count cells and prepare 250,000 cells in 50µL sterile PBS per mouse.
2. Prepare mice for surgery.
   a. Anesthetize mice with 4% isoflurane in an induction chamber.
   b. Shave hair around the 4th nipple.
   c. Apply eye ointment to prevent corneal drying.
   d. Place the mouse in the nose cone to maintain the delivery of 2% isofluorane. Assess the depth of anesthesia by pinching the mouse hind paw with tweezers to check for absence of pedal reflex.
   e. Clean the area with 70% ethanol wipes and iodine to keep aseptic the area.
3. Mammary fat pad injection
   a. Make a 2mm incision next to the nipple area.
   b. Localize mammary gland.
   c. Inject 50µL of the cell suspension into the mammary fat pad.
      CRITICAL: Keep needle parallel to the skin to avoid injecting in the intraperitoneal cavity.
   d. Drop a couple of drops of lidocaine for topical analgesia in the incision.
   e. Close the incision using tissue glue (VetBond®).

Place the chilling block on the freezer

Timing: 1h

During the embedding process of the tumor, we will use a chilling block (provided with the compresstome) to cool and solidify agarose faster, minimizing the waiting time and reducing heat damage to the tissue. Place the chilling block at -20 for at least 1h before use to let it cool down.

Prepare 12 well plate

Timing: 10 min

Fill all wells from a 12 well plate with 1ml of non-supplemented IMDM medium to store the tumor and the slices obtained during the process.

Materials and equipment

Compresstome

The VF-310-0Z compresstome from Precisionary Instruments LLC was used to obtained live tissue sections.

Point scanner confocal microscope

A Zeiss LSM710 single photon point-scanning confocal unit with galvanometer mirrors attached to a fully motorized Axio-Observer Z1 inverted microscope equipped with a Zeiss motorized stage and a Zeiss Plan Apochromat 20x/0.8 NA DIC air objective was used. A 405nm 30mW diode AOTF modulated line was used for photoconversion. An argon multi-line 488 nm 25 mW Argon AOTF modulated line and a 561 nm 20mW DPSS AOTF modulated line were used for image acquisition. The emission wavelength range for the green and red fluorescence signals was set to 499-560 nm and 571-735, respectively, and collected by multi-alkali PMTs.

CRITICAL: Imaging and photoconversion require the use of laser lines that are hazardous for eyes and skin irradiation. Avoid exposure to laser beams and use eye protection when required.

Alternatives: Any single point-scanning confocal microscope or spinning disk confocal microscope equipped with a DMD (Digital Mirror Device) endowed with the capability of drawing irregular polygonal regions of interest (ROI) can be used for this photoconversion-based method. If the microscope software only allows the use of standard ROIs (squared, rectangular, circular or ellipsoid regions), the user will not be able to accurately photoconvert individual cell clusters (“niches”) with irregular shapes.

This point might be critical or not depending on the scientific question to be addressed. If “irregular” illumination is not required, alternative equipments such as a widefield microscope can be used to image and photoconvert areas of interest.

Step-by-step method details

Tumor sectioning

Timing: 1-2 h

After tumor growth and harvest, tumors were processed with a compresstome in order to obtain live tumor slices whose infiltrates can be photoconverted using a point scanner confocal microscope. The use of slices directly exposes deep tumoral areas, avoiding the need of a multiphoton microscope for photoconversion across the whole tumor. Besides, the use of slices also allows for the enrichment of the population/s of interest, increasing recovery yield in the subsequent flow-sorting step.

1. Collect tumor. Harvest the tumor with the help of scissors and a blade to maintain tissue integrity. Trim the surrounding fat tissue. Place the tumor in one well of the 12-well cell culture plate with medium prepared before starting.

   Note: When possible protect tumor from light to avoid photobleaching or undesired photoconversion.

2. Embed tissue in low melting agarose.

   a. Mounting tumor into the specimen tube.

      i. Cut with a blade the edge of the tumor to generate a flat surface.

      ii. Place one drop of Gorilla Glue® into the tissue holder of the specimen tube.

      iii. Glue the flat surface of the tumor to the tissue holder (Figure S1A).

Critical: Make sure the tissue is located in the center to obtain a block with homogenous agarose thickness around the tissue when embedding.

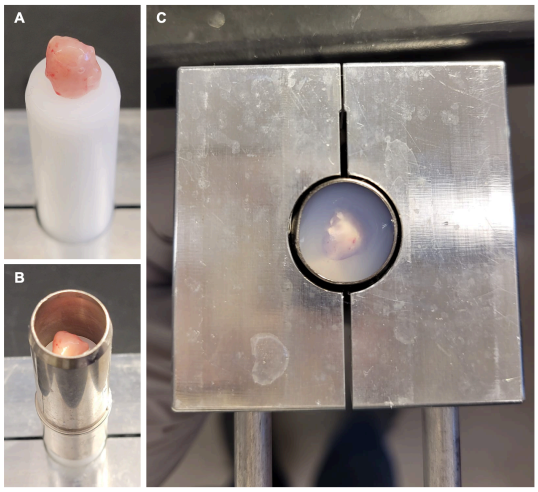

Figure S1. Mounting tumor into specimen tube. A) Glue tissue to tissue holder (white plunger). B) Assemble tissue holder with the metallic tube to create embedding cavity. C) Place sample holder into the chilling block to solidify the agarose faster.

b. Prepare the agarose solution.

i. Dissolve 0.5g of agarose in 25ml of PBS to get a 2% agarose solution.

Critical: Agarose concentration in this protocol is optimized for our model of mammary tumors. It is crucial that the agarose density is similar to that of your tissue to obtain clean slices.

ii. Heat the solution in a microwave until the solution gets clear (20-30'' aprox).

iii. Cool down the solution by washing the flask under cold running water to reach 37C.

iv. Use right away to prevent undesired polymerization prior to tissue embedding.

Note: The flask can be kept in a water bath at 37C to avoid solidification.

c. Embed tissue with agarose.

i. Assemble the specimen tube by introducing the sample holder (white plunger) into the metal tube (Figure S1B).

ii. Cut the tip of a 1000µl pipette tip to facilitate the pipetting of a dense substance such as agarose and pour it around the tissue into the sample holder.

Critical: Avoid bubble formation during this process. Additionally, when embedding the tissue in agarose, be sure to leave approximately 0.2-0.5cm between the sample and the edge of the tube to set up compresstome settings with the free agarose before reaching the sample.

iii. Introduce the specimen tube into the chilling block until agarose solidifies (Figure S1C).

3. Slice samples with the compresstome.

a. Assemble the sample holder into the compresstome following manufacturer instructions (compresstome VF-310-0Z user manual). Make sure the blade is placed in the correct position and the buffer tray is secured in place with the screw tightly attached. (Figure S2A,B)

b. Fill buffer tray with PBS until it covers half of the sample (specimen tube).

c. Sectioning of the tissue.

i. Push the tissue advancement plunger until the agarose is seen out of the tube.

ii. Set machine in single cutting mode, speed 1-3 and oscillation 5-6. Set slice thickness to 300µm.

Note: Settings are optimized for the breast tumors we normally process, but they need to be adjusted for each specific tissue and also throughout the slicing process, as the tumor surface increases and becomes less cohesive. See **Problem 1** in **Troubleshooting** section for more details.

iii. Slice through the agarose using the manual fast forward to trim the tissue-free agarose gel using thicker slicing until the tissue appears. The speed of cutting can also be increased during the trimming. Do not cut slices thicker than ~2mm to obtain slices with even surfaces. **Note**: During trimming, you can set continuous mode and a higher slice thickness. However, make sure you start reducing the slice thickness gradually before reaching the tissue, since the equipment does not readjust the thickness immediately (it might take a couple of slices to get the desired slice thickness).

iv. Once the tissue is visible, change to single mode and keep adjusting the settings to the tissue needs. Generally a speed 1-3 and oscillation 5-6 is suitable for most tissues. Place sequential slices in pairs in one well of the 12-well plate with medium to store them until image acquisition. (Figure S2C,D).

Note: Keep the 12-well plate on ice and covered from light. Slices should be protected from light to avoid photobleaching or undesired photoconversion.

v. After finished slicing the tumor, make sure to clean the buffer tray, the blade and the sample holder. Remove the gorilla glue with acetone if needed.

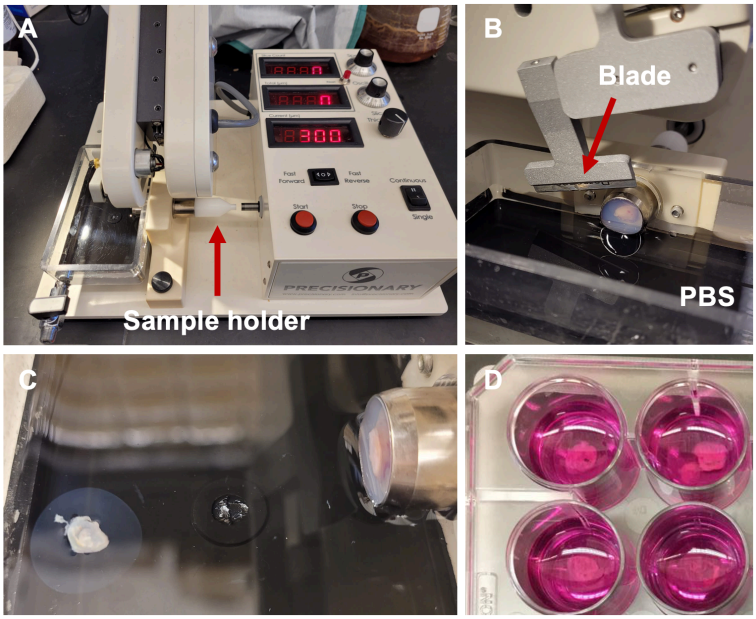

Figure S2. Tissue sectioning with compresstome. A,B) Compresstome assembly. C) Successful floating tissue section. C) Sections stored in non-supplemented medium to keep track of sequential slices after sectioning until microscope processing.

Photoconversion in the microscope

Timing: 1-1.5h/slice

Live tissue slices are mounted on a slide and photoconverted using a point-scanning confocal microscope that can perform selective illumination of irregular polygonal ROIs to maximize the spatial resolution of the areas of interest.

4. Mount tumor slice on a microscope slide:
    a. Place a few drops of medium on the slide before mounting the slice to facilitate straightening the tissue.
    b. Set the slice on the slide and carefully extend it using tweezers, without inflicting damage to the tissue.
    c. Add a moisturizing agent such as lubricant eye gel to decrease evaporation and maintain/keep slices hydrated during the whole imaging process.

Note: The use of lubricant instead of alternative physiological aqueous buffers helps avoiding desiccation. Lubricant eye gel might possess slightly different refractive index as compared to water-based buffers impacting in the quality of imaging. However, the aim of this imaging step is the specific photoconversion of cellular niches and not the generation of high-resolution images. As the tissue needs further processing to obtain a viable single-cell suspension, we prioritize the wellbeing of the tissue over the quality of imaging at this step.

d. Place a coverslip and seal the edges using paraffin or nail polish to fix the sample.

Note: Use nail polish with caution since it could be toxic for the sample in case of undesired contact.

5. Scan the whole slice by tiling fields of view (FOV) to generate a full-size image of the tissue that helps to identify regions of interest:

a. Acquire a tile scan using fast scan rate (short pixel dwell time) and low resolution to generate a full-size image of the whole slice:

i. Collect green (non-photoconverted Kaede) and red (from tdTomato-p27k reporter in quiescent cancer cells in our experimental model) fluorescence by using a Zeiss Plan Apochromat 20x/0.8 NA DIC air objective. The acquisition settings are as follows: the sample was illuminated with an argon multi-line 488 nm 25 mW Argon AOTF modulated line set to 0.2 % transmittance and a 561 nm 20mW DPSS AOTF modulated line set to 0.2 % transmittance, using a multi-bandpass dichroic mirror with 488/561cut off wavelengths (MBS 488/561). The emission wavelength ranges for the green and red fluorescence signals were set to 499-560 nm and 571-735, respectively, and collected using multi-alkali PMTs. No offset was applied. The microscope was controlled by ZEN Black SP2

acquisition software, scanned unidirectionally with a pixel dwell time of 1.58µsec/pixel, no averaging, a 12-bit digitizer, zoom 1.0x, a pixel size of 0.83µm and pinhole set to 1 A.U. for 488 nm wavelength. Images were saved with the .czi file format.

b. Once a mesoscopic image of the tissue is obtained, positions of interest can be marked per slice. In our experimental model, positions were placed in tdTomato-p27k^{High} areas in the first slice and in tdTomato-p27k^{Negative} areas in the consecutive paired slice (Figure S3A).

6. Photoconversion of the identified regions of interest:

a. A single confocal image (snapshot) was generated for each position marked in the slice using same microscope settings as in 5.a.i., except for the pinhole aperture that was set to max.

Note: In confocal microscopy, fluorophore excitation is not restricted to the focal plane.

Critical: Opening the pinhole allows to recover also the out of focus signal above and below the focal plane. This is critical to assess that the volume to be photoconverted only contains cells of interest (either tdTomato-p27k^{High} or tdTomato-p27k^{Negative} clusters).

b. A defined region of interest (ROI) was drawn in the snapshot using the freehand shape tool of the microscope (Figure S3B).

Note: If the aim is to compare the approximate number of infiltrating cells or the relative abundance of a cell type among different conditions, equivalent areas should be photoconverted. For this purpose, a ROI can be initially defined and saved, then applied to every position of interest throughout the set of slices from the same experiment.

c. Photoconversion of Kaede protein was performed specifically within the ROI using a Zeiss Plan Apochromat 20x/0.8 NA DIC air objective, a 405nm 30mW diode AOTF modulated line set to 0.2 % transmittance laser, and a

405 long-pass dichroic mirror. A time series of 325 cycles at a 1.58µsec/pixel (pixel dwell time) was used during photoconversion.

d. A single confocal micrograph with dual green-red fluorescence was acquired after photoconversion using the settings from 5.a.i. (Figure S3C) to ascertain that the process was successful. If not, check **problem 2** in **Troubleshooting** section.

7. Scan the whole slice to check the overall photoconversion using same setting as 5.a.i. (Figure 3C).

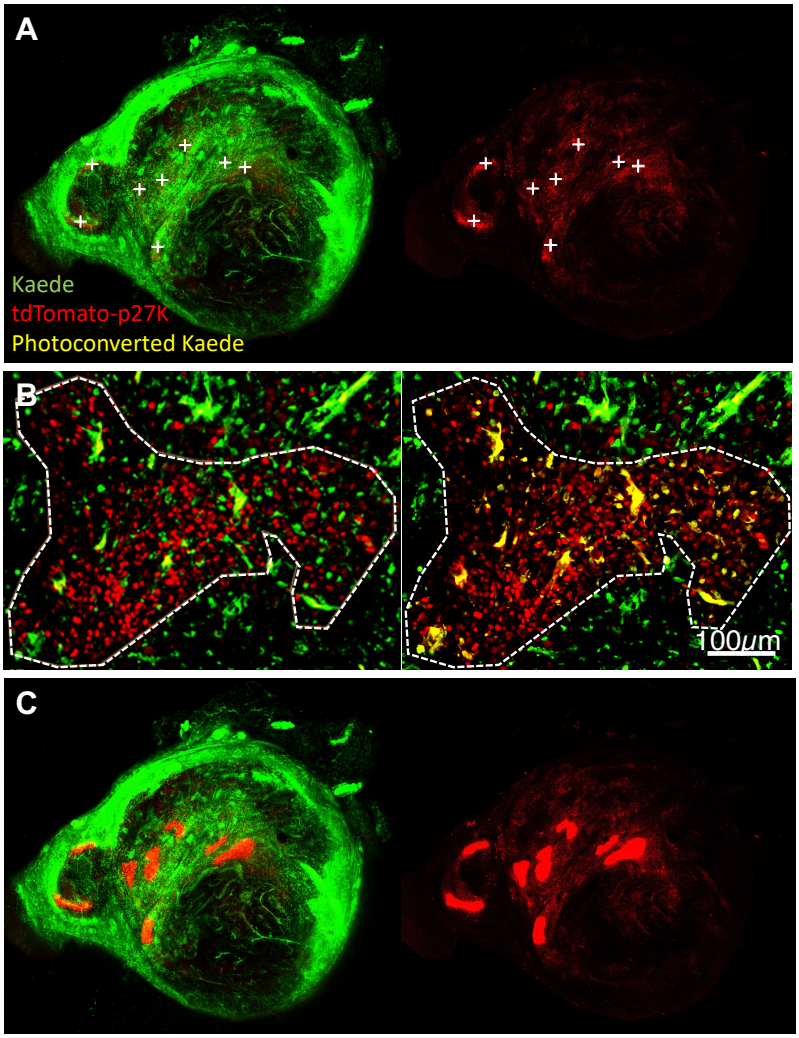

Figure S3. Photoconversion of Kaede protein in tumor slices. A) Full-size image of the tumor slice showing the distribution of the expression of the non-photoconverted Kaede protein in host cells (green channel) and the expression of the quiescence reporter in specific tumor cells (red channel). The data from the red channel was used to select positions of interest (white crosses) based on the tdTomato-p27k reporter (red). B) Region of interest drawn based on tdTomato-p27k reporter expression (white dash-dotted line) before and after photoconversion (left and right, respectively). Overlay of green and red channels is shown. C) Full-size image of the tumor slice acquired after photoconversion to corroborate successful photoconversion in all selected positions.

Slice processing and flow sorting populations

Timing: 30-45min processing + 1h sorting per slice

Photoconverted slices are digested to obtain single-cell suspensions that are flow-sorted to isolate individual photoconverted cells from the specific tumor region of interest.

8. Tissue digestion to obtain a single-cell suspension:

    a. Prepare digestion buffer as follows:

    Table S1. Digestion buffer

Reagent	Amount
Hyaluronidase	6.8U/mL
Collagenase IV	400U/mL
DNaseI	20µg/mL
FBS	10%
HBSS	Up to 500 µL/slice

    b. Digest slices:

        i. Place 500µL of the digestion buffer in a 12-well cell culture plate to digest each slice separately.

ii. Put tissue slice in the solution and disrupt tissue with two needles.

iii. Incubate for 15-20min at 37C.

iv. Pipette up and down with a 1000µL pipette to further disrupt tissue.

v. Filter digestion with a 100µm (pore size) filter, washing the well and the filter with flow buffer (2mM EDTA, 0.1% BSA in PBS).

vi. Spin down at 800g for 5min.

c. Prepare a single-cell suspension for sorting:

i. Resuspend in 500µL of red blood cell lysis buffer (Biolegend) and incubate for 5min at RT.

ii. Wash with flow buffer.

iii. Spin down at 800g for 5min.

Optional: Stain with antibodies to analyze specific cell populations, such as exhaustion markers in our particular case (Baldominos P. et al, Cell 2022).

Critical: As quality control, it is recommended to stain a single-cell suspension from one slice that has gone through the whole procedure, combining an apoptosis marker such as AnnexinV and a viability dye (DAPI, Biolegend). Viable cells will be negative for both markers. The percentage of cell viability in photoconverted samples should be comparable to non-photoconverted ones.

Note: We did not experience major phototoxicity issues with the conditions used for photoconversion.

iv. Resuspend in flow buffer + DAPI (dilution 1:10000 from stock, Biolegend).

9. Sort photoconverted population:

a. Set gates using a single-cell suspension from a non-photoconverted slice (negative control) and another from a photoconverted slice with a big photoconverted area as a positive control (Figure S4A).

b. Check cell viability using the single-cell suspension stained with AnnexinV and DAPI, as a quality control before proceeding further with the protocol (Figure S4B).

   Note: If cell viability is low, check **problem 3** in **Troubleshooting** section.

c. Sort enough cells to comply with the requirements for sequencing. In our experimental model, the target amount for scRNA-sequencing using 10x genomics platform was 10000 cells per condition (See **problem 4** in **Troubleshooting** section).

   Note: Sorting in serum-supplemented cell culture medium increases cell viability but requires extra washing steps that might reduce the cell recovery yield.

   Critical: If sorting in serum-supplemented culture medium, use 1.5ml Eppendorf tubes and a swing centrifuge to minimize cell loss during repeated washes.

d. Samples are ready for standard single-cell RNA-sequencing (such as 10x genomics, the procedure used for our experimental model) or any other analysis dependent on the scientific question to be addressed.

   Note: If comparing two different regions inside of a tumor, it is recommended to use hashtags to eliminate technical variability when sequencing paired samples.

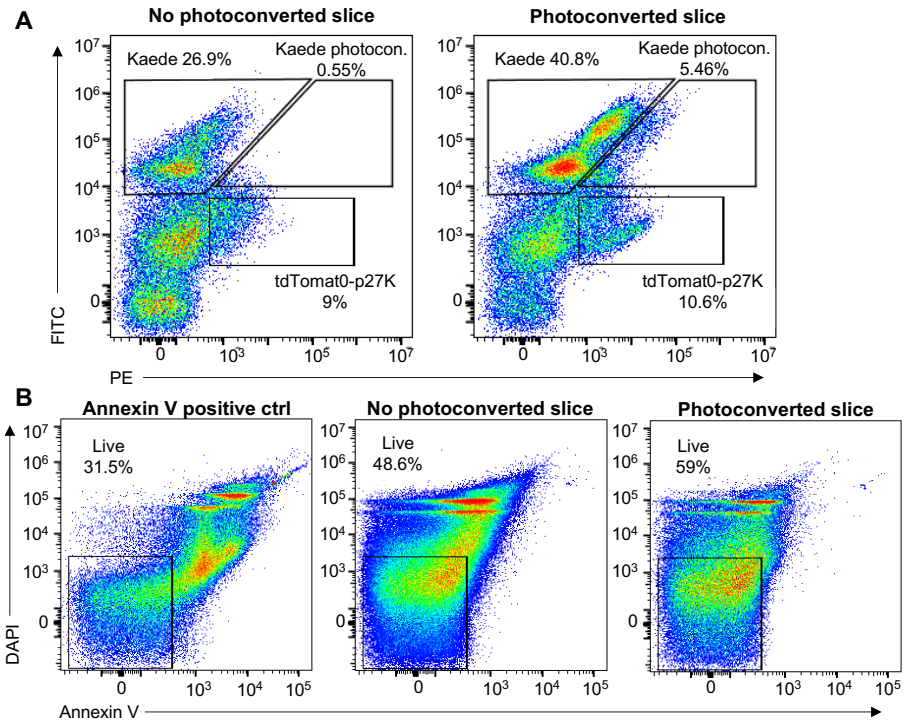

Figure S4. Representative FACS plots of photoconverted infiltrates. A) Set up gate strategy using the DAPI negative cell population gated from a non-photoconverted sample (left) and from a photoconverted one (right). B) Assessment of sample viability after photoconversion using viability dye (DAPI) and annexinV staining (to control for apoptosis).

Expected outcomes

After performing this protocol, infiltrates in the areas of interest inside of a tumor will be labeled by photoconversion. This protocol will allow to flow-sort single-cell populations from a known spatial location, enabling scRNA-Seq with detailed spatial resolution (Figure 4).

Quantification and statistical analysis

Photoconverted infiltrates from different areas were submitted to the Brigham and Women's Hospital Single-Cell Genomics Core for 10x genomics sequencing and analyzed following well-stablished pipelines in Seurat package (Hao et al., 2021; Stuart

et al., 2019; Butler et al., 2018; Satija el at., 2015), as explained in Baldominos et al. (2022).

Limitations

* Overall time from photoconversion to cell recovery is critical for cell viability. For that reason, we limit photoconversion to a maximum of 10 different regions per tissue section, with an area < 50% of the FOV/region. All the microclusters in the tissue section are not photoconverted, but this is not a problem, since we only analyzed photoconverted cells (being 10 regions/slice optimal to obtain enough cell recovery yield with acceptable viability).

* PADME might not be the most accurate or quantitative technique to fairly compare, e.g., number of infiltrating cells or the relative abundance of a cell type among different conditions, since photodamage and tissue processing might affect differently specific cell populations.

* The consistency of the tissue to be analyzed might not allow the use of tissue sections. This scenario might be overcome by using fresh tissue (such as a whole tumor) and a multiphoton microscope for the photoconversion step. Take into account that light penetrance will continue to be a limiting factor, even using this equipment that allows for deep tissue imaging.

* Processing of the tissue (e.g. agarose embedding, sectioning) might partially affect the metabolic or activation status of the cells of interest, inducing subtle changes in their transcriptional profiles, as compared to fresh tissue.

Troubleshooting

Problem 1: Slices are not cut evenly in thickness or tissue gets disrupted during the cutting process.

During tissue slicing, it is necessary to have the same density across the tissue surface to maintain fix settings. However, tumors are not homogeneous, and the core has usually necrotic areas, that dramatically change the tissue consistency affecting the integrity of the slices.

Potential solution: Adjust speed and oscillation as you cut through the tissue.

The speed of the blade can be adjusted during the cutting process. You can lower the speed when the blade is approaching difficult areas (usually the center of the tumor) to improve cutting. You can also increase or decrease the oscillation to help with tissue integrity. Higher oscillation will improve the cutting, but if the tissue consistency is very soft tissue integrity can be compromised. It is necessary to balance both settings to get an even and consistent tissue slice.

If problems persist, multiphoton microscopy could be used to penetrate deeper in the tissue and allow for accurate photoconversion of thicker slices (easier to generate) or even of a whole-mount tissue preparation. However, fluorophore excitation in a multiphoton microscope is restricted to the focal plane, as opposed to confocal microscopy. This dramatically reduces the amount of photoconverted cells obtained per cycle. Therefore, using this type of equipment increases the overall microscopy time due to the need of photoconversion in several focal planes across the sample, which can be a limiting factor depending on the downstream application.

Problem 2: Suboptimal photoconversion.

Potential solution: If photoconversion is not optimal, you will need to change your microscopy settings by increasing time of fluorescence excitation or laser power, but always being aware of the concomitant increase in phototoxicity. We recommend increasing the number of cycles of fluorescence excitation, instead of the continuous illumination of the sample.

Problem 3: High phototoxicity and low viability observed in the combined annexin V and viability staining.

The photoconversion process requires violet light exposure of live tissues that can be cytotoxic and induce cell death. Using Annexin V combined with a viability dye as quality control helps to define the microscope settings that are optimal to minimize cell damage.

Potential solution: Adjust microscope settings for photoconversion to reduce photodamage.

Kaede protein is photoconverted from green to red with ultraviolet light. However, increasing the wavelength to the violet spectrum reduces phototoxicity, since a higher lambda radiation carries less energy and will improve the overall quality of the sample. Prolonged exposure also increases the temperature of the sample, contributing to tissue damage. In order to minimize these issues, the laser scanning dwelling time can be reduced. Hence, scanning faster but performing several cycles of laser exposure using the time series setting allows to achieve an optimal photoconversion with less harmful conditions. Another plausible solution to overcome phototoxicity is the use of multiphoton microscopy that relies on infrared wavelengths with lower frequency, lower energy level and higher tissue penetrance than those in the violet spectrum. However, multiphoton technology might not be broadly available as compared to the widespread use of conventional single-photon excitation confocal laser scanning microscopes. Alternatively, the use of a DMD (Digital Mirror Device) or similar spatial light modulators that use LED-based illumination, therefore producing lower irradiation than a point scanning confocal microscope, may be used to reduce phototoxicity.

Problem 4: Poor recovery yield after cell sorting.

If the viability of the samples is acceptable but the cell recovery yield after cell sorting is insufficient to run a scRNA-Seq experiment or another alternative downstream analysis, the number of photoconverted areas should be increased.

Potential solution:

Increase the number of slices to be pooled in a single-cell sequencing experiment instead of increasing the amount of photoconverted ROIs/sample will better preserve the cell viability, while increasing the cell recovery yield.

9. ANNEXES II

9.1. Scientific contribution

9.1.1. Articles

1. **Baldominos P,** Barbera-Mourelle A, Barreiro O, Huang Y, Wight A, Cho JW, Zhao X, Estivill G, Adam I, Sanchez X, McCarthy S, Schaller J, Khan Z, Ruzo A, Pastorello R, Richardson ET, Dillon D, Montero-Llopis P, Barroso-Sousa R, Forman J, Shukla SA, Tolaney SM, Mittendorf EA, von Andrian UH, Wucherpfennig KW, Hemberg M, Agudo J. Quiescent cancer cells resist T cell attack by forming an immunosuppressive niche**. Cell. 2022** May 12;185(10):1694-1708.e19. doi: 10.1016/j.cell.2022.03.033. Epub 2022 Apr 20. PMID: 35447074.

2. **Baldominos P**, Barreiro O, von Andrian U, Sirera R, Montero-Llopis P, Agudo J. Protocol to isolate live single cells while retaining spatial information by combining cell photolabeling and FACS. **STAR Protoc. 2022** Oct 28;3(4):101795. doi: 10.1016/j.xpro.2022.101795. PMID: 36325581; PMCID: PMC9619724.

9.1.2. Congress communications as poster

1. **2023 Mammary Gland Biology Gordon Research Seminar and Conference**: Baldominos P, Barbera-Mourelle A, Barreiro O, Huang Y, Wight A, Agudo J. Quiescent cancer cells resist T cell attack by forming an immunosuppressive niche.

   Best poster award.

2. **37th Annual meeting of the Society for Immunotherapy in cancer (SITC)**: Baldominos P, Barbera-Mourelle A, Barreiro O, Huang Y, Wight A, Agudo J. Quiescent cancer cells resist T cell attack by forming an immunosuppressive niche.

3. **2022 American Association fo Cancer Research (AACR) Special Conference on Tumor Immunology and Immunotherapy**: Baldominos P, Barbera-Mourelle A, Barreiro O, Huang Y, Wight A, Agudo J. Quiescent cancer cells resist T cell attack by forming an immunosuppressive niche.

4. **2021 American Association fo Cancer Research (AACR) Virtual Special Conference on Tumor Immunology and Immunotherapy**: Baldominos P, Barbera-Mourelle A, Barreiro O, Huang Y, Estivill G, …, Agudo J. Quiescent cancer cells form immunotherapy resistant reservoirs by forming an immune suppressive niche.

9.2. Scientific mentoring

1. Synthetic biology approaches to study tumor cell dissemination and the metastatic niche in breast cancer. 2023. **Ia Codinachs Bosch**. International University of Catalonia.

9.3. Fellowships and awards

1. La Caixa pre-doctoral fellowship for postgraduate studies in North America, Asia and Pacific Ocean 2018 (LCF/BQ/AA18/11680040) funded by ‘‘La Caixa’’ Foundation (ID 100010434).
2. Premio Joven Talento 2022 (Young Scientist Award) Fundación EVAP (Entrepreneur Women Fundation), (Spain).

9.4. International internships

1. Harvard Research fellow program at Harvard Medical School 2023-2024.